The Pennsylvania State University

The Graduate School

College of Earth and Mineral Sciences

DYNAMICS OF SHALLOW MARINE GAS HYDRATE AND FREE GAS SYSTEMS

A Thesis in

Geosciences

by

Xiaoli Liu

Submitted in Partial Fulfillment
of the Requirements
for the Degree of

Doctor of Philosophy

May 2006

The thesis of Xiaoli Liu was reviewed and approved* by the following:

Peter B. Flemings
Professor of Geosciences
Thesis Adviser
Chair of Committee

Richard B. Alley
Evan Pugh Professor of Geosciences

Michael A. Arthur
Professor of Geosciences

Turgay Ertekin
Professor of Petroleum and Natural Gas Engineering

Katherine H. Freeman
Professor of Geosciences
Associate Head for Graduate Programs and Research

*Signatures are on file in the Graduate School.

ABSTRACT

Multi-phase fluid flow is critical to the formation and concentration of gas hydrate in marine sediments. A transient, multi-phase (hydrate, gas and liquid) fluid and heat flow model is presented to describe hydrate formation in porous media. Fluid flux and physical properties of sediment largely control the dynamics of gas hydrate formation and free gas migration. In fine-grained sediments, hydrate formation leads to rapid permeability reduction and capillary sealing. Free gas accumulates below the hydrate layer until a critical gas column builds up, thereby forcing gas upward to the seafloor. In coarse-grained sediments, large volumes of gas are transported into the hydrate region to produce a significant change in salinity. An interconnected three-phase zone with high hydrate concentration and elevated salinity develops from the base of hydrate stability to the seafloor. Both processes may drive gas venting through the hydrate stability zone.

We also extend these models to demonstrate that the likely impact of climatic warming events on marine hydrate reservoirs. If hydrates are originally formed in the two-phase region, dissociated methane cannot be released to the ocean until the warming at the seafloor exceeds a critical value. However, all of hydrates formed within the three-phase zone are already at the dissociation boundary. Thus they can be affected by small warming events and are most susceptible to environmental changes.

TABLE OF CONTENTS

List of Tables

List of Figures

Acknowledgements

I would like to express my sincere appreciation to my thesis advisor Dr. Peter Flemings, who provided guidance and support in all aspects of this research. I also thank Dr. Turgay Ertekin, Dr. Richard Alley, and Dr. Michael Arthur for their participation in my thesis committee and for their comments and suggestions. Appreciation is extended to all my friends and colleagues in Basin Research Group for their useful discussion and encouragement.

I would like to thank my wife for all of her support and encouragement.

I acknowledge from the financial support from the Penn State GeoFluids Consortium, the ExxonMobil Quantitative Geosciences Fellowship and the JOI/USSAC Fellowship.

Chapter 1

INTRODUCTION

Gas hydrate is an ice-like mineral that contains methane or other low molecular weight gases (e.g., ethane, CO_2, H_2S) in a lattice of water molecules [*Sloan*, 1998]. Most of the naturally occurring hydrates are methane hydrate. Methane hydrates are stable under the low-temperature and high-pressure conditions commonly found in the Arctic and near the seafloor at water depths >300 m [*Kvenvolden*, 1993]. Hydrates are common beneath the slope of both active (e.g., Hydrate Ridge, offshore Oregon) and passive (e.g., Blake Ridge, offshore Carolinas) continental margins, where adequate supplies of gas are available [*Hyndman and Davis*, 1992]. The large volume of gas stored in hydrate structures represents a significant fraction of the global methane budget [*Kvenvolden*, 1993] and may be a potential energy resource for the future [*Milkov and Sassen*, 2002]. Pressure increase due to rapid hydrate decomposition may contribute to failure along continental margins where gas hydrate is found [*Kayen and Lee*, 1991; *Paull et al.*, 1996]. Several authors [*Nisbet*, 1990; *Dickens et al.*, 1995; *Kennett et al.*, 2000; *Dickens*, 2003] have suggested that dissociation of subsurface gas hydrates in response to changes in ambient conditions may play an important role in the past and present climates.

The previous studies have underestimated the fundamental link between the gas transport mechanism and the formation and concentration of gas hydrate. We analyze gas hydrate provinces as hydrologic systems. In this study, through integrated field, modeling

and experimental analysis, we quantitatively address (1) the hydrologic factors that control hydrate formation and distribution, (2) the critical role of free gas migration in hydrate formation, (3) the amounts of methane in gas hydrate and underlying free gas, (4) the response of hydrate system to seafloor changes in temperature and pressure.

There is emerging evidence for free gas migration within gas hydrate provinces. In Chapter 2, we present a conceptual model for free gas migration through the hydrate stability zone without being converted into gas hydrate. This conceptual model nicely ties together several lines of observations from southern Hydrate Ridge, offshore Oregon. Core and log data show that three-phase equilibrium may exist in the uppermost 50 m sediments below seafloor at the ridge crest.

In Chapter 3, we develop a numerical, multiphase fluid and heat flow model to better understand the processes that determine the distribution, nature and concentration of gas hydrates in marine environments. We show that sediment lithology and fluid flux are the critical parameters controlling the dynamics of gas hydrate deposits and free gas migration. Recent seismic evidences suggest that the base of the hydrate stability zone commonly shows topography. The model described above is extended to two dimensions to study the relative importance of several mass transport processes in the formation of hydrate-driven fluid features (e.g., gas chimney).

The process of methane release to the ocean is also a multiphase fluid flow problem within a sediment-gas-water system. In Chapter 4, we explore how hydrate reservoirs respond to environmental changes, including exactly how dissociated methane escapes to the ocean. We show that the hydrate system at South Hydrate Ridge is already everywhere at the three-phase boundary, and therefore it is highly sensitive to changes in

ambient conditions, offering a mechanism for rapid release of methane from gas hydrate deposits.

Chapter 2

PASSING GAS THROUGH THE HYDRATE STABILITY ZONE AT SOUTHERN HYDRATE RIDGE, OFFSHORE OREGON

Abstract

We present an equilibrium model of methane venting through the hydrate stability zone at southern Hydrate Ridge, offshore Oregon. Free gas supplied from below forms hydrate, depletes water, and elevates salinity until pore water is too saline for further hydrate formation. This system self-generates local three-phase equilibrium and allows free gas migration to the seafloor. Log and core data from Ocean Drilling Program (ODP) Site 1249 show that from the seafloor to 50 meters below seafloor (mbsf), pore water salinity is elevated to the point where liquid water, hydrate and free gas coexist. The elevated pore water salinity provides a mechanism for vertical migration of free gas through the regional hydrate stability zone (RHSZ). This process may drive gas venting through hydrate stability zones around the world. Significant amount of gaseous methane can bypass the RHSZ by shifting local thermodynamic conditions.

1. Introduction

Gas hydrate is an ice-like compound that contains methane and/or other low molecular weight gas in the lattice of water molecules [*Sloan*, 1998]. Although most of the seafloor lies within the low-temperature and high-pressure conditions necessary for hydrate formation, hydrate is generally found in sediments along continental margins [*Kvenvolden*, 1993], where adequate supplies of gas are available [*Hyndman and Davis*, 1991]. The large volumes of gas stored in hydrate are a potential energy resource [*Milkov and Sassen*, 2002]. Release of large volumes of methane from hydrate into the ocean and atmosphere may play a role in the past climate change [*Dickens et al.*, 1995; *Kennett et al.*, 2000; *Dickens*, 2003]. Pressure increase due to rapid hydrate decomposition may contribute to failure along continental margins where gas hydrate is found [*Kayen and Lee*, 1991; *Paull et al.*, 1996].

Southern Hydrate Ridge lies at ~800 m water depth in the Cascadia accretionary complex (Fig. 2-1). A bottom-simulating reflector (BSR) is imaged pervasively beneath it [*Trehu et al.*, 1999]. The BSR is a strong, negative-polarity, strata-crossing, seismic reflector that mimics the seabed and records the phase boundary between gas hydrate above and free gas below [*Bangs et al.*, 1993; *Holbrook et al.*, 1996]. Gas vents, hydrate outcrops, authigenic carbonate deposits, and chemosynthetic organisms are present on the seafloor [*Suess et al.*, 1996; *Heeschen et al.*, 2002]. A 50-m-high pinnacle of authigenic carbonate is located ~350 m southwest of the summit [*Trehu et al.*, 2003]. Beneath the Pinnacle, there is a zone of low reflectivity (wipeout) overlying a weak and disrupted BSR (Fig. 2-2).

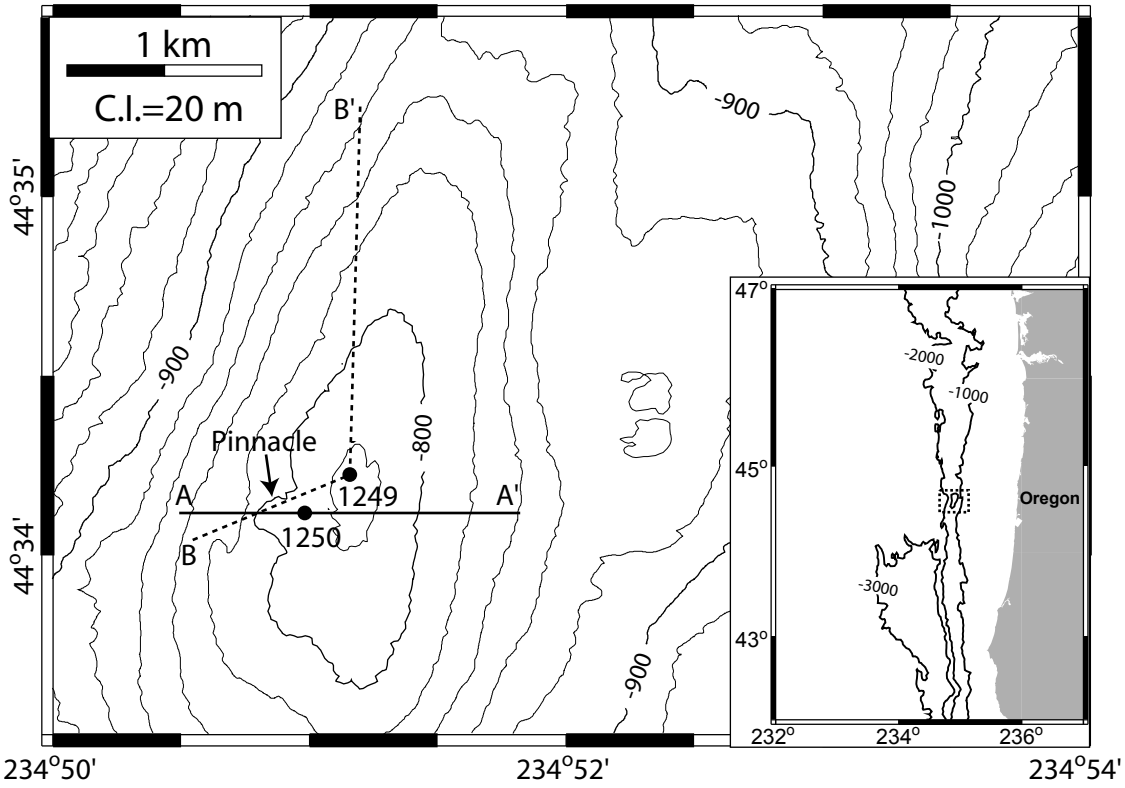

Fig. 2-1: Topography of southern Hydrate Ridge (in meters below sea level). Contour interval is 20 m. Inset map shows location of Hydrate Ridge. Bathymetric contour interval is 1000 m.

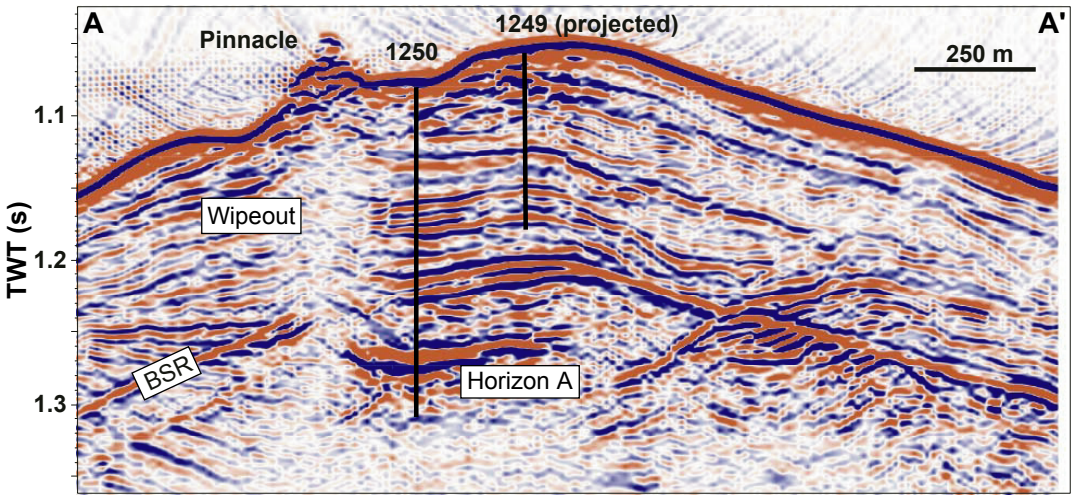

Fig. 2-2: Seismic cross section through the summit (A-A' in Fig. 2-1, modified from [*Trehu et al.*, 2003]. The bottom-simulating reflector (BSR) is a negative-polarity reflection that marks the phase boundary between gas hydrate above and free gas below. A bright, negative-polarity reflection (Horizon A) stretches laterally beneath the BSR. High free gas saturations are present over some distance within Horizon A [*Trehu et al.*, 2004a]. The BSR is disrupted where Horizon A crosses the RHSZ but is continuous elsewhere. A low-amplitude chimney is present above the disrupted BSR and is capped by a seafloor pinnacle. TWT - two-way traveltime.

Hydrate stability depends on pressure, temperature, the gas concentration in the surrounding pore water, and the activity of water [*Sloan*, 1998] (Fig. 2-3). Liquid (subscript L) and gas (subscript G) coexist below the three-phase equilibrium curve, while liquid and hydrate (subscript H) coexist above it (Fig. 2-3C). We define the regional hydrate stability zone (RHSZ) as the zone where hydrate is stable for seawater salinity (550 mM Cl^-). At southern Hydrate Ridge, the base of the RHSZ is predicted to be ~130 meters below seafloor (mbsf) (Fig. 2-3B). Water coexists with hydrate inside the RHSZ, whereas water and free gas are stable below the RHSZ. In this stratified gas hydrate system, the zone of three-phase equilibrium corresponds to a single depth (~130 mbsf) and free gas should not be present within the RHSZ.

However, there is abundant evidence that free gas exists and migrates inside the RHSZ at southern Hydrate Ridge. Venting of methane bubbles at the seafloor indicates rapid passage of methane-rich fluids through the RHSZ [*Heeschen et al.*, 2002]. X-ray computer tomography (CT) studies on near-surface samples record gas within hydrate layers [*Abegg et al.*, 2003]. Hydrate samples collected near the seafloor have a gas bubble texture [*Suess et al.*, 1999]. At ODP (Ocean Drilling Program) Site 1249, a PCS (Pressure Core Sampler) measurement (~14 mbsf) records the presence of *in situ* free gas [*Milkov et al.*, 2004]. Core bulk density measured within a pressurized core taken at the same depth was very low (~0.75 g/cm^3) [*Trehu et al.*, 2003].

Three mechanisms are envisaged for eruption of free gas through the RHSZ. First, gas flow may be out of equilibrium with its surroundings due to kinetic effects [*Haeckel et al.*, 2004; *Torres et al.*, 2004]. Second, hydrate formation may be limited by the availability of water when gas is supplied in excess of its proportion in hydrate [*Ginsburg*

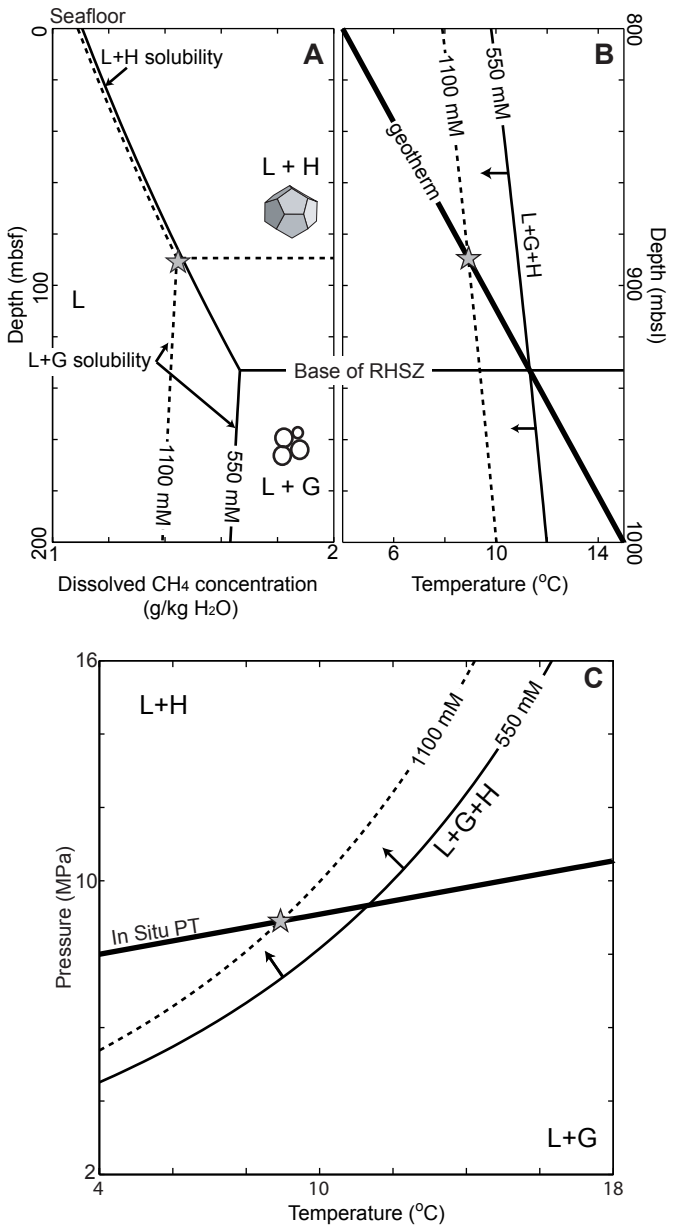

Fig. 2-3: (A) CH_4 solubility, (B) temperature for three-phase equilibrium and (C) hydrate stability P-T phase diagram for salinities of 550 (solid line) and 1100 mM Cl^- (dotted line). Fields of hydrate (H), dissolved (L) and free gas (G) are depicted. (A) Hydrate or free gas is present only when the gas concentration exceeds the solubility. The peak in solubility coincides with the base of the RHSZ for seawater salinity (550 mM Cl^-). (B) The intersection of the geotherm with the temperature for three-phase equilibrium defines the base of the RHSZ. (C) Solid arrows indicate the displacement of the phase boundary when salinity increases. At southern Hydrate Ridge, water depth is ~800 m, pressure gradient is hydrostatic (~10 MPa/km), seafloor temperature is 4 ^oC and geothermal gradient is 55 ^oC/km [*Milkov et al.*, 2004]. mbsf - meters below sea floor; mbsl - meters below sea level.

and Soloviev, 1997; *Clennell et al.*, 1999]. Third, the P-T boundary defining the RHSZ may be perturbed upward by advecting warm fluids [*Wood et al.*, 2002], capillary effects in fine-grained sediments [*Clennell et al.*, 1999; *Henry et al.*, 1999], or high pore water salinity [*Haeckel et al.*, 2004; *Milkov et al.*, 2004; *Torres et al.*, 2004].

We build upon recent suggestions [*Haeckel et al.*, 2004; *Milkov et al.*, 2004; *Torres et al.*, 2004] that hyper-saline pore water shifts the three-phase stability boundary to allow free gas migration through the RHSZ. We present an equilibrium model to describe how the three-phase zone extends to the seafloor throughout the RHSZ and permits methane gas to escape into the ocean. We predict the evolution and distribution of salinity and gas hydrate along the gas migration path. The measured pore water salinities at Site 1249 are corrected to the *in situ* conditions; the corrected salinities in the upper ~50 mbsf agree well with model predictions, indicating that free gas and hydrate coexist *in situ*. We propose that hydrate formation is a self-equilibrating process in marine environments where a large volume of free gas is transported into the RHSZ.

2. Development of an equilibrium model for hydrate formation

2.1 Thermodynamic conditions for hydrate stability

The distribution of hydrate and free gas in the sediment column depends on two P-T dependent equilibrium solubility curves (Fig. 2-3A): (1) the liquid-hydrate (L+H) methane solubility curve where gas hydrate is at equilibrium with dissolved gas in water, and free gas is absent; and (2) the liquid-gas (L+G) methane solubility curve where free gas is at equilibrium with dissolved gas in water, and hydrate is absent. *Duan et al.*'s model [1992] is used to predict the L+G equilibrium. *Henry et al.*'s model [1999] is used

to predict the L+H equilibrium (Appendix A). Comparison of model predictions with the CSMHYD hydrate program [*Sloan*, 1998] shows good agreement.

The L+H solubility increases downward from the seafloor, while the L+G solubility slightly increases upward to the seafloor. At their intersection, three-phase equilibrium is present and CH_4 solubility reaches a maximum (Fig. 2-3A). The base of the RHSZ is located at the three-phase equilibrium for CH_4 + seawater salinity. When dissolved CH_4 concentration exceeds the solubility, hydrate is stable within the RHSZ while free gas is stable below the RHSZ.

Doubling pore water salinity from 550 to 1100 mM Cl^- reduces the L+G solubility by 15%, while the L+H solubility is relatively insensitive to the salinity increase (Fig. 2-3A). As a result, the intersection of the two solubility curves, and hence the base of the hydrate stability zone, shifts upward from 130 to 90 mbsf (Fig. 2-3B). Elevated pore water salinity decreases hydrate stability conditions (Fig. 2-3C).

2.2 Hydrate formation and salinity increase in a box model

We explore how salinity change that occurs during hydrate formation affects hydrate stability. A sediment volume within the RHSZ is initially saturated with seawater (550 mM Cl^-) and local thermodynamic equilibrium is assumed. Pressure and temperature are assumed constant (volume expansion and latent heat of hydrate formation are ignored). Free methane gas is supplied to the sediment volume from below. This system is analogous to natural systems where abundant gas is supplied to sediment of low permeability.

Hydrate, like water ice, excludes dissolved salt during its formation, which increases the salinity of the surrounding pore water [*Hesse and Harrison*, 1981].

Assuming there is no hydrate present initially and that all salts remain dissolved in water, then mass conservation of salts yields the relation between pore water salinity (C), initial salinity (C_i) and hydrate saturation (S_h):

$$C = \frac{C_i}{1 - S_h} . \quad (2\text{-}1)$$

As written, S_h in Eq. 2-1 is the fraction of original pore space filled with hydrate assuming no volume change when the liquid forms hydrate. In fact, because we have assumed constant pressure and temperature, there will be volume expansion, first as the gas and water form hydrate and second as gas continues to be added after three-phase stability is achieved. *Xu* [2002; 2004] treated this problem more rigorously.

With addition of methane, the system evolves from a single phase (L) to two phases (L+H), to three phases (L+H+G) (Fig. 2-4). Initially all the methane is dissolved in water (L) and hydrate is absent. As methane is added, the methane concentration increases until it reaches the L+H solubility limit whereupon hydrate forms. Thereafter, the amount of methane in solution is limited by the solubility (Fig. 2-4D) and additional methane is transferred to the growing hydrate phase (Fig. 2-4A). During the L+H stage, the liquid is progressively enriched in salt with continued hydrate formation as described by Eq. 2-1 (Fig. 2-4B). The L+H solubility decreases slightly while the L+G solubility decreases significantly (Fig. 2-4D). The increase in salinity causes an increase in the fugacity of methane in the liquid phase ($f_L^{CH_4}$) (Fig. 2-4C).

Once the fugacity of methane in solution ($f_L^{CH_4}$) equals that of gaseous methane ($f_G^{CH_4}$) (Fig. 2-4C), three-phase equilibrium between hydrate, salt solution and free gas is achieved. The L+G and L+H methane solubilities are the same at three-phase equilibrium

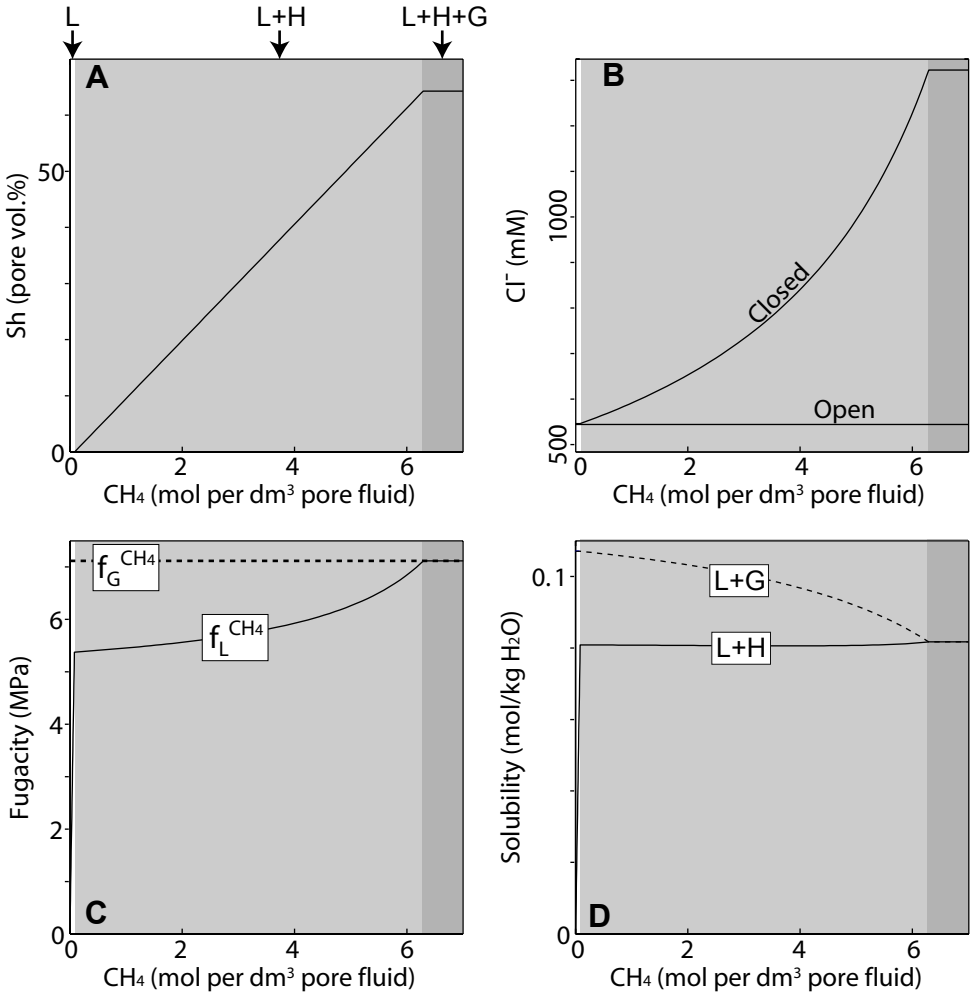

Fig. 2-4: Changes in (A) hydrate saturation, (B) salinity, (C) dissolved CH_4 fugacity and (D) concentration as CH_4 is added (in mol per dm^3 of pore fluids) to a sediment volume at 50 mbsf (P=8.5 MPa, T=6.75 ^oC) from southern Hydrate Ridge. Single-phase (L), two-phase (L+H) and three-phase (L+G+H) fields are indicated by white, gray and dark areas respectively. Dashed lines in (C) and (D) indicate the fugacity and concentration of dissolved CH_4 that would be in equilibrium with free gas if hydrate did not form.

(Fig. 2-4D). At this critical state, there is no further hydrate formation and any additional methane is present in the gas phase.

2.3 Hydrate formation by upward migration of free gas in a sediment column

We next describe how hydrate saturation and salinity evolve in a sediment column that is initially filled with seawater (Fig. 2-5). Free gas is supplied from below the RHSZ. We assume vertical gas flow, local thermodynamic equilibrium, that there is no water flux, and that there is no large-scale diffusion. Volume change and latent heat of hydrate formation are not considered; thus the temperature gradient is assumed constant and the pressure profile is assumed hydrostatic.

Initially, gas enters the base of the RHSZ and becomes hydrated. As hydrate forms, pore water salinity increases until free gas can coexist with hydrate (Figure 5, Time 1). At this point, gas migrates further upward and hydrate forms at successively shallower depths (Fig. 2-5, Time 2). A sharp front in hydrate saturation and salinity is present at the top of the gas invasion zone and it moves upward with time. Ultimately, the three-phase zone expands to the seafloor (Fig. 2-5, Time 3). At this point, there is a steady gas flow from below the RHSZ to the seafloor, the system is everywhere in three-phase equilibrium, and gas is vented into the ocean.

This process of hydrate formation is termed a flow-controlled front reaction [*Phillips*, 1991]. Hydrate is formed as an advancing reaction front that separates the three-phase stability region behind from the unaltered region ahead. Behind the front, the water available for hydrate formation is not completely depleted, but the high salinity of the residual water prevents its reaction with gas to form more hydrate at the ambient P-T conditions. Hydrate formation only occurs at the reaction front where both water and gas

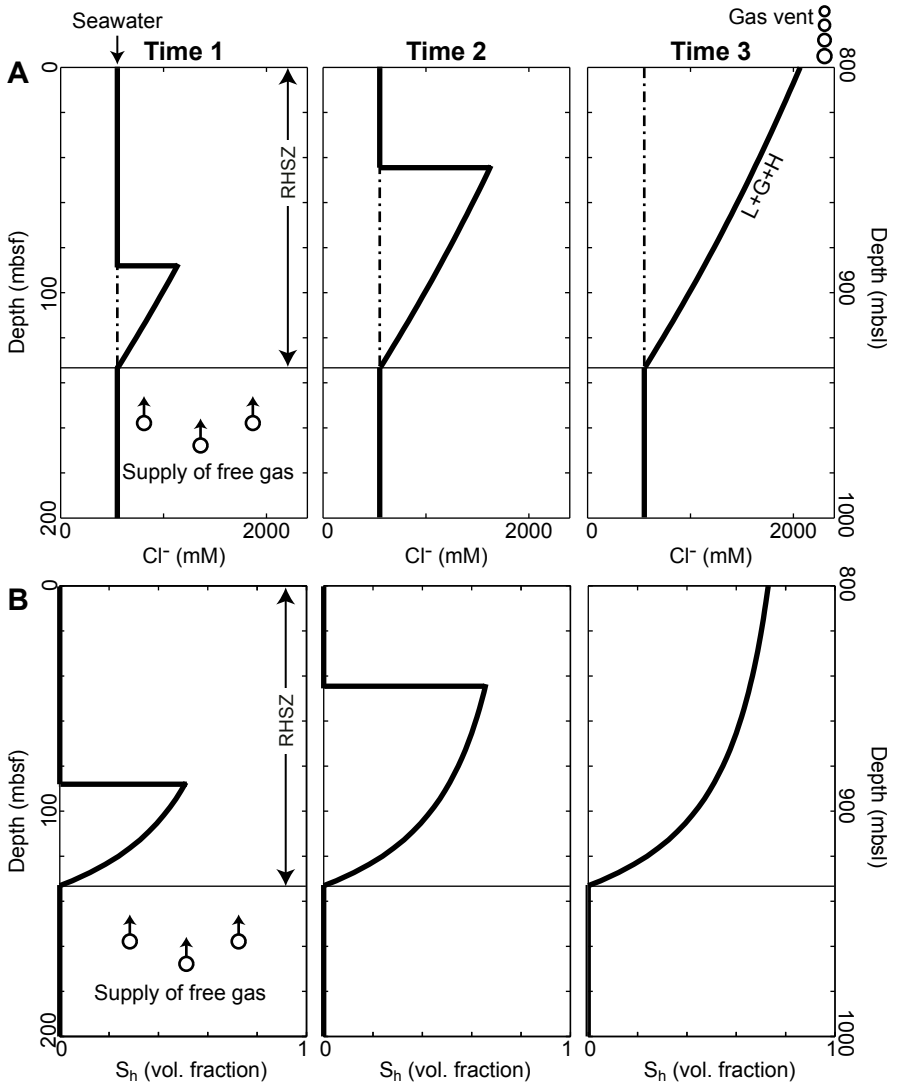

Fig. 2-5: Evolution of (A) salinity and (B) hydrate saturation in a sediment column due to the sustained gas flux from below. Initially, free gas migrates upward into the RHSZ and becomes hydrated at the base. Salinity increases due to the exclusion of salt from hydrate. Gas migrates upward further once the salinity is elevated to the point where three phases coexist. The salinity front grows with time from the base of the RHSZ towards the seafloor. A steady state profile eventually develops when the gas invasion zone reaches the seafloor and a gas vent is formed.

(i.e., reactants) are available. Ultimately, the reaction front propagates to the seafloor. In this model hydrate formation is essentially limited by the availability of pure water.

The salinity necessary for three-phase equilibrium increases upward toward the seafloor (Fig. 2-5). Near the base of the RHSZ, the P-T conditions are close to the expected three-phase boundary for seawater salinity. Thus only a small amount of hydrate forms before salinity builds enough to achieve three-phase equilibrium. In contrast, the P-T conditions at the seafloor are furthest away from the expected three-phase boundary for seawater salinity. The salinity required for three-phase equilibrium is not achieved until hydrate saturation increases to ~70%.

When the three-phase zone reaches the seafloor, there is a steady state (Fig. 2-5, Time 3): methane released at the seafloor equals that delivered at the base of the RHSZ and no more hydrate accumulates. The steady-state hydrate saturation and salinity profiles are independent of the gas supply rate and depend only on pressure and temperature. The gas flux does control the rate at which the three-phase zone propagates to the seafloor.

We can test the assumption of local equilibrium through calculating the equilibration length (l_e) [*Phillips*, 1991], which is

$$l_e = \frac{u_g}{\gamma}, \quad (2\text{-}2)$$

where u_g is the gas Darcy velocity and γ is the reaction rate constant. l_e is the characteristic distance in the flow direction over which free gas remains out of equilibrium with its surroundings. If l_e is much smaller than the model dimensions, non-equilibrium effects are negligible. Experiments on hydrate formation suggest that $\gamma \approx 10^{-3}$ s^{-1} [*Rempel and Buffett*, 1997] and the distance between the BSR and the seafloor is on

the order of 100 m. Under these conditions, the Darcy velocity must be much less than 0.1 m s^{-1} for local equilibrium to be present.

We also assumed no large-scale diffusion. In fact, there is a vertical zone of elevated salinity through which gas is being transported within the RHSZ. Lateral diffusion of Cl^- will occur from this saline gas chimney to the bounding normal salinity pore water. Loss of salt through lateral diffusion would shift the thermodynamic equilibrium, allow more hydrate formation [*Torres et al.*, 2004], and deplete upward gas flow. If vertical gas supply far exceeds gas depletion that is caused by lateral diffusion of salt (Appendix B), then hydrate formation will rapidly propagate upward and the lateral diffusion of salt from the sides of the gas chimney can be neglected. Thus when gas flux is high, the inherently three-dimensional problem of a gas chimney can be approximated by the one-dimensional model. In contrast, if lateral diffusion of salt outpaces gas supply from below, then three-phase equilibrium cannot be sustained. As a result, the chimney will be restricted to the lower part of the RHSZ and free gas will not reach the seafloor.

3. Application to southern Hydrate Ridge

3.1 ODP Site 1249

ODP Site 1249 was drilled on the summit of southern Hydrate Ridge to a depth of 90 mbsf (Fig. 2-2). The BSR at this site is at ~115 mbsf. Sediments are mainly composed of clay and silty clay [*Trehu et al.*, 2003] and the permeability measured at Site 1244 is low, ranging from 1.5×10^{-16} to 3×10^{-17} m^2 [*Tan et al.*, submitted].

Log and core data from Site 1249 suggest that massive hydrate lenses extend to 30 mbsf near the summit of southern Hydrate Ridge (Fig. 2-6). The caliper log indicates an oversized borehole that may be associated with dissociated hydrate in the upper 10

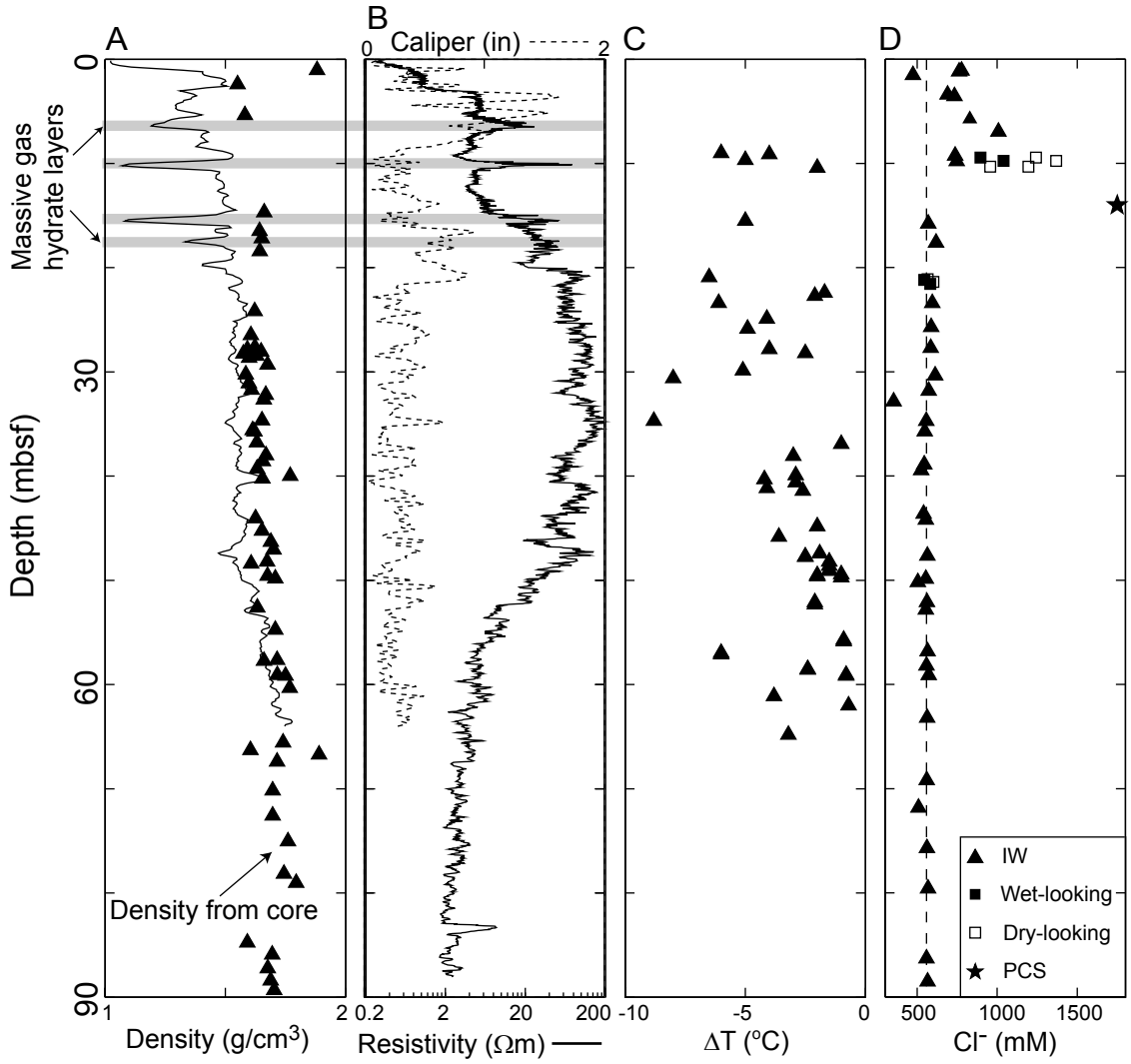

Fig. 2-6: Core and log data from ODP Site 1249. (A) LWD bulk density and MAD core density. (B) LWD deep resistivity (solid line) and caliper log (dashed line). (C) Negative temperature anomalies (measured immediately after core recovery). (D) Chloride concentrations. Standard whole-round samples (triangle) and selected wet- (closed square) and dry-looking (open square) samples are shown. The in situ salinity is also estimated from the Pressure Core Sampler (PCS; star). Dashed line indicates seawater salinity (550 mM Cl^-).

mbsf (Fig. 2-6B). Between 10 and 20 mbsf, several massive gas hydrate layers have high resistivities (20 to 100 Ωm) and low formation densities (as low as 1.1 g/cm^3). Pressurized cores recovered from 8 and 14 mbsf indicate hydrate pore volume saturations of ~45% [*Trehu et al.*, 2004b]. Negative thermal anomalies, probably caused by adiabatic gas expansion and/or endothermic hydrate dissociation, are commonly measured (Fig. 2-6C).

Below 30 mbsf, logs reveal a 20-m-thick, high-resistivity zone with peak values exceeding 160 Ωm at 35 mbsf (Fig. 2-6B). Thermal anomalies and mousse-like textures resulting from hydrate dissociation are observed throughout this interval. Surprisingly, the PCS core recovered from 34 mbsf only contains hydrate of ~5% pore volume [*Trehu et al.*, 2004b] (Fig. 2-7A). Core recovery improved significantly below 30 mbsf.

Pore fluids collected from the upper 20 mbsf at Site 1249 are enriched in Cl^- (Fig. 2-6D). *Torres et al.* [2004] described how these interstitial water (IW) samples were obtained and showed that pore water chlorinity reaches 1008 mM at ~7 mbsf. Pairs of wet and adjacent dry sediment intervals were analyzed immediately after retrieval [*Torres et al.*, 2004]. Pore fluids in the dry-looking samples have a Cl^- maximum of 1368 mM at ~10 mbsf. *Milkov et al.* [2004] estimated *in situ* salinity and gas concentration through degassing a PCS core (~14 mbsf; star in Fig. 2-6D) and found that the *in situ* salinity (~1750 mM Cl^-) approximates the value required for three-phase equilibrium at that depth. Below 20 mbsf, high-chloride brines give way to the low-chloride anomalies.

3.2 ODP Site 1249: *In situ* salinity and water saturation

Pore water salinities measured from IW samples record both the *in-situ* salinity and a freshening component due to hydrate dissociation during retrieval [*Trehu et al.*,

2003]. The *in situ* salinity may be calculated from a combination of electrical resistivity log, core-derived porosity and pore fluid salinity [*Hyndman et al.*, 1999].

Archie's law describes the relation between formation resistivity (R_t) and water saturation (S_w):

$$S_w^{\,n} = \frac{aR_w}{\phi^m R_t}, \quad (2\text{-}3)$$

where n is the saturation exponent, a is the tortuosity coefficient and m is the cementation coefficient. The core-derived porosity ϕ is known from shipboard moisture and density measurements [*Trehu et al.*, 2003]. We derive a and m by cross-plotting LWD resistivity vs. core-derived porosity from Site 1250 below the BSR where there is no free gas (i.e., $S_w = 1$) and pore fluid salinity is assumed to equal that of seawater. We find a=3.65 and m=0.5. These parameters are close to that derived from ODP Site 891 (a=5.8, m=0.8) [*Spangenberg*, 2001]. At relatively low S_w, the water phase may form discrete drops within the pores [*Spangenberg*, 2001] and n is relatively high. We take n=1.9386 [*Collett and Ladd*, 2000] for Site 1250 and n=4 [*Spangenberg*, 2001] for Site 1249. The latter value is high because Site 1249 is inferred to have low S_w.

We use an iterative method to estimate *in situ* salinity (C_{insitu}) and water saturation, because C_{insitu} affects the resistivity. Pore-water resistivity (R_w) is calculated as a function of temperature and salinity [*Schlumberger*, 1989]. The core-measured salinity (C_{IW}) and its associated pore-water resistivity are initially input into Eq. 2-3 to obtain S_w. We assume that the dissociated hydrate produces an equal volume of freshwater; thus we use $C_{insitu}=C_{IW}/S_w$ to estimate the *in situ* salinity. Pore-water resistivity changes accordingly and S_w is recalculated. The iterative process is continued

until the *in situ* salinity and water saturation do not change. The solution generally converges after a few iterations.

We calculate that $1\text{-}S_w$ ranges from 20 to 80% at Site 1249 (triangle in Fig. 2-7A). $1\text{-}S_w$ rapidly increases from the seafloor to 80% at 20 mbsf and there is a spike at 10 mbsf. Between 20 and 50 mbsf, $1\text{-}S_w$ is ~80%. Beneath 50 mbsf, $1\text{-}S_w$ decreases to 20%. Compared to the iterative method, the standard Archie calculation with the measured salinity (solid line in Fig. 2-7A) [*Collett and Ladd*, 2000] underestimates $1\text{-}S_w$ by 5-10%.

The sediment pores must be filled with water, hydrate and/or free gas *in situ*. However, resistivity alone cannot distinguish the fraction of the pore space not filled with water ($1\text{-}S_w$), because both free gas and hydrate have high resistivity [*Trehu et al.*, 2004b]. *Milkov et al.* [2004] indicated that the pore space at 14 mbsf from Site 1249 had 40% hydrate and 10% free gas. *Schowalter* [1979] determined experimentally that 10% gas saturation is required for gas migration in shale. Our best estimate is that gas saturation is equal to or more than 10%; thus hydrate saturations are less than 70% at Site 1249.

The *in situ* salinity is much higher than that measured by pore-water squeezing (Fig. 2-7B). The zone between the seafloor and 50 mbsf has Cl^- concentrations of up to 2600 mM. In this zone, the *in situ* salinity gradually decreases with depth and the values are in general agreement with salinities inferred from a PCS core (star in Fig. 2-7B) [*Milkov et al.*, 2004]. Below this zone, there is an abrupt downward decrease in salinity and in $1\text{-}S_w$.

We interpret that three phases (gas, hydrate and water) coexist from the seafloor to 50 mbsf at Site 1249 (gray area in Fig. 2-7). In this zone, the *in situ* salinity falls near

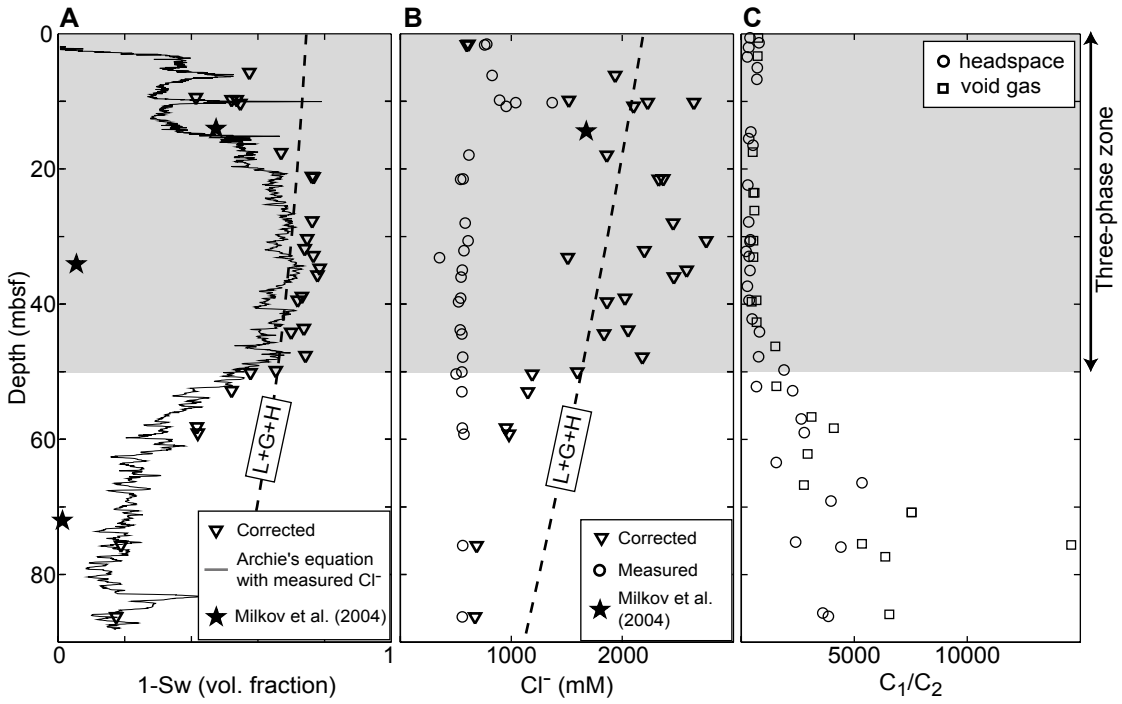

Fig. 2-7: Interpretation of ODP Site 1249. (A) 1-S_w determined from the in situ salinity (triangle), the measured salinity (solid line) and the Pressure Core Sampler (PCS) measurement (star). (B) Measured (circle) vs. corrected (triangle) pore water salinity. Dashed line denotes salinity at three-phase equilibrium. Shaded area represents the three-phase zone. (C) C_1/C_2 ratio in gas void (square) and headspace (circle). Note that the BSR was not penetrated at this site.

the three-phase equilibrium curve. However, beneath 50 mbsf, the *in situ* salinity is below the three-phase equilibrium curve and only two phases (hydrate and water) coexist.

3.3 ODP Site 1250: *In situ* salinity and water saturation

ODP Site 1250 was drilled 350 m southwest of ODP Site 1249 and 100 m east of the Pinnacle (Fig. 2-2). Site 1250 has a high-resistivity zone (~3 Ωm) near the seafloor (Fig. 2-8B). Core recovery from this interval was poor. Below this interval, resistivity increases with depth and there are zones of high resistivity. Extensive cold anomalies are present (Fig. 2-8C), but poor core recovery limits detection of near-surface hydrate.

The pore fluids recovered from the upper 20 mbsf at Site 1250 also show Cl^- enrichment (Fig. 2-8D); however, it is significantly lower than the enrichment measured at Site 1249. Cl^- reaches a maximum value of 613 mM at 13.9 mbsf. Below 30 mbsf, the Cl^- concentration is less than that of seawater. We use Eq. 2-3 to calculate $1\text{-}S_w$ as described for Site 1249. At Site 1250, hydrate is concentrated in a 10-m-thick zone just below the seafloor and the maximum $1\text{-}S_w$ approaches 40% (Fig. 2-9A). Below this interval, hydrate is distributed over a broad depth range and $1\text{-}S_w$ increases from approximately zero at 40 mbsf to 20% at the BSR (~114 mbsf).

The *in situ* salinity is lower at equivalent depths at Site 1250 than at Site 1249. The *in situ* salinity at Site 1250 only slightly exceeds the measured salinity (Fig. 2-9B), even in the near-surface hydrate zone. The *in situ* salinity falls below the three-phase equilibrium curve, indicating that only hydrate and water should coexist above the BSR at Site 1250.

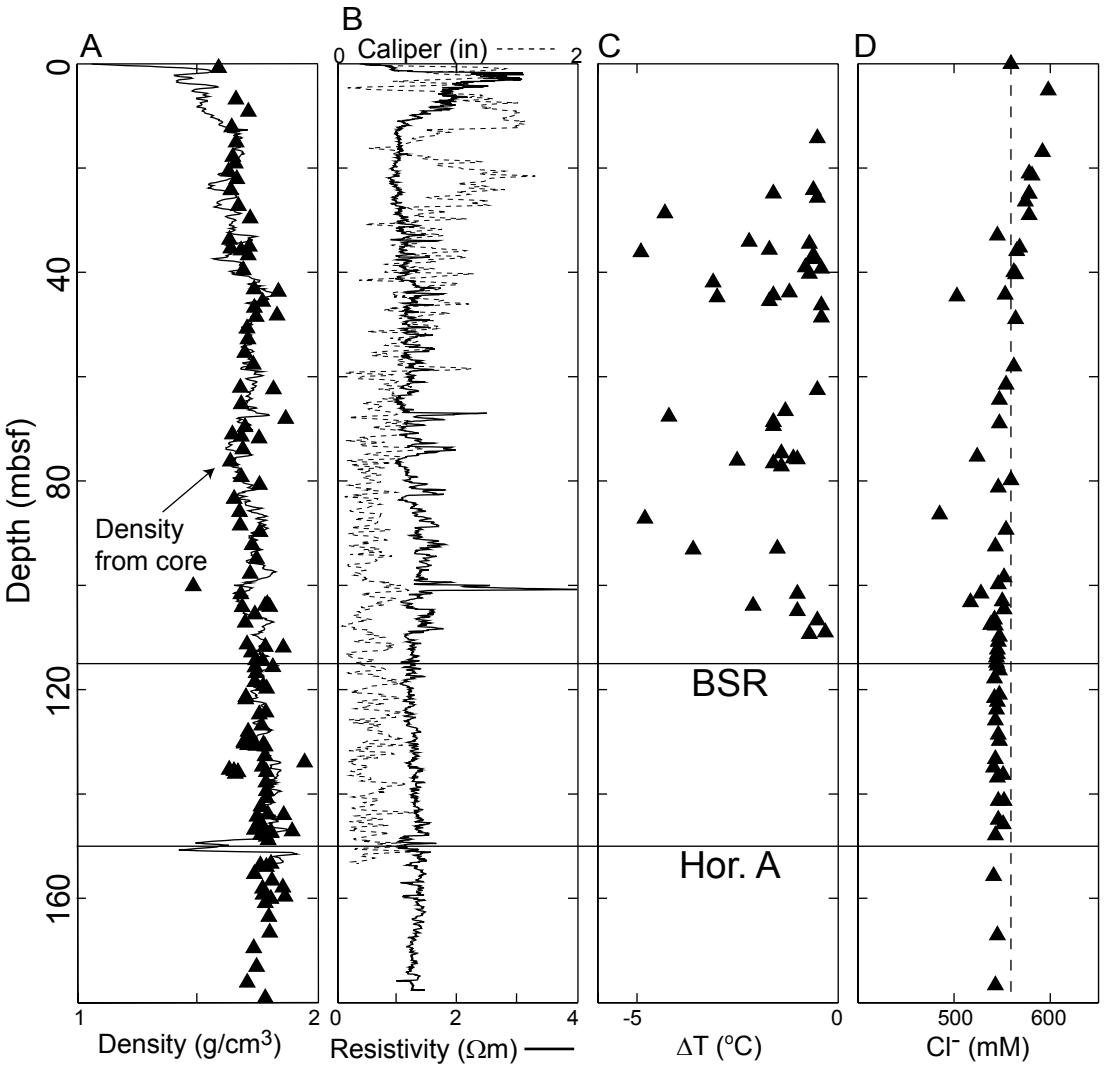

Fig. 2-8: Core and log data from ODP Site 1250. (A) LWD bulk density and MAD core density. (B) LWD deep resistivity (solid line) and caliper log (dashed line). (C) Negative temperature anomalies (measured immediately after core recovery). (D) Chloride concentrations. Standard whole-round samples (triangle) are shown. Dashed line indicates seawater salinity.

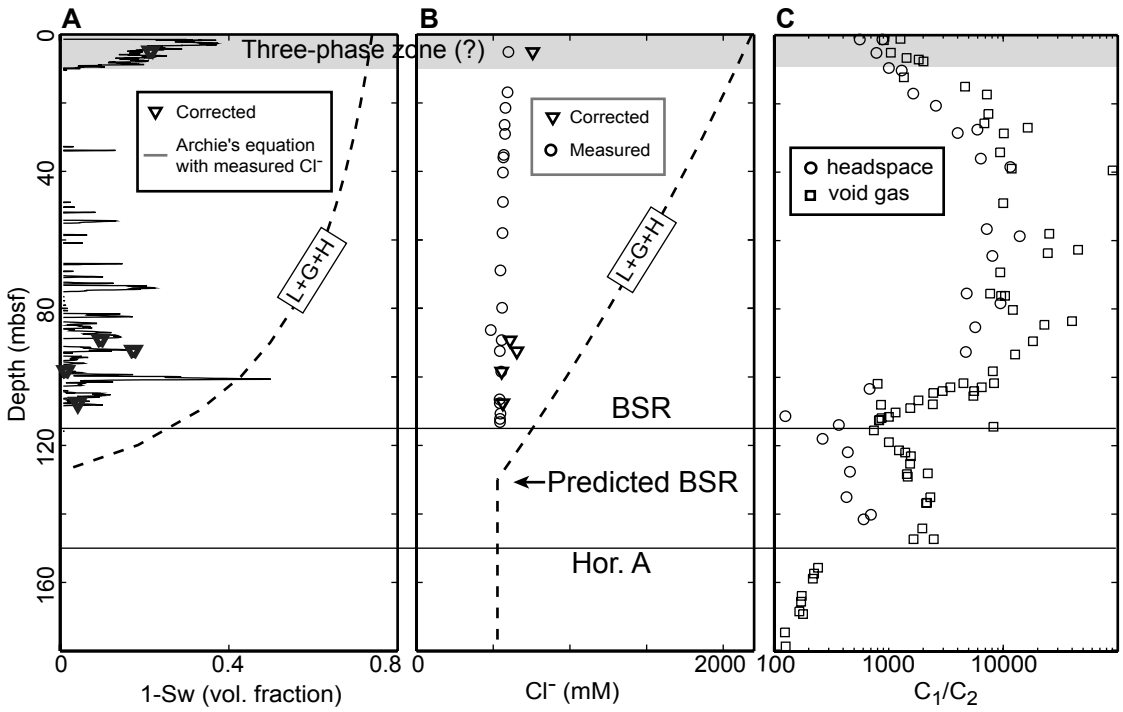

Fig. 2-9: Interpretation of ODP Site 1250. (A) 1-S_w determined from the in situ salinity (triangle), the measured salinity (solid line). (B) Measured (circle) vs. corrected (triangle) pore water salinity. Dashed line denotes salinity at three-phase equilibrium. The in situ salinity is not sufficient for three-phase equilibrium. (C) C_1/C_2 ratio in gas void (square) and headspace (circle).

4. Discussion

We have presented a model to describe how marine gas hydrate systems with abundant gas supply create local equilibrium conditions that allow free gas migration through the hydrate stability zone. Focused gas flow generates a local, moving, three-phase reaction front. The pore water salinity is buffered at the equilibrium value: hydrate forms until salinity increases to the point where free gas is stable and thereafter, gas migrates through the zone. The model provides a simple explanation for the presence of free gas within the RHSZ, does not rely on kinetics [*Torres et al.*, 2004], and extends studies that suggest free gas is present within the RHSZ as a result of elevated salinity [*Milkov et al.*, 2004; *Torres et al.*, 2004].

We document a zone of three-phase stability between the seafloor and 50 mbsf at ODP Site 1249 and suggest that there is a zone of three-phase stability from the BSR to the ridge crest where gas is venting today. The high salinity hypothesis is linked to observations of seismic wipeout zone located beneath the Pinnacle. Although southern Hydrate Ridge is a specific case, this model may apply to other settings where free gas migration within the hydrate stability zone has been inferred, such as the Gulf of Mexico [*MacDonald et al.*, 1994], the Cascadia margin offshore Vancouver [*Wood et al.*, 2002], the Caspian Sea [*Ginsburg and Soloviev*, 1997] and the Blake Ridge [*Paull et al.*, 1995; *Taylor et al.*, 2000].

4.1 Comparisons to other hydrate formation models

Previous hydrate formation models assumed that methane is transported only in the liquid phase by diffusion and slow advection [*Rempel and Buffett*, 1997; *Xu and Ruppel*, 1999; *Davie and Buffett*, 2001; *Davie and Buffett*, 2003]. This hydrate

accumulation process is termed a flow-controlled gradient reaction [*Phillips*, 1991].These two-phase (hydrate and water + dissolved gas) models are only appropriate for low-methane flux regions. In these models, the change in solubility within the RHSZ is too small to generate a significant hydrate concentration and consequently no excess salinity is generated. Hydrate is concentrated at the base of the hydrate stability zone where the solubility gradient is greatest [*Rempel and Buffett*, 1997; *Xu and Ruppel*, 1999]. In contrast, we suggest that where methane flux is high, it is transported as a separate gas phase under buoyancy. Hydrate formation is limited by salt buildup and not by methane supply, free gas is present throughout the RHSZ, gas actively vents the surface and hydrate precipitates at or near the seafloor. In this model, salinity and hydrate saturation increase upward towards the seafloor.

4.2 Two-dimensional free gas migration at southern Hydrate Ridge

The model presented here is one-dimensional, with gas supplied from below. At southern Hydrate Ridge, the flow path is multi-dimensional (Fig. 2-10). *Trehu et al.* [2004a] suggested that beneath the BSR, gas is focused laterally along a high-permeability layer named Horizon A. Gas accumulated in Horizon A below the RHSZ until its high pressure forced gas to migrate upward into the RHSZ. The elevated gas pressure fractured the hydrate-bearing sediments and transported gas upward through the hydrate layer. We suggest that gas migrated vertically below the Pinnacle. The BSR was disrupted and the low-amplitude chimney was caused by upward migration of free gas (Fig. 2-2). Subsequently, gas flow was diverted laterally by near-surface low-permeability carbonate layers to the ridge summit where gas is actively venting at present (Fig. 2-10) [*Heeschen et al.*, 2002].

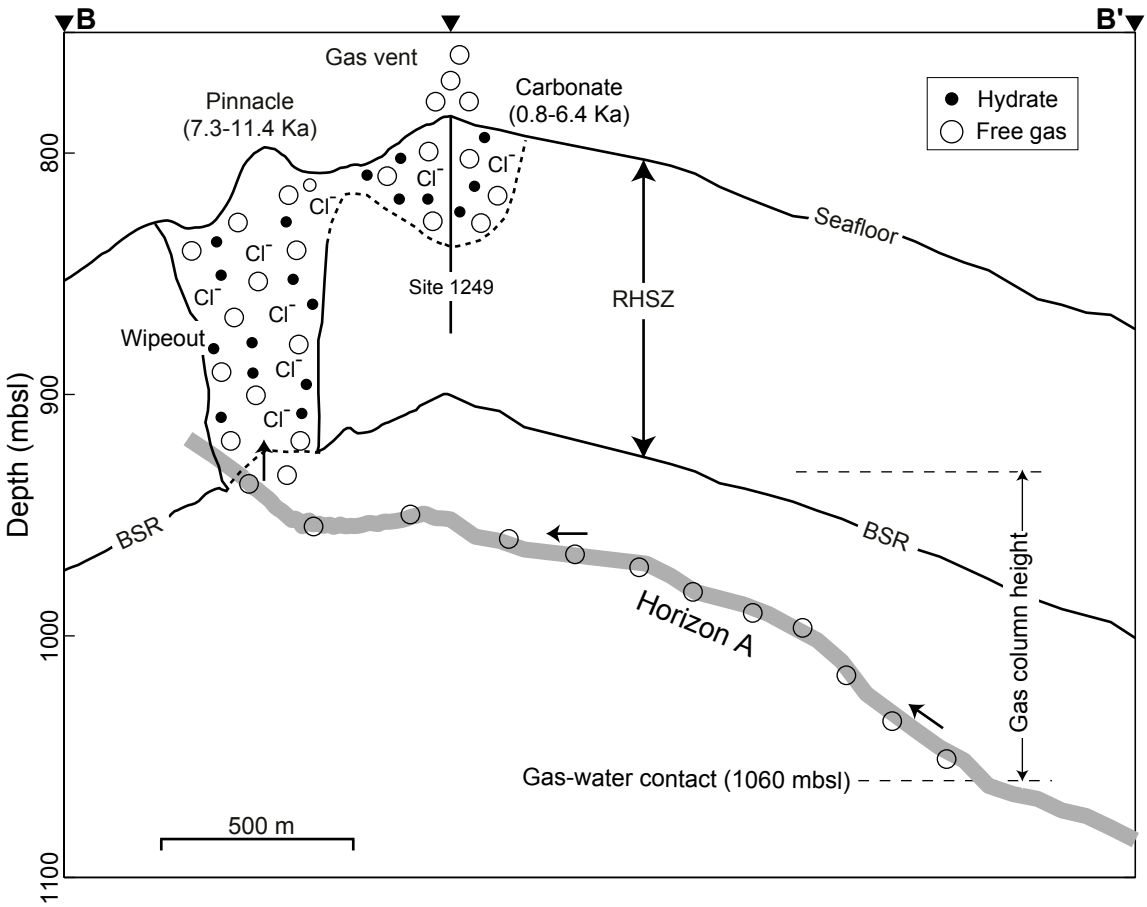

Fig. 2-10: Schematic diagram of the dynamic hydrate/free gas system at southern Hydrate Ridge (B-B' in Fig. 2-1). Free gas migrates up the conduit (i.e., Horizon A) under a strong buoyancy force and first become hydrated where Horizon A crosses the RHSZ. Gas is trapped beneath this hydrate seal until the pressure at the top of the gas column is high enough to drive gas into the RHSZ. High gas flux from Horizon A initiates rapid hydrate formation and pore water salinity is increased to the point where free gas will locally be thermodynamically stable. The massive, near-surface carbonate deposits form an impermeable barrier. As a result, the gas rising from depth is laterally diverted to the crest.

Sediments at southern Hydrate Ridge contain mainly microbial C_1 but C_{2+} hydrocarbon gases of thermogenic origin are also present. The three-phase zones are enriched in C_2. At Site 1249, the C_1/C_2 ratio is constant (<1000) in the three-phase stability zone (0-50 mbsf) and then abruptly increases down to the base of the cored section (~5000) (Fig. 2-7C). The near-surface hydrate zone (0-10 mbsf) at Site 1250 also has low C_1/C_2 ratios (Fig. 2-9C). Horizon A penetrated at Site 1250 also reveals C_2 enrichment (Fig. 2-9C) and the C_1/C_2 ratios are similar to those in the three-phase zone at Sites 1249 and 1250. We interpret that C_{2+} hydrocarbon gases are supplied to the base of the RHSZ from the deeper permeable Horizon A (Fig. 2-10) and that zones of C_2 enrichment represent the gas migration pathway.

Steady gas venting requires three-phase equilibrium along the entire migration path. Although Site 1250 lies between the Pinnacle and the summit (Fig. 2-2), the *in situ* salinity is not sufficient to stabilize free gas (Fig. 2-9B). We suggest that the three-phase zone may exist in the upper 10 mbsf at Site 1250 for three reasons. First, borehole conditions were especially degraded near the top (Fig. 2-8B), resulting in large-scale, negative shifts in the electrical resistivity log. Second, the sulfate-methane interface is very near the seafloor [*Trehu et al.*, 2003], typical of the influence of free gas. Third, the near-surface zone at Site 1250 (Fig. 2-9C) has anomalously low C_1/C_2 ratio similar to the three-phase zone at Site 1249 (Fig. 2-7C).

Southern Hydrate Ridge may have evolved from an early phase where methane-rich water vented to the present-day phase where gas is venting. During early gas accumulation, methane-rich water was vertically displaced from Horizon A to the seafloor and this aqueous flow may have formed the Pinnacle. Later, sufficient gas

entered the hydrate stability zone to create a gas pathway to the Pinnacle. However, low permeability at the Pinnacle drove flow laterally resulting in venting at the summit. However, massive authigenic carbonates are not present at the summit [*Trehu et al.*, 1999], suggesting that focused gas venting has recently begun here. The evolution from methane-rich water to gas venting is consistent with variations in the age of the authigenic carbonates from the Pinnacle (7.3-11.4 Ka) to the summit (0.8-6.4 Ka) (Fig. 2-10) [*Teichert et al.*, 2003].

4.3 Scaling arguments

We have approximated gas flow through the regional hydrate stability zone as a one dimensional process, where local equilibrium is present, where there is no long range diffusion, where there is only gas flow, and where latent heat of hydrate formation can be ignored. We defend these assumptions with scaling arguments. The gas flux out of the crest of southern Hydrate Ridge is estimated to be ~10^2 mol CH_4 m^{-2} $year^{-1}$ [*Torres et al.*, 2004]. This corresponds to a gas Darcy velocity of ~10^{-9} m s^{-1}, assuming a gas density of 62.8 kg m^{-3} [*Trehu et al.*, 2004a]. The equilibration length (l_e) is only ~10^{-6} m (Eq. 2-2), much smaller than the thickness of the hydrate stability zone. Thus, the assumption of local thermodynamic equilibrium is valid. In the Appendix B, we calculate that gas depletion rate caused by loss of salt (<10 mol CH_4 m^{-2} $year^{-1}$) is far less than gas supply rate (~10^2 mol CH_4 m^{-2} $year^{-1}$); thus the assumption of no large-scale diffusion is appropriate.

The model assumes a constant temperature gradient. Heat advection by the gas flow and the heat released by crystallization of hydrate could perturb this constant gradient. The thickness of the RHSZ (Δz) is 120 m, the gas flux (q_g) is 10^2 mol CH_4 m^{-2}

year^{-1} [*Torres et al.*, 2004], the thermal conductivity (K) is ~1.0 W m^{-1} °C^{-1} [*Trehu et al.*, 2003] and the gas heat capacity (c_g) is 3.5 kJ kg^{-1} °C^{-1} [*Xu*, 2002]. In this case the Peclet number ($Pe=q_g c_g \Delta z/K$) is ~0.02 and thus advection of heat can be neglected [*Cathles and Chen*, 2004]. If the latent heat of crystallization of hydrate (L) is 42.1 kJ kg^{-1} [*Cathles and Chen*, 2004] and the normal heat flow at southern Hydrate Ridge is ~55 mM m^{-2} (the thermal conductivity is ~1.0 W m^{-1} °C^{-1} [*Trehu et al.*, 2003] and the geothermal gradient is 55 °C km^{-1} [*Torres et al.*, 2004]), the heat added by hydrate formation at the reaction front ($q_e=7.5q_gL$) is ~16 mW m^{-2}, which is a significant fraction of the normal heat flow. Thus the latent heat of hydrate formation may cause significant deviation from the linear thermal gradient in a one-dimensional model.

However, we interpret that a large fraction of the released latent heat will be dissipated laterally from the gas chimney. We estimate that it takes ~30 years to fill a sediment volume (1 m thickness and 150 m half-width) at 50 mbsf with hydrates (~65% of pore volume). Upon formation, this amount of hydrate laterally releases ~10^6 kJ of heat to the surrounding. If the heat capacity per unit volume of sediment is 2.3 J cm^{-3} °C^{-1} [*Cathles and Chen*, 2004] and the thermal diffusivity is 10^{-6} m^2 s^{-1} [*Rempel and Buffett*, 1997], the positive thermal anomaly of the gas chimney decays to less than 1 °C in 30 years [*Turcotte and Schubert*, 2002].

The model also assumes a hydrostatic pressure gradient and no water flow. However, the positive volume change of hydrate formation will drive flow. In fact, the associated flow is very small since methane hydrate density is only ~8% lower than water density [*Sloan*, 1998]. Variations in salinity and water density across the hydrate zone may generate a density-driven convection below the seafloor. We assume the water

viscosity (μ_w) is 10^{-3} Pa·s, the chemical diffusivity (D) is 10^{-9} m^2 s^{-1} [*Rempel and Buffett*, 1997], the permeability (k) is 10^{-16} m^2 [*Tan et al.*, submitted], the thickness of the RHSZ (Δz) is 120 m, and the water density difference between the seafloor and the base of the RHSZ ($\Delta\rho_w$) is 75 kg m^{-3}. The Rayleigh number ($Ra=\Delta\rho_w k\Delta z/\mu_w D$) is only ~0.9, which is not sufficient to initiate a convection [*Turcotte and Schubert*, 2002].

Finally, we assume no basal water flux at southern Hydrate Ridge. This assumption is justified for two reasons: the gas is more mobile and it has a much larger driving force. Fluid mobility is proportional to relative permeability and inversely proportional to viscosity [*Trehu et al.*, 2004a]. The gas viscosity is at least 10 times the water viscosity and because the gas saturation in Horizon A is large (up to 90%), its relative permeability will be significantly more than the water relative permeability [*Trehu et al.*, 2004a]. Finally, while the gas flow is driven by its own buoyancy, the water flow must be driven by elevated pressure in the water phase. Limited measurements suggest hydrostatic water pressures [*Dugan*, 2003] and thus no driving force for water flow. In sum, it is reasonable to assume the gas flux will greatly exceed the water flux in the gas vent zone.

4.4 Implications for hydrate reservoir stability

We propose that there is a direct pathway for free gas migration from the free gas zone beneath the RHSZ to the seafloor and that this migration pathway forms very rapidly. As a result, significant amounts of gaseous methane can bypass the RHSZ without forming hydrate. Thus, in areas where gas flow is focused, such as Hydrate Ridge, significant amounts of free gas may enter the ocean without forming hydrate, which changes the expected behaviors of the hydrate capacitor [*Dickens*, 2003]. In

addition, hydrate at three-phase equilibrium is more susceptible to environmental changes than hydrate that forms in the two-phase region. In our model, all the hydrates are already at the three-phase boundary, so they would respond easily and rapidly to bottom-water warming or sea-level lowering during climate change.

5. Conclusions

Free methane gas is venting through the regional hydrate stability zone (RHSZ) at southern Hydrate Ridge. Free gas supplied from below forms hydrate, depletes water and elevates salinity until pore water is too saline for further hydrate formation. This system self-generates local three-phase equilibrium and allows free gas migration to the seafloor. Log and core data document a zone of three-phase stability between the seafloor and 50 mbsf at ODP Site 1249. We suggest that there is a zone of three-phase stability from the disrupted BSR to the ridge crest where gas is venting today. This process provides a mechanism for gas venting through the hydrate stability zone that is observed around the world. In these settings, the RHSZ is no longer a thermodynamic barrier to free gas migration.

Nomenclature

g – free gas phase
h – hydrate phase
l – liquid phase
m – methane
w – water
Δz – thickness of RHSZ (L)
ϕ – porosity (dimensionless)
ρ_h – hydrate density (ML^{-3})
ρ_w – water density (ML^{-3})

μ_w – water viscosity ($ML^{-1}T^{-1}$)

a – tortuosity coefficient (dimensionless)

b – half-width of chimney (L)

c_g – gas heat capacity ($L^2T^{-2}\Theta^{-1}$)

f – fugacity ($ML^{-1}T^{-2}$)

k – permeability (L^2)

l_e – equilibration length (L)

m – cementation coefficient (dimensionless)

n – saturation exponent (dimensionless)

q_e – heat flux (MT^{-3})

q_g – gas flux ($ML^{-2}T^{-1}$)

z – depth below seafloor (L)

C – salinity (dimensionless)

D – chemical diffusivity (L^2T^{-1})

F – formation factor (dimensionless)

K – thermal conductivity ($MLT^{-3}\Theta^{-1}$)

L – latent heat (L^2T^{-2})

P – pressure ($ML^{-1}T^{-2}$)

R_w – formation water resistivity ($ML^3T^{-2}A^{-2}$)

R_t – formation resistivity ($ML^3T^{-2}A^{-2}$)

S_g – gas saturation (dimensionless)

S_h – hydrate saturation (dimensionless)

S_w – water saturation (dimensionless)

T – temperature (Θ)

Chapter 3

NUMERICAL MODELING OF HYDRATE FORMATION IN MARINE SEDIMENTS

Abstract

We develop a multi-component, multi-phase fluid and heat flow model for hydrate formation in marine sediments. Methane is mainly transported as a continuous gas phase into the regional hydrate stability zone (RHSZ) driven by buoyancy. The dynamic effects of hydrate formation on salinities, thermal regimes and hydraulic properties are explicitly modeled. We show sediment lithology and fluid flux primarily control the vertical distribution and concentration of gas hydrate and free gas. We present two mechanisms for vertical gas migration through the RHSZ. In coarse-grained sediments, free gas supplied from depth forms hydrate, depletes water and elevates salinity until pore water is too saline for further hydrate formation. This system allows free gas migration to the seafloor by generating local three-phase equilibrium. In contrast, in fine-grained sediments, hydrate formation leads to rapid permeability reduction and capillary sealing to free gas. This dynamic hydrate seal is critical for allowing gas pressure to build up, thereafter driving gas upward through the RHSZ. Both mechanisms may drive gas venting through hydrate stability zones worldwide. Two-dimensional model of fluid flux suggests that in areas of high gas supply, lateral diffusion of salts is slow enough for gas chimney to rapidly propagate through the RHSZ toward the seafloor.

1. Introduction

Hydrate stability depends on pressure, temperature, the gas concentration in the surrounding pore water, and the activity of water [*Sloan*, 1998]. Liquid (subscript L) and gas (subscript G) coexist below the three-phase equilibrium curve, while liquid and hydrate (subscript H) coexist above it (Fig. 3-1C). We define the regional hydrate stability zone (RHSZ) as the zone where hydrate is stable for seawater salinity (3 wt.%). The temperature at the base of the RHSZ coincided with the temperature of the three-phase equilibrium at hydrostatic pressure and seawater salinity (Fig. 3-1B). Above this depth, temperature is below the three-phase equilibrium value, and hydrate and seawater coexist. Below this depth, free gas and seawater coexist. Free gas should not be present in the RHSZ if excess water is present [*Handa*, 1990]. In this gas hydrate system modeled after southern Hydrate Ridge [*Trehu et al.*, 2004a], the zone of three-phase equilibrium is confined to a single depth (~130 mbsf). This depth is commonly associated with a strong, negative-polarity seismic reflector that mimics the seabed and records the phase boundary between gas hydrate above and free gas below [*Bangs et al.*, 1993; *Holbrook et al.*, 1996].

Current hydrate formation models [*Hyndman and Davis*, 1992; *Rempel and Buffett*, 1997; *Xu and Ruppel*, 1999; *Davie and Buffett*, 2001] describe the accumulation of gas hydrate in the two-phase regions of the three-phase system. These studies suggest that water, methane, and energy fluxes largely control the distribution of free gas and gas hydrate in porous media. These models depends on two-phase equilibrium between hydrate and seawater + dissolved CH_4 [*Hyndman and Davis*, 1992; *Rempel and Buffett*, 1997], and assume that pressure, temperature and salinity variations associated with

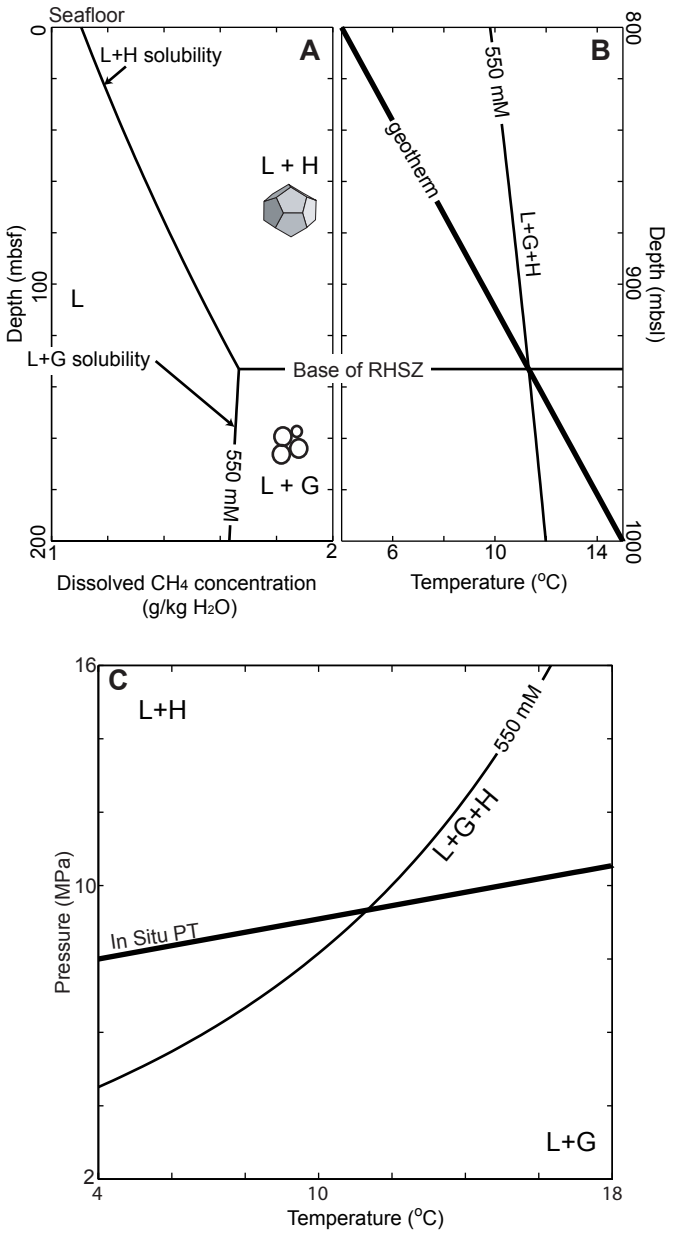

Fig. 3-1: (A) CH_4 solubility, (B) temperature for three-phase equilibrium and (C) hydrate stability P-T phase diagram for seawater salinity (550 mM Cl^-). Fields of hydrate (H), dissolved (L) and free gas (G) are depicted. (A) Hydrate or free gas is present only when the gas concentration exceeds the solubility. The peak in solubility coincides with the base of the RHSZ for seawater salinity (550 mM Cl^-). (B) The intersection of the geotherm with the temperature for three-phase equilibrium defines the base of the RHSZ. mbsf - meters below sea floor; mbsl - meters below sea level.

hydrate formation are negligible compared to total mass and heat transports in the system [*Xu and Ruppel*, 1999]. In addition, these steady-state models do not account for the dynamic effects of hydrate formation on hydraulic, thermal and chemical regimes. Thus they provide little insight into hydrate formation as a transient process.

In this paper, we present a one-dimensional, multi-component, and multi-phase fluid and heat flow model for dynamic and transient hydrate formation in marine environments. Our objective is to understand the dynamics of the gas hydrate reservoir, the mechanisms for free gas migration, and hydrate formation. First, we develop the equations that govern hydrate formation based on the mass and energy balances. We present the criteria for the appearance and disappearance of phases and the corresponding switching of the primary variables. Then, we examine gas hydrate formation in two end-member models. One involves migration of methane-bearing fluid from depth into the hydrate zone, while the other involves free gas migration into the hydrate zone. Finally, the model is extended to two dimensions to show that lateral salt diffusion from the gas chimney is negligible.

Our one-dimensional models suggest that in coarse-grained sediments, hydrate formation at the base of the RHSZ cannot form an efficient capillary barrier to upward gas migration. Thus a large volume of free gas is transported into the RHSZ rapidly to produce a significant change in salinity. In this case, high salinity pore water provides a mechanism to transport free gas through the RHSZ. By comparison, in fine-grained sediments, hydrate formation causes rapid permeability reduction and capillary sealing to free gas. Therefore hydrate formation in such systems is concentrated at the base of the RHSZ until a critically pressured gas column builds up below it. This critical gas pressure

provides a path for vertical gas migration from the free gas zone (FGZ) through the RHSZ. Two-dimensional models show that at high gas flux driven by buoyancy, lateral diffusion of salts is slow enough for gas chimney to rapidly propagate to the seafloor.

2. Mathematical Model

2.1 Assumptions and physical processes

We assume the following. (1) Darcy's Law adequately describes multiphase fluid flow in uniform porous media. (2) Local thermodynamic equilibrium. In marine sediments, the fluid flow rate is small and hydrate formation is rapid as shown by laboratory [*Zatsepina and Buffett*, 2003] and field [*Rehder et al.*, 2002] studies. (3) The model extends from the seafloor to a depth below the RHSZ, and is spatially fixed. (4) There is no sedimentation or tectonic uplift. (5) Gas is supplied only from below the RHSZ instead of through *in situ* production within the RHSZ. (6) CH_4 is the only hydrate-forming gas. (7) Diffusion is only considered in the liquid phase, because diffusion of CH_4 within either hydrate or free gas is negligible. (8) CH_4 is assumed to be the only component in the vapor phase because the amount of water in the vapor phase is small [*Duan et al.*, 1992]. (9) Salt is confined to the liquid phase. (10) Hydrate is a solid phase and only two-phase (gas + water) capillary pressure is considered.

Hydrate formation is modeled as a three-phase, three-component flow system. The three components (κ) are methane, water and salt (superscripts *m*, *w* and *s*). The three phases (β) are liquid, free gas and hydrate (subscripts *l*, *g* and *h*). Each component may be present in different proportion in any of the three phases. The mass fraction of component κ in phase β is denoted by X_β^κ. The system contains a liquid phase consisting

of CH_4, salt and water, a vapor phase consisting of CH_4 only and hydrate composed of CH_4 and water only.

This model includes the following features: (1) the partitioning of the components among the phases is calculated from the assumption of local thermodynamic equilibrium; (2) each phase is allowed to disappear from or appear in any region of the domain during the simulation; (3) fluid flow in both liquid and gas phases occur under pressure, capillary and gravitational forces, according to the multiphase Darcy's law that includes the effect of relative permeability; (4) diffusive transport of CH_4 and salt in the liquid phase are considered; (5) heat transfer occurs due to conduction and multiphase advection, and includes latent heat effects.

2.2 Governing equations

We treat the hydrate system as a continuum of sediment grains, fluids and solid hydrates. We formulate the mass balance for each component (water, methane and salt). Local thermodynamic equilibrium implies that the three phases and the sediment grain in a small volume are at the same temperature, which allows us to formulate the energy balance for the overall porous media. Thus, we obtain a system of partial differential equations, constrained by three mass balances and an energy balance to describe the system (Appendix C).

Each balance equation includes accumulation, flux and sink/source terms. The balance equations are written in integral form for a flow region V_n with a surface area Γ_n, as follow:

$$\frac{d}{dt}\int_{V_n} M^{\kappa} dV = \int_{\Gamma_n} F^{\kappa} \cdot n d\Gamma + \int_{V_n} q^{\kappa} dV \ , \quad (3\text{-}1)$$

where M^κ is the amount of component κ per unit volume, F^κ is the total flux of component κ into V_n, n is the outward unit normal vector, and q^κ is the generation rate of component κ per unit volume. Heat is treated as a "pseudo" component (superscript *e*) [*Falta et al.*, 1992]. For κ= *e*, M^κ is the amount of energy per unit porous media volume. F^κ is the heat flux and q^κ is the rate of heat generation per unit volume.

2.2.1 Accumulation term

Since methane may exist in three possible phases, the methane accumulation term sums over the liquid, vapor and hydrate phases:

$$M^m = \phi \sum_{\beta=l,v,h} S_\beta \rho_\beta X_\beta^m \text{ , (3-2)}$$

where ϕ is the porosity, S_β is the saturation of phase β, ρ_β is the density of phase β, and X_β^k is the mass fraction of component κ in phase β. The water accumulation term sums over the liquid and hydrate phase, because the amount of water in the vapor phase is negligible. The salt accumulation term involves the liquid phase only, because all of the salts are assumed to be dissolved in the liquid.

The heat accumulation term includes contributions from both the solid and the three possible phases:

$$M^e = (1-\phi)\rho_R C_R T + \phi \sum_{\beta=l,v,h} S_\beta \rho_\beta u_\beta \text{ , (3-3)}$$

where ρ_R is the density of the soil grain, C_R is the heat capacity of the soil grain, T is the temperature, and u_β is the specific internal energy of phase β.

2.2.2 Flux term

The mass flux terms of the three components (*m*, *w*, *s*) sum over the three phases (*l*, *v*, *h*). The mass fluxes of each component in the liquid phase include both advection and diffusion as:

$$F_l^\kappa = -\frac{kk_{rl}\rho_l}{\mu_l} X_l^\kappa \left(\nabla P_l - \rho_l g\right) + J_l^\kappa, \quad (3\text{-}4)$$

where k is the intrinsic permeability, k_{rl} is the relative permeability of phase *l*, μ_l is the viscosity of phase *l*, P_l is the pressure of phase *l*, and g is the acceleration due to gravity. And the diffusive flux J_l^κ is:

$$J_l^\kappa = \phi D_l^\kappa \rho_l \nabla X_l^\kappa, \quad (3\text{-}5)$$

where D_l^κ is the molecular diffusion coefficient of component κ in sediment. D_l^κ is

$$D_l^\kappa = \frac{D_{l0}^\kappa}{\theta^2}, \quad (3\text{-}6)$$

where θ is the tortuosity (the resistance to diffusion in porous media) and D_{l0}^κ is the molecular diffusion coefficient in free water. Tortuosity (θ) can be calculated from the sediment porosity (ϕ) using Archie's law [*Torres et al.*, 2004]:

$$\theta^2 = \phi^{-1}. \quad (3\text{-}7)$$

The mass flux of CH_4 in the gas is calculated by considering only advection as:

$$F_g^m = -\frac{kk_{rg}\rho_g}{\mu_g} X_g^m \left(\nabla P_g - \rho_g g\right). \quad (3\text{-}8)$$

The heat flux includes both conduction and multiphase advection as:

$$F^h = -\lambda \nabla T + \sum_\beta h_\beta F_\beta, \quad (3\text{-}9)$$

Where λ is the overall thermal conductivity of the porous media, h_β is the β phase specific enthalpy, and F_β is the total β phase mass flux. λ is calculated as:

$$\lambda = (1-\phi)\lambda_R + \phi(S_h\lambda_h + S_l\lambda_l + S_g\lambda_g), \quad (3\text{-}10)$$

where λ_R, λ_h, λ_l and λ_g are the grain, hydrate, liquid and gas thermal conductivity.

Substituting equations (3-2 to 3-10) into equation (3-1), we obtain three mass balance equations (Appendix C.1-C.3) and one energy balance equation (Appendix C.4). These balance equations, combined with the conditions of thermodynamic equilibrium, provide a complete description of hydrate formation in uniform porous media.

2.3 Thermodynamic Equilibrium for Hydrate Stability

The distribution of hydrate and free gas in the sediment is strongly dependent upon two P-T dependent equilibrium solubility curves (Fig. 3-1A): (1) the liquid-hydrate (*L*+*H*) methane solubility curve (X^m_{L+H}) where gas hydrate is at equilibrium with dissolved gas in water, and free gas is absent; and (2) the liquid-gas (*L*+*G*) methane solubility curve (X^m_{L+G}) where free gas is at equilibrium with dissolved gas in water, and hydrate is absent. *Duan et al.*'s model [1992] is used to predict the *L*+*G* equilibrium. *Henry et al.*'s model [1999] is used to predict the *L*+*H* equilibrium. Comparison of model predictions with the CSMHYD hydrate program shows good agreement.

The *L*+*H* solubility increases downward from the seafloor, while the *L*+*G* solubility slightly increases upward to the seafloor (Fig. 3-1A). At their intersection, three-phase equilibrium is present and CH_4 solubility reaches a maximum value (Fig. 3-1A). The base of the RHSZ is located at the three-phase equilibrium for CH_4 and seawater salinity. When dissolved CH_4 concentration exceeds the solubility, hydrate is stable within the RHSZ while free gas is stable below it.

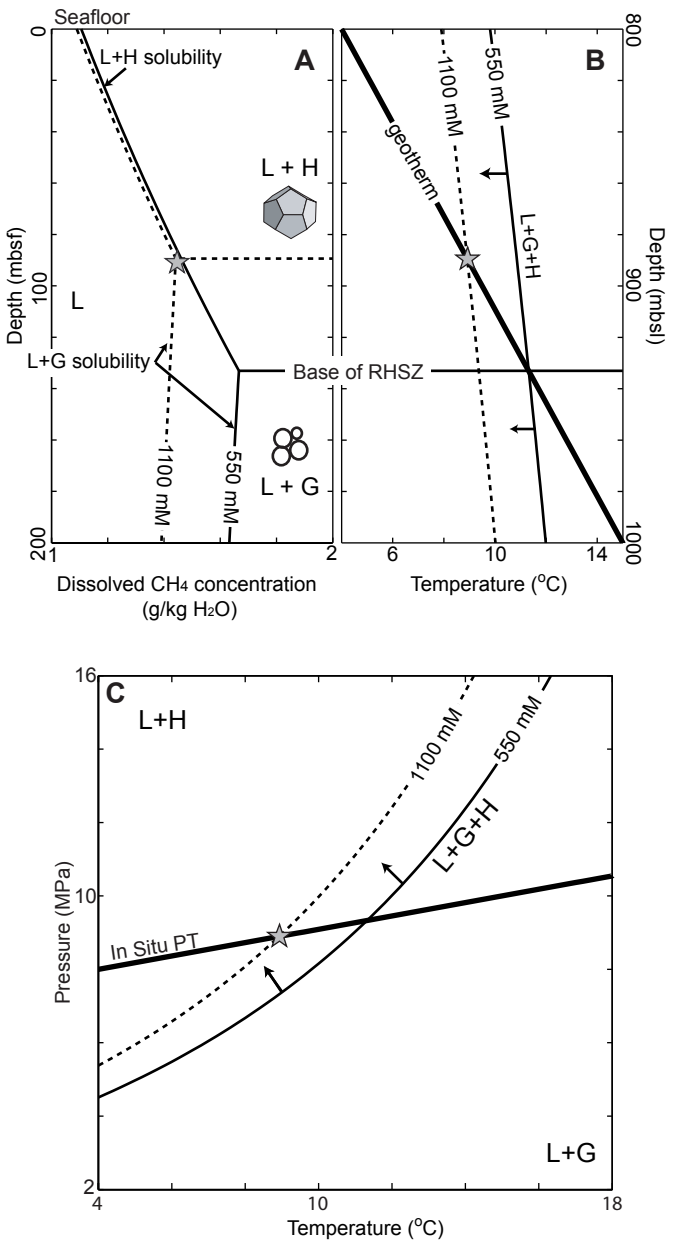

Fig. 3-2: (A) CH_4 solubility, (B) temperature for three-phase equilibrium and (C) hydrate stability P-T phase diagram for salinities of 550 (solid line) and 1100 mM Cl^- (dotted line). Solid arrows indicate the displacement of the phase boundary when salinity increases. mbsf - meters below sea floor; mbsl - meters below sea level.

Doubling pore water salinity from 3 wt.% to 6 wt.% reduces the *L+G* solubility by 15%, while the *L+H* solubility is relatively insensitive to the salinity increase (Fig. 3-2A). As a result, the intersection of the two solubility curves shifts upward from 130 to 90 mbsf. Consequently, the base of the hydrate stability zone shifts from 130 to 90 mbsf (Fig. 3-2B). Elevated pore water salinity decreases hydrate stability conditions (Fig. 3-2C).

2.4 Primary variables and switching during phase transition

We need *n+1* independent variables to describe the thermodynamic state of a *n*-component system [*Clennell et al.*, 1999; *Xu*, 2004]. These *n+1* variables are called the primary variables. For a three-component (methane, water, salt) system, four independent primary variables are needed.

The choice of primary variables for a grid block depends on the phases present in a given volume. For example, under the three-phase condition, the primary variables are chosen to be pressure P, temperature T, liquid saturation S_l, hydrate saturation S_h. This choice of variables completely defines the thermodynamic state of the system. Because all three phases are present, the mass fraction of every component in the phases is determined by local equilibrium consideration. In this case, the salinity of the liquid X_l^s is maintained at that required for three-phase equilibrium, which depends only on the given P and T. The dissolved CH_4 concentration is calculated according to the *L+G* equilibrium at the given P-T-salinity.

Displacement or phase transition processes may cause the appearance or disappearance of three phases. Suppose that the gas phase disappears due to its crystallization as hydrate, perhaps due to a decrease in salinity. Then $S_g=0$; thus S_l and S_h

are dependent ($S_l + S_h = 1$). The system shifts from the three-phase $L+G+H$ to two-phase $L+H$ equilibrium conditions. In this case, the system cannot be fully defined by the primary variables P, T, S_l and S_h. This problem is resolved by primary variable switching during the phase transition. If the primary variables are switched from P, T, S_l and S_h, to P, T, X_l^s and S_h, where X_l^s is the salinity of the liquid, a complete description of the system is once again possible in terms of the primary variables. This technique of primary variables switching is also adopted to describe the phase transition processes in petroleum reservoir simulation [*Farnstrom and Ertekin*, 1987] and subsurface removal of NAPL (Non-Aqueous Phase Liquid) [*Falta et al.*, 1992].

2.5 Substitution criteria

The governing equations, only when combined with local thermodynamic equilibrium, can describe hydrate formation in porous media. For example, if only liquid is initially present, hydrate appears when the dissolved CH_4 concentration (X_l^m) equals the $L+H$ CH_4 solubility (X_{L+H}^m). When the dissolved CH_4 concentration is below the solubility, thermodynamic equilibrium enforces $S_h=0$ and the primary variables are P, T, X_l^m and X_l^s. Once hydrate forms, the dissolved CH_4 concentration is fixed by the solubility ($X_l^m = X_{L+H}^m$), and any additional gas is present in the hydrate phase. Thus the CH_4 concentration (X_l^m) is replaced by the hydrate saturation (S_h) in the set of variables. Similarly, gas appears when the dissolved CH_4 concentration equals the $L+G$ CH_4 solubility (X_{L+G}^m). Upon the appearance of gas, the dissolved CH_4 concentration (X_l^m) is replaced by the gas saturation (S_g) in the set of variables.

Pore water salinity can increase during hydrate formation because salt is excluded from the hydrate structure. If the salinity of the liquid solution (X_l^s) equals the salinity

required for three-phase equilibrium (X^s_{L+G+H}), then gas can appear where only hydrate and seawater coexist previously. The system shifts from two-phase *L+H* to three-phase *L+G+H* equilibria and the primary variables are switched to the three-phase set of variables.

2.6 Secondary variables

In addition to the four primary variables, a complete set of secondary variables is needed for the solution of the four balance equations. These secondary variables include thermodynamic and transport properties such as density, viscosity, permeability and relative permeability. The secondary variables are determined from the primary variables. We calculate the liquid density as a function of temperature and salinity. The gas density strongly depends on pressure and temperature [*Duan et al.*, 1992]. Methane hydrate is assumed to be incompressible and have a constant density (ρ_h=912 kg m^{-3}) [*Sloan*, 1998]. We calculate the liquid and gas viscosities as a function of pressure and temperature [*Class et al.*, 2002]. The calculation of permeability and relative permeability as a function of hydrate saturation is discussed in the next section. Variations in the secondary variables (*e.g.*, permeability *k* and thermal diffusivity λ) can also affect the evolution of the primary variables (*e.g.*, pressure *P* and temperature *T*).

2.7 Changes in porosity, permeability, capillary pressure with hydrate formation

We consider hydrate formation in two different uniform porous media – sand and silt. ϕ_0=0.5 and k_0=~10^{-13} m^2 for sand, while ϕ_0=0.5 and k_0=~10^{-15} m^2 for silt [*Fetter*, 1994]. Assuming the modeled silt and sand have the same pore geometry as the unconsolidated sand in *Bear* [1972], we can scale the capillary pressure curves of the modeled silt and sand from the J-function derived from this unconsolidated sand (Fig. 3-

3B). This curve has a flat plateau, *i.e.*, capillary pressure increases small with decreasing S_w at high S_w. It consists with *Thomeer*'s model [1960] that has a small pore size distribution (*i.e.*, well-sorted sediments). The J-function is [*Amyx*, 1960; *Bear*, 1972]:

$$J(S_w) = \frac{P_{c0}(S_w)}{\sigma_{gw}} \sqrt{\frac{k_0}{\phi_0}}, \quad (3\text{-}11)$$

Where P_{c0} is the capillary pressure in the absence of hydrate and σ_{gw} is the interfacial tension between gas and water (~72 mJ m^{-1}) [*Henry et al.*, 1999]. Using equation (3-11) and the J-function (Fig. 3-3B), we calculate the capillary pressure curve for sands (solid line in Fig. 3-3C) and silts (solid line in Fig. 3-3D) in the absence of hydrate.

The capillary pressure is inversely proportional to the square root of the permeability (equation 3-11). Given the permeability ratio between sand and silt, the capillary pressure of silt is 10 times that of sand. The capillary pressure at S_w=0 is the capillary entry pressure (P_d). The capillary entry pressure must be exceeded before gas enters an initially water-saturated sediment [*Schowalter*, 1979]. We calculate that P_d is ~0.02 MPa for sand and ~0.2 MPa for silt in the absence of hydrate.

Porosity is assumed to be the pore volume fraction filled with fluid phases (liquid and gas). The porosity change due to hydrate formation is:

$$\phi = \phi_0 (1 - S_h), \quad (3\text{-}12)$$

where ϕ_0 is the porosity when hydrate is absent. The permeability is proportional to the hydrate saturation. If the porous medium is approximated as a bundle of capillary tubes and hydrate forms in the centers of each capillary, the change in intrinsic permeability is (Fig. 3-4) [*Kleinberg et al.*, 2003]:

$$k = k_0 \left[1 - S_h^2 + \frac{2(1 - S_h)^2}{\log(S_h)} \right], \quad (3\text{-}13)$$

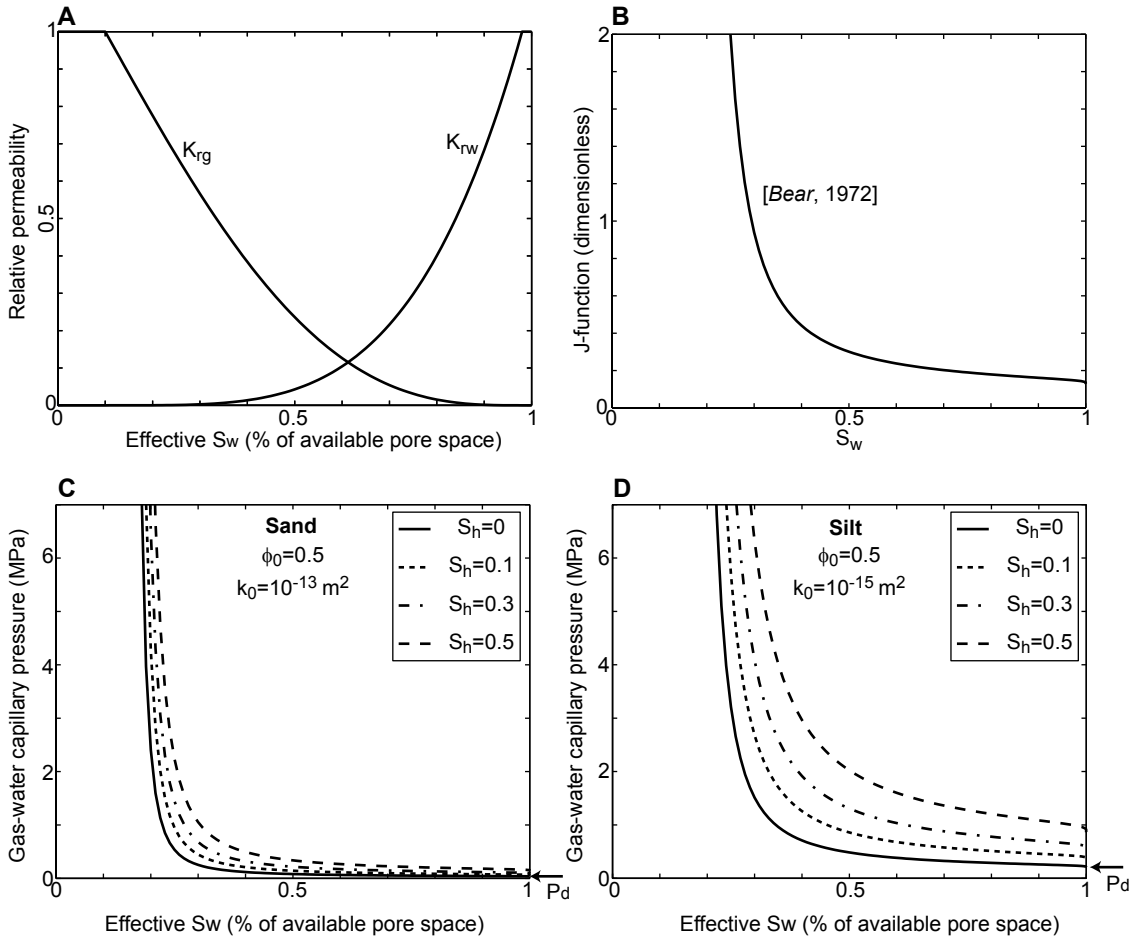

Fig. 3-3: (A) Water and gas relative permeabilities as a function of effective water saturation. (B) Dimensionless J-function for unconsolidated sands [*Bear*, 1972]. Capillary pressure curves of hydrate-bearing sand (C) and silt (D). The solid line represents the capillary pressure curve when hydrate is absent. The dotted, dotted-dashed, dashed lines represent the capillary pressure curve at S_h=0.1, 0.3 and 0.5, respectively. P_d is the capillary entry pressure.

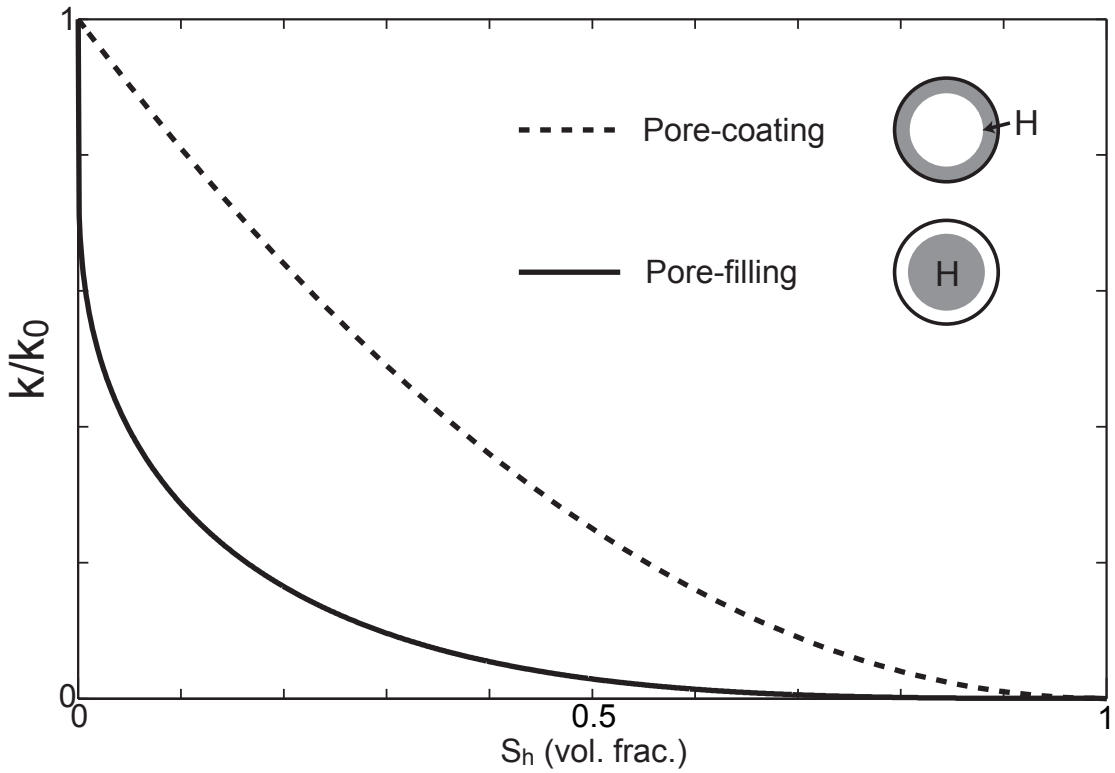

Fig. 3-4: Changes in permeability with hydrate (H) formation. Permeability reduction occurs more rapidly in the pore-filling model (solid line) than in the pore-coating model (dashed line).

where k_0 is the permeability when hydrate is absent. However, if hydrate coats the wall of pores, the change in permeability is (Fig. 3-4) [*Kleinberg et al.*, 2003]:

$$k = k_0 (1 - S_h)^2 . \quad (3\text{-}14)$$

Permeability will decrease more rapidly with hydrate formation for pore-filling model than for pore-coating model (Fig. 3-4). *Clennell et al.* [1999] suggested that hydrate formation is analogous to ice formation in porous media and that hydrate, as a non-wetting phase, preferentially grows in the center of pores in liquid-water-wet sediments. This growth habit has been verified by deep sea NMR (Nuclear Magnetic Resonance) measurements [*Kleinberg et al.*, 2003] and by experiments in glass micromodels [*Tohidi et al.*, 2001]. Thus, we assume hydrate pore-filling in the following simulations.

Hydrate formation is assumed to be analogous to solid precipitation. Hydrate formation decreases the fraction of pore space available to fluid phases. Thus the effective liquid and gas saturations ($S_w^{'}$ and $S_g^{'}$) are:

$$S_w^{'} = \frac{S_w}{S_w + S_g}, \quad (3\text{-}15)$$

$$S_g^{'} = \frac{S_g}{S_w + S_g} . \quad (3\text{-}16)$$

The effective saturations are used in estimating relative permeabilities. The relative permeabilities are calculated according to Corey's model (Fig. 3-3A) [*Bear*, 1972]:

$$k_{rw} = \left(\frac{S_w^{'} - S_{rw}}{1 - S_{rw} - S_{rg}} \right)^4, \quad (3\text{-}17)$$

$$k_{rg} = \left(1 - \frac{S_w^{'} - S_{rw}}{1 - S_{rw} - S_{rg}} \right)^2 \left(1 - \left(\frac{S_w^{'} - S_{rw}}{1 - S_{rw} - S_{rg}} \right)^2 \right), \quad (3\text{-}18)$$

where S_{rw} and S_{rg} are the irreducible or residual water and gas saturation. We use S_{rw}=10% and S_{rg}=2% [*Yousif et al.*, 1991].

Hydrate formation decreases porosity and permeability. Similarly, for each lithology (sand or silt), gas-water capillary pressure in sediments with different hydrate saturation can also be scaled using the J-function [*Moridis et al.*, 2005]. Assuming that the J-functions for hydrate-free and hydrate-bearing sediments are the same, we calculate the capillary pressure in hydrate-bearing sediments from that in hydrate-free sediments:

$$P_c(S_w') = \sqrt{\frac{k_0}{\phi_0} \cdot \frac{\phi}{k}} \cdot P_{c0}(S_w), \quad (3\text{-}19)$$

where P_c is the capillary pressure for hydrate-bearing sediment with k, ϕ and S_w', and P_{c0} for hydrate-free sediment with k_0, ϕ_0 and S_w. Changes in porosity (ϕ) and permeability (k) with hydrate formation are given by equations (3-12) and (3-13). The effective water saturation (S_w') is used to calculate the capillary pressure of hydrate-bearing sediments. Given the same amount of hydrate precipitation, silt (Fig. 3-3D) will experience more increase in capillary pressure than sand (Fig. 3-3C).

3. One-dimensional model of hydrate formation

We model pressure and temperature conditions similar to those at southern Hydrate Ridge, offshore Cascadia [*Trehu et al.*, 2004a]. The initial conditions are as follows (Fig. 3-5; table 1). The seafloor is at 800 mbsl (meters below sea level) and the pressure increases hydrostatically through the sediments (10.4 MPa/km). The bottom water temperature is 4°C and the temperature gradient is linear (55 °C/km). No methane is present and pore water has seawater salinity everywhere (3 wt.%). Under these

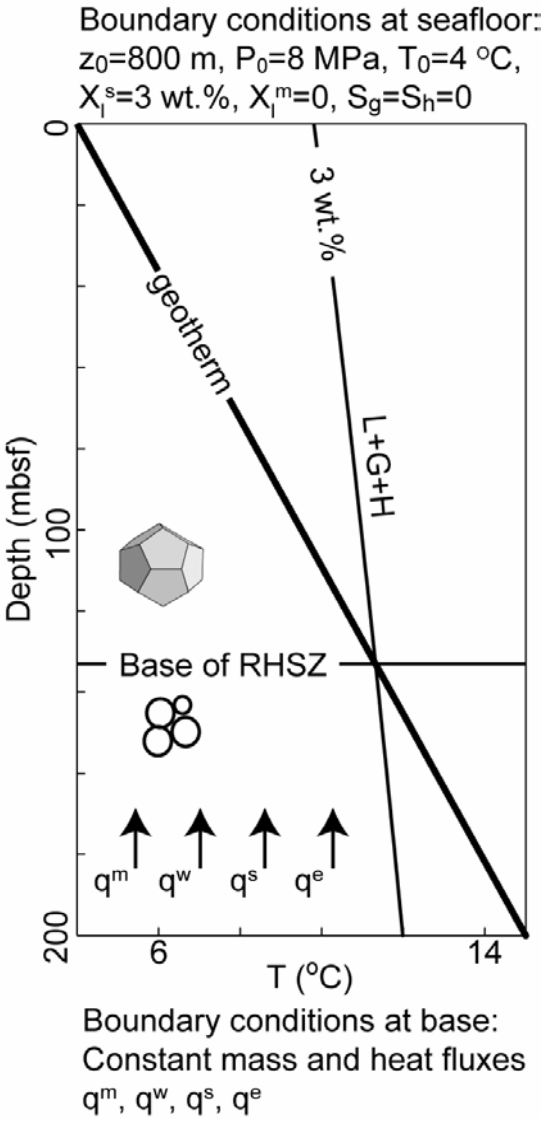

Fig. 3-5: Initial and boundary conditions of one-dimensional model. The intersection of geotherm (heavy solid line) with the temperature for three-phase equilibrium (thin solid line) defines the base of the RHSZ. Methane is supplied into the RHSZ by advection of both methane-rich pore water and free gas.

Table 1 Physical parameters in the one-dimensional simulations

Variable	Physical Meaning	Units or Dependence
g	Gravitational acceleration	9.81 m s^{-1}
T_0	Temperature at seafloor	4.0 °C
dT/dz	Geothermal gradient	55.0 °C km^{-1}
ϕ_0	Porosity when hydrate is free	0.50
k_0	Permeability when hydrate is free	10^{-13} (sand) 10^{-15} m^2 (silt)
z_0	Depth below sea level	800 m
D_{l0}^m	Diffusion coefficient of methane	10^{-9} m^2 s^{-1}
D_{l0}^s	Diffusion coefficient of salt	10^{-9} m^2 s^{-1}
ρ_l	Density of liquid phase	T- & Salinity-dependent
ρ_g	Density of gas phase	P- & T-dependent
ρ_h	Density of methane hydrate	912 kg m^{-3}
μ_l	Dynamic viscosity of liquid	P- & T-dependent
μ_g	Dynamic viscosity of gas	P- & T-dependent

Table 2 Input fluxes in the one-dimensional simulations

	Case 1 (high gas flux in sand)	**Case 2 (high gas flux in silt)**	**Case 3 (low gas flux in silt)**
q^m (methane flux)	0.96 kg m^2 yr^{-1}	0.96 kg m^2 yr^{-1}	0.005 kg m^2 yr^{-1}
q^w (water flux)	0	0	2.5 kg m^2 yr^{-1}
q^s (salt flux)	0	0	0.075 kg m^2 yr^{-1}
q^e (heat flux)	55 mW m^{-2}	55 mW m^{-2}	55 mW m^{-2}
ϕ_0	0.5	0.5	0.5
k_0	10^{-13} m^2	10^{-15} m^2	10^{-15} m^2

conditions, three-phase equilibrium is present at ~130 mbsf. The model domain extends from below the RHSZ to the seafloor (Fig. 3-5).

Boundary conditions imposed during the simulation are as follows (table 1). Constant mass fluxes of CH_4, water and salt are specified at the base of the domain. In addition, there is a constant heat flow at the base of the model and the seafloor temperature is fixed at 4°C.

We run three different scenarios to illustrate the processes of hydrate formation (table 2). A high gas flux is run in sand (*Case 1*). A high gas flux (*Case 2*) and a low gas flux (*Case 3*) are run in silt.

3.1 Case 1: High gas flux + no water flux in sand

The basal CH_4 flux is 0.96 kg m^2 yr^{-1} and there is no basal water or salt fluxes; latent heat released by hydrate formation is neglected. This gas flux is similar to that observed at southern Hydrate Ridge [*Torres et al.*, 2004]. CH_4 is primarily transported as free gas because of the high gas flux. As the free gas moves upward, it displaces the original pore water in which it partly dissolves (Fig. 3-6A and 3-6D, t_1). At t_1, a free gas zone (FGZ) appears below the RHSZ (shaded area) with S_g=2.5%. At this gas saturation, the gas relative permeability is sufficient to allow gas to be transported at the rate that it is supplied (equation 3-18). Within the FGZ, the CH_4 concentration is sustained at its solubility (Fig. 3-6A, t_1). Within the RHSZ, CH_4 concentration is below the solubility (Fig. 3-6A, t_1), there is no hydrate formation (Fig. 3-5D, t_1) and pore water has seawater salinity (Fig. 3-6E, t_1).

When free gas migrates into the RHSZ, a three-phase zone develops in the RHSZ as indicated by the coexistence of hydrate and gas (Fig. 3-6D, t_2). An expanding reaction

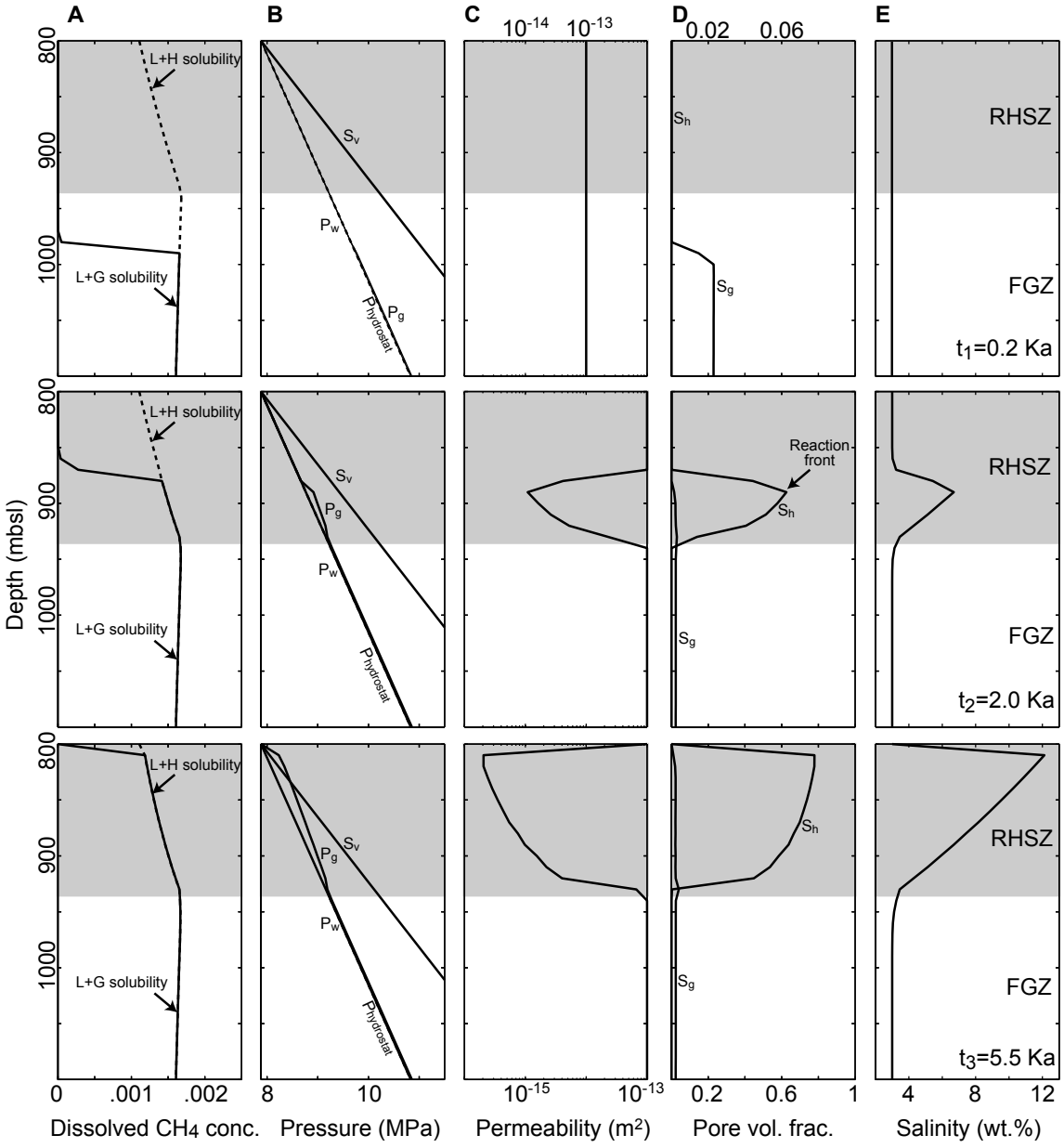

Fig. 3-6: Evolution of (A) dissolved methane concentration, (B) water and gas pressures, (C) intrinsic permeability, (D) water and gas fractions of pore volume, and (E) salinity at three times (0.2, 2.0 and 5.5 Ka) in Case 1. A three-phase zone develops with a front propagating form the base of the RHSZ (shaded area). Behind the front, hydrate formation is water-limited and salinity is buffered at three-phase equilibrium. The reaction front eventually reaches the seafloor. Thereafter free gas can directly flow through the RHSZ to the seafloor. mbsl - meters below sea level.

front separates the three-phase zone below from the two-phase zone above. At t_2, the reaction front is approximately 50 m above the base of the RHSZ. The salinity increases sharply from 3 wt.% at the base of the RHSZ to 6 wt.% at the front. Within the three-phase zone, salinities are sustained at the values required for three-phase equilibrium, while above the three-phase zone, the salinity drops abruptly (Fig. 3-6E, t_2).

The three-phase zone is present across a large vertical range and consequently across large changes in pressure and temperature. This is possible because the salinity increases upward from the base of the RHSZ (Fig. 3-6E, t_2) and the salinity lowers the temperature for three-phase equilibrium. The high salinities result from hydrate formation. As hydrate forms, dissolved salts are excluded from the hydrate structure; at progressively higher levels above the base of the RHSZ, greater concentrations of hydrate must form before the salinity necessary for three-phase equilibrium is achieved (Fig. 3-6E, t_2). The result is an increase in hydrate concentration and salinity upward from the base of the RHSZ to the reaction front. Above the reaction front, hydrate concentration, salinity, and dissolved methane drop rapidly, affected only by diffusion from the underlying reaction front.

The reaction front propagates from the base of the RHSZ toward the seafloor. The propagation rate of the reaction front gradually decelerates with time (Fig. 3-7), because free gas encounters increasingly colder sediments as it rises upward. The amount of hydrate produced for salinity to reach three-phase equilibrium is greater at the shallower depths. The amount of hydrate is largest near the seafloor, where the P-T conditions are brought furthest into the RHSZ.

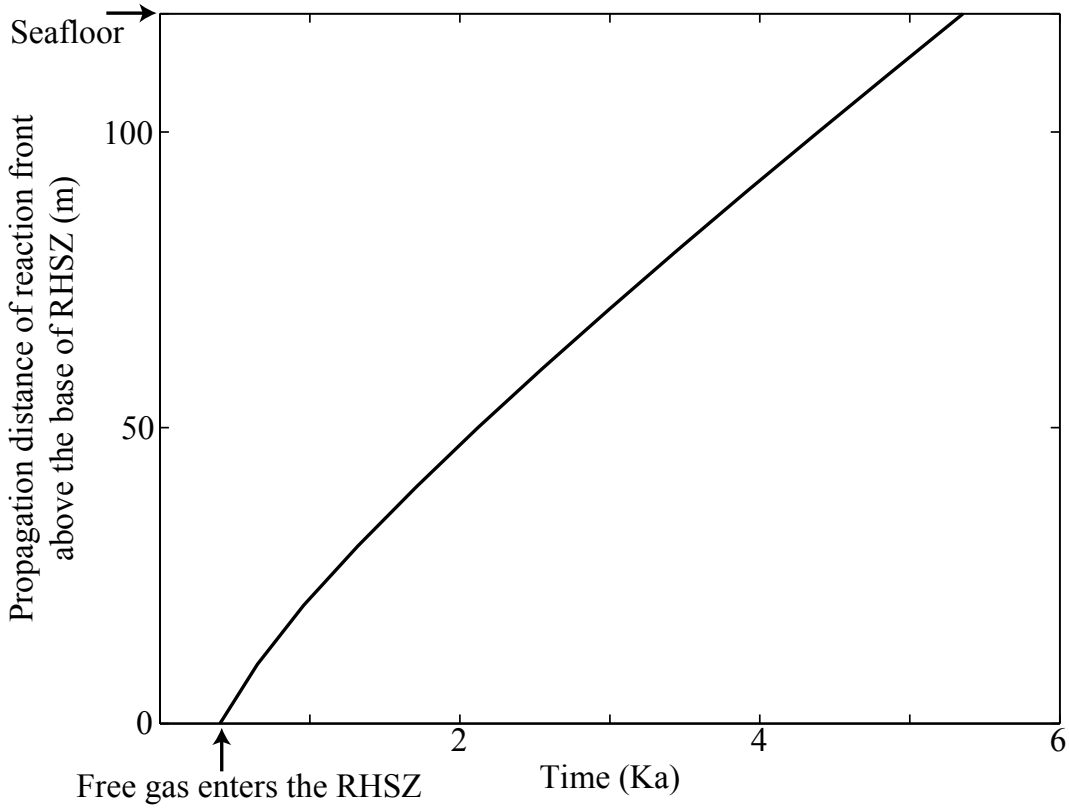

Fig. 3-7: Propagation rate of the reaction front through the RHSZ in Case 1. A large amount of free gas enters the RHSZ at ~0.4 Ka, initiating the front

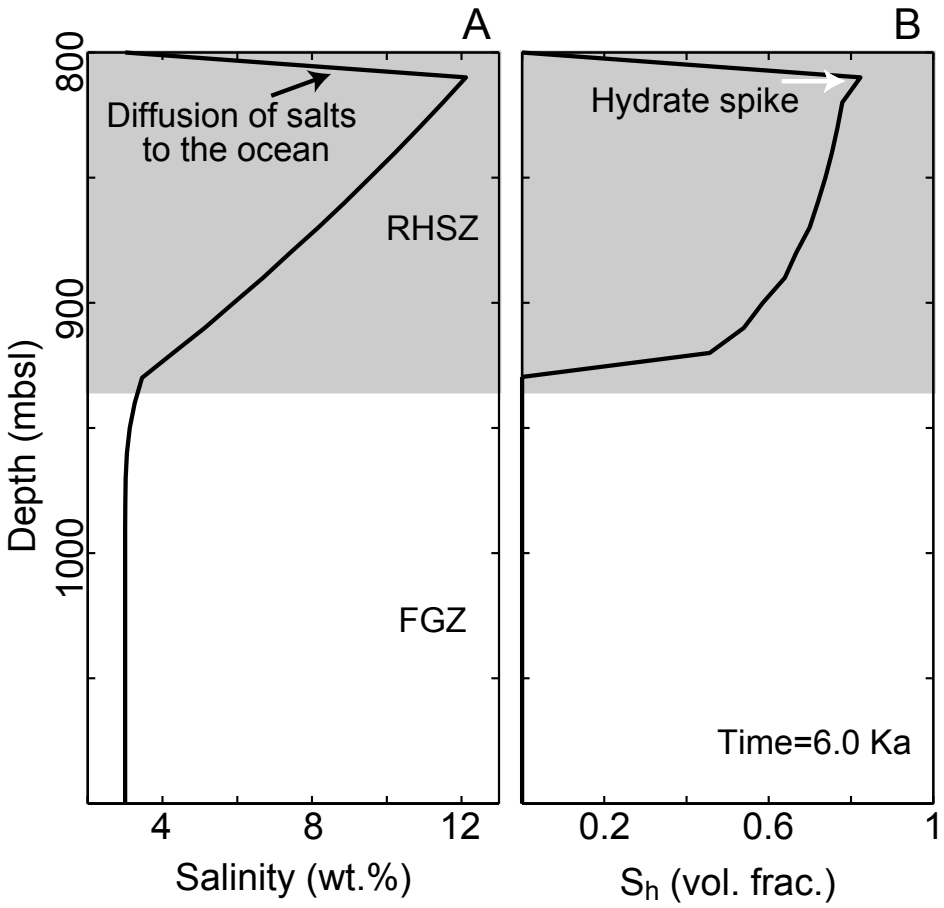

Fig. 3-8: Changes in (A) salinity and (B) hydrate saturation after the three-phase zone extends to the seafloor and a quasi-steady state is reached. (A) The sharp gradient in salinity near the seafloor removes salt out of the three-phase zone. (B) Loss of salts shifts the three-phase equilibrium to allow more hydrate formation below the seafloor.

At t_3, a quasi-steady state is reached when the reaction front breakthroughs the seafloor. At this point, salinities are maintained at those required for three-phase equilibrium throughout the RHSZ (Fig. 3-6E, t_3); the salinity increases sharply from ~3 wt.% at the base of the RHSZ to ~12 wt.% just below the seafloor; the CH_4 concentrations match its solubility throughout the RHSZ (Fig. 3-6A, t_3); three phases coexist throughout the RHSZ; S_h increases upward (Fig. 3-6D, t_3). Both dissolved (Fig. 3-6A, t_3) and free gas CH_4 (Fig. 3-6D, t_3) are discharged at the seafloor.

S_h continues changing after the reaction front reaches the seafloor. Seawater salinity remains at the seafloor in the model, generating a sharp gradient in salinity near the seafloor (Fig. 3-8A). Thus salt is constantly lost from the three-phase zone into the ocean. Loss of salts to the ocean shifts the thermodynamic conditions, allows further hydrate formation, and causes a spike in S_h immediately below the seafloor (Fig. 3-8B). Salt is continually diffused out of the hydrate layer and into the overlying ocean.

3.2 Case 2: High gas flux + no water flux in silt

Case 2 differs from Case 1 only in that Case 2 is performed in silt. As in Case 1, free gas is hydrated once it enters the hydrate stability zone (Fig. 3-9D, t_1). However, in this case, hydrate formation in the already low-permeability sediments (Fig. 3-9C, t_1) results in a larger increase in capillary entry pressure, considering that the capillary pressure is inversely proportional to the square root of the permeability (equation 3-11). Thus the base of the RHSZ acts as a cap, preventing upward migration of CH_4 gas and causing it to accumulate below the base of the RHSZ (Fig. 3-9D, t_1). During gas filling, CH_4-rich pore water is displaced from the trap to the seafloor. Dissolved CH_4 is also transported upward from the trap by diffusion. But dissolved CH_4 concentration is still

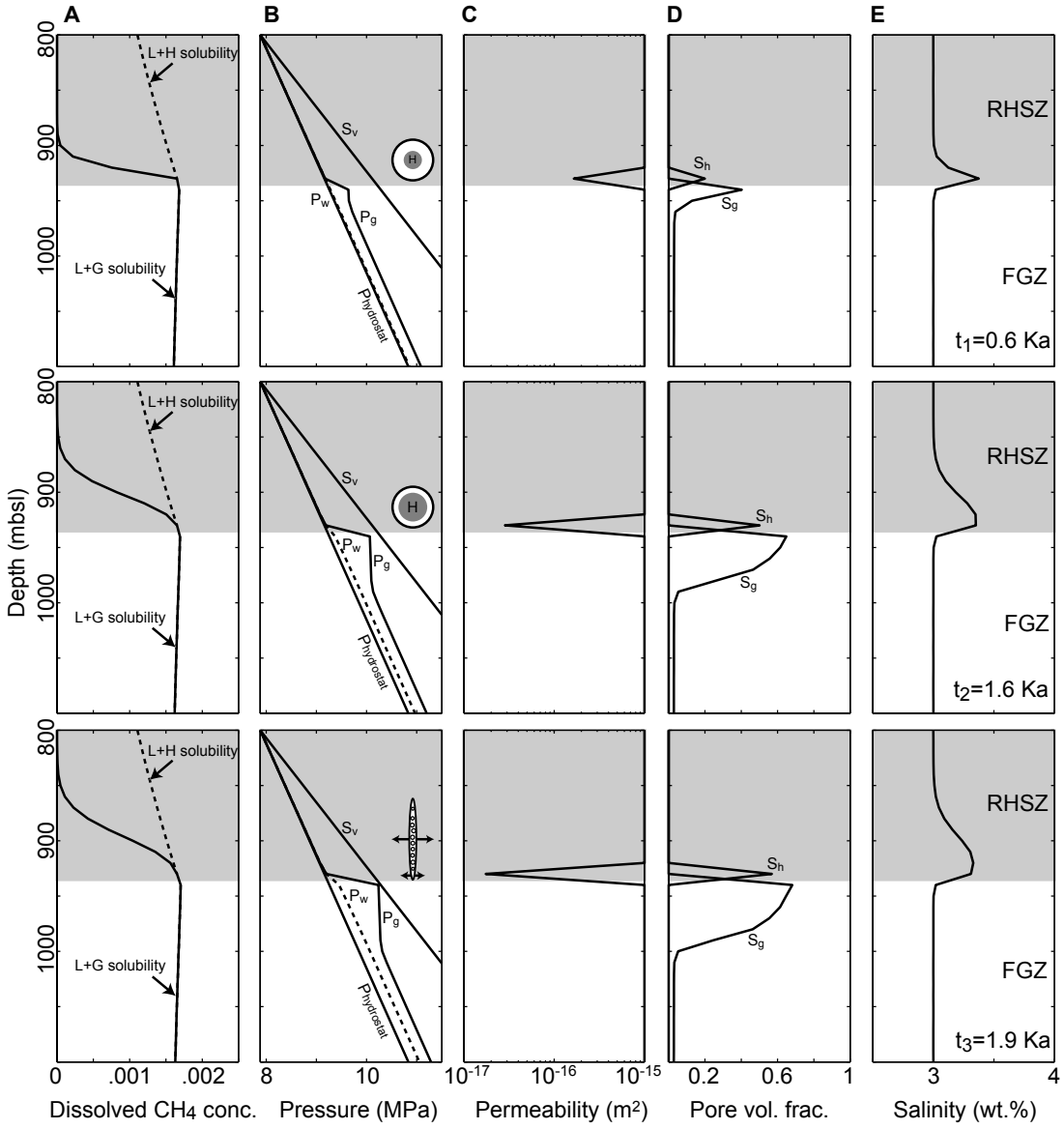

Fig. 3-9: Evolution of (A) dissolved methane concentration, (B) water and gas pressures, (C) intrinsic permeability, (D) water and gas fractions of pore volume, and (E) salinity at three times (0.4, 1.6 and 1.9 Ka) in Case 2. Hydrates precipitated at the base of the RHSZ form a capillary barrier to upward gas migration. Free gas progressively accumulates below the hydrate layer, building up a gas column. With constant gas supply, the gas column height increases until the gas pressure (P_g) at its top impinges on the overburden stress (S_v). Then high gas pressure forces the gas to migrate upward through the RHSZ.

below its solubility within the RHSZ (Fig. 3-9A, t_1). Thus there is no hydrate formation (Fig. 9D, t_1) and no salinity buildup (Fig. 3-9E, t_1). At this point, hydrate formation is restricted to the base of the RHSZ where water and gas (*i.e.*, reactants) are abundant, and most of the supplied CH_4 is trapped as free gas below the hydrate zone.

Only a small gas column builds beneath the hydrate layer at t_1. When the buoyancy force at the top of gas column exceeds the original capillary entry pressure at t_1, gas flows into the seal, forming more hydrate at the base of the RHSZ. Capillary entry pressure increases further. For more gas to enter the RHSZ, the gas pressure must increase further and therefore a larger gas column must build up below gas hydrate. Ultimately, the buoyancy force at the top of gas column reaches the new capillary entry pressure (Fig. 3-9D, t_2). Thus, breakthrough and resulting increase in capillary entry pressure lead to an additional increase of the column height. Meanwhile, the fraction of gas-filled pore volume increases by displacing more water and the gas-water contact moves downward (Fig. 3-9D, t_2). In this case, hydrate forms only at the base of the RHSZ via a series of small, discontinuous gas migration pulses.

The difference between the gas and water pressures is the gas-water capillary pressure, which is proportional to S_g. Through the gas column, gas pressure follows its static pressure gradient (~0.7 MPa/km), while water phase is overpressured (~0.2 MPa above hydrostatic conditions) (Fig. 3-9B, t_2). This is because (1) gas is displacing water upward and (2) water permeability is small in the gas column where S_w is near the residual value (equation 3-17). The capillary pressure ($P_{cgw}=P_g-P_w$) increases with the elevation above the gas-water contact (Fig. 3-9B, t_2). Thus S_g increases upward through

the gas column (Fig. 3-9D, t_2), as the upward-increasing capillary pressures force gas into successively smaller pores.

The gas column height continues to increase with further hydrate formation at the base of the RHSZ until gas pressure at the top of the gas column (P_g) reaches the overburden stress (S_v) (Fig. 3-9B, t_3). Then the trapped gas column can not build up further, though capillary entry pressure at the base of the RHSZ continues increasing with hydrate formation. The vertical gas effective stress ($=S_v$-P_g) decreases to zero and hydraulic fracturing occurs to allow for upward gas migration. However, we do not account for further migration of gas in fractured network within the RHSZ. A more complicated model will be developed in the future to address this issue. The simulation ceases once the gas pressure reaches the overburden stress at the BSR depth.

The gas column height necessary for its pressure to reach the overburden stress is the critical height. There is a critical gas column height of ~120 m immediately beneath the RHSZ (Fig. 3-9D, t_3), when both water overpressure and gas-water capillary pressure elevate the gas pressure (P_g) to the lithostatic stress (S_v). Note that finite capillary entry pressure (~0.2 MPa) and water overpressure of the FGZ (~0.2 MPa) reduces the critical gas column height (Fig. 3-9B, t_3), relative to zero capillary entry pressure and hydrostatic conditions. At this point, the gas pressure at the top of the gas column is enough to dilate fractures, no seal capacity remains to support an additional gas column, and gas migrating from depth must escape the FGZ to keep gas pressure from exceeding the overburden stress. Thus the lithostatic gas pressures allow gas to escape the FGZ by opening fractures and to form hydrate above the base of the RHSZ.

3.3 Case 3: Low gas flux + water flux in silt

The model is carried out in silt. The fluxes of CH_4, water and salt are 0.005, 2.50 and 0.75 kg m^{-2} yr^{-1} respectively, and latent heat released by hydrate formation is neglected. Given the specified CH_4 flux and CH_4 solubility at the base of the model domain, we estimate that not all of the supplied CH_4 is carried by the specified water flux. The maximum amount of CH_4 carried by water is limited by its low solubility (~10^{-3}) (Fig. 3-10A, t_1). Thus excess CH_4 occurs as free gas at the base of the domain.

At t_1, CH_4 is transported into the RHSZ only by aqueous diffusion and advection (Fig. 3-10A, t_1). Hydrate forms only in the center of the RHSZ (Fig. 3-10D, t_1), where the CH_4 concentration exceeds the solubility. Hydrate formation does not extend to the base of the RHSZ, where CH_4 solubility is higher. A FGZ is present ~50 m below the RHSZ (Fig. 3-10D, t_1) and CH_4 concentration is sustained at its solubility in the FGZ (Fig. 3-10A, t_1). The gas displacement front lags behind, since free gas cannot move upward until the residual gas saturation (S_{rg}=2%) is exceeded (equation 3-18). At this point, the deepest occurrence of hydrate does not coincide with conditions for three-phase equilibrium.

The top of the free gas zone is separated from the base of the hydrate zone by a zone containing liquid only (Fig. 3-10D, t_1), where CH_4 concentration is below its local solubility. We interpret this gap as a transient feature, because this zone shrinks as free gas progressively moves upward and saturates pore water below the RHSZ. Eventually, hydrate and free gas coexist at the base of the RHSZ (Fig. 3-10D, t_2). At this point, the P-T at the base of the RHSZ coincides with conditions for three-phase equilibrium.

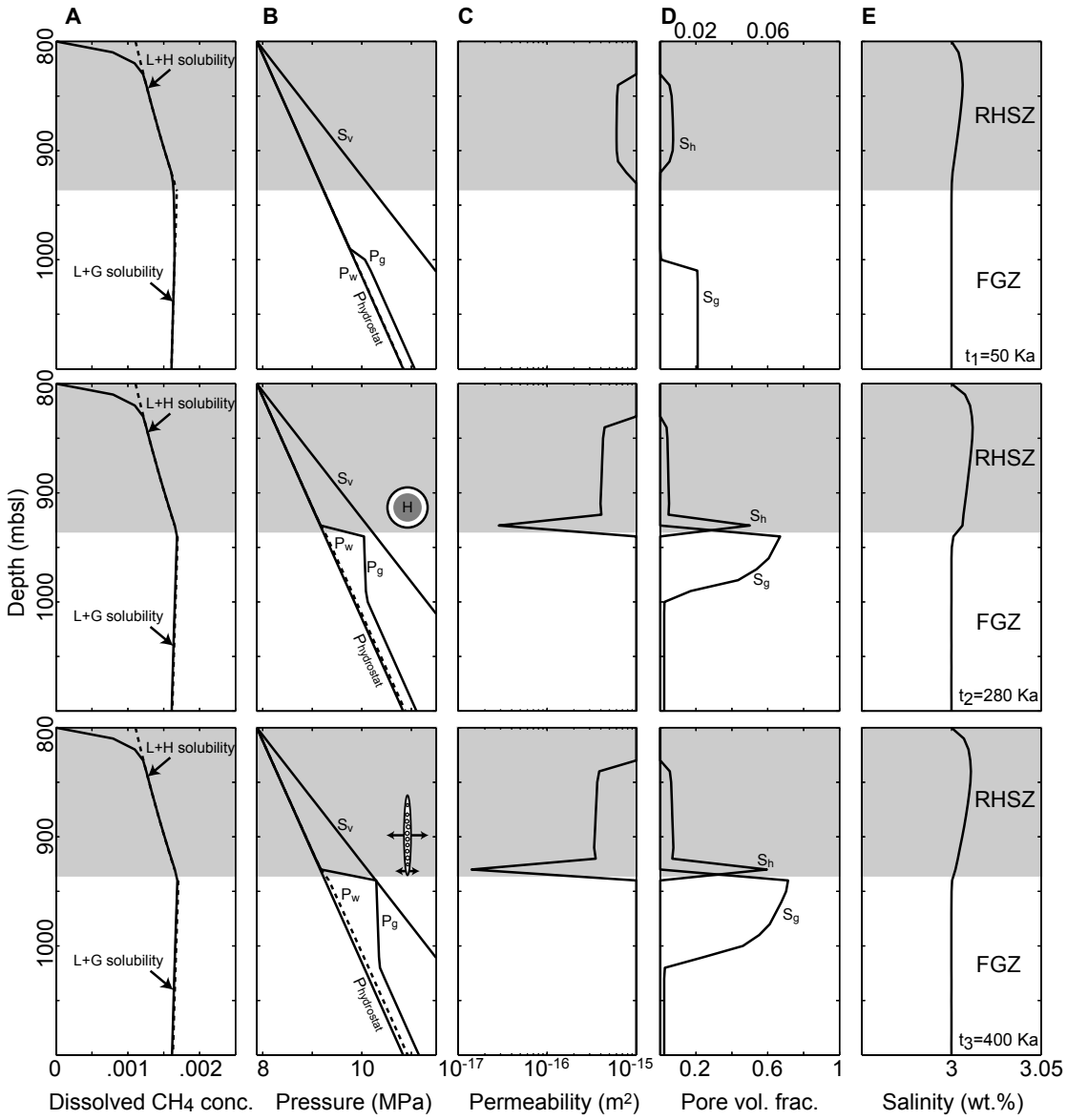

Fig. 3-10: Evolution of (A) dissolved methane concentration, (B) water and gas pressures, (C) intrinsic permeability, (D) water and gas fractions of pore volume, and (E) salinity at three times (50, 280 and 400 Ka) in Case 3. Initially, there is a gap between the top of free gas and the base of gas hydrate. Then both dissolved and free gas CH_4 are transported into the RHSZ, forming a peak in S_h at the base of the RHSZ. The layer of concentrated hydrate permits gas pressure to build up below it. The critical gas pressure eventually drives the gas upward through the RHSZ to seafloor. mbsl - meters below sea level.

At t_2, free gas migrates into the RHSZ and rapidly forms hydrate at the base of the RHSZ. The CH_4 concentration is everywhere maintained at the solubility except near the seafloor (Fig. 3-10A, t_2), where its concentration is set to zero. CH_4 is transported into the RHSZ by a mixture of saturated water (Fig. 3-10A, t_2) plus free gas (Fig. 3-10D, t_2). A gradual increase in S_h within the RHSZ occurs above a sharp increase in S_h at the base of the RHSZ (Fig. 3-10D, t_2). Dissolved CH_4 is continuously transported upward into the RHSZ by aqueous diffusion and advection. However, the amount of CH_4 carried by water is limited by low methane solubility below the RHSZ. Thus S_h slowly increases within the RHSZ, where the gradient in CH_4 solubility is small (Fig. 3-10A, t_2). On the other hand, CH_4 transported in the gas phase freezes as hydrate once it enters the RHSZ, producing a sharp spike in S_h at the base of the RHSZ.

Similar to Case 2, hydrate forms at the base of the RHSZ via a series of gas migration pulses during gas filling. The formation of concentrated hydrate at the base of the RHSZ impedes upward migration of gas due to capillary pressure (Fig. 3-10B, t_2). CH_4 gas that continues to migrate from deeper sediments is trapped below the RHSZ. But the capillary seal does not block water flow. Dissolved CH_4 can be transported into the RHSZ from the trap by aqueous flow to form more hydrate. Thus in this case, though free gas is trapped below the RHSZ, hydrate can accumulate further in the RHSZ (Fig. 3-10D, t_2).

There is no significant salinity buildup in this case (Fig. 3-10E, t_2). The resulting salinity is not high enough for free gas to stabilize in the RHSZ, because capillary pressure at the base of RHSZ inhibits a large volume of free gas from entering the RHSZ.

Moreover, the excluded salts are efficiently removed out of hydrate formation zone by upward water flow. Thus, S_g vanishes at the base of the RHSZ (Fig. 3-10D, t_2).

Similar to *Case 2*, as more hydrate precipitates in pores and the seal capacity increases, gas continues to accumulate until the height of the interconnected gas column exerts sufficient buoyant force at its top to equal the overburden stress in the overlying sediment (Fig. 3-10B, t_3). At this point, large amounts of free gas migrate upward into the overlying sediments within the RHSZ by opening fractures. The model ceases when the gas pressure reaches the overburden stress.

4. Two-dimensional model of gas chimney

A two-dimensional model is adopted to study the formation of gas chimney and the effect of lateral salt diffusion on its formation (Fig. 3-11). Gas chimney is modeled in two dimensions assuming symmetry about a vertical zone with basal gas supply. The left edge is the centerline of gas chimney. The left and right edges are no-flow boundaries. The seafloor P and T are fixed at the initial values. A basal gas flux of 0.96 kg m^2 yr^{-1} is imposed on the inner three sediment columns, while there is no basal gas flux in the surrounding sediments. The specified gas flux is similar to that observed at southern Hydrate Ridge [*Torres et al.*, 2004]. We consider one scenario where the capillary pressure is neglected and one scenario where it is considered. Both simulations are run in sand.

4.1 Gas chimney model without capillary pressure

The changes in capillary pressure with hydrate formation are neglected in this case. A gas chimney forms with an advancing reaction front that separates the three-phase zone behind from the surrounding sediments. The pore water salinity in gas

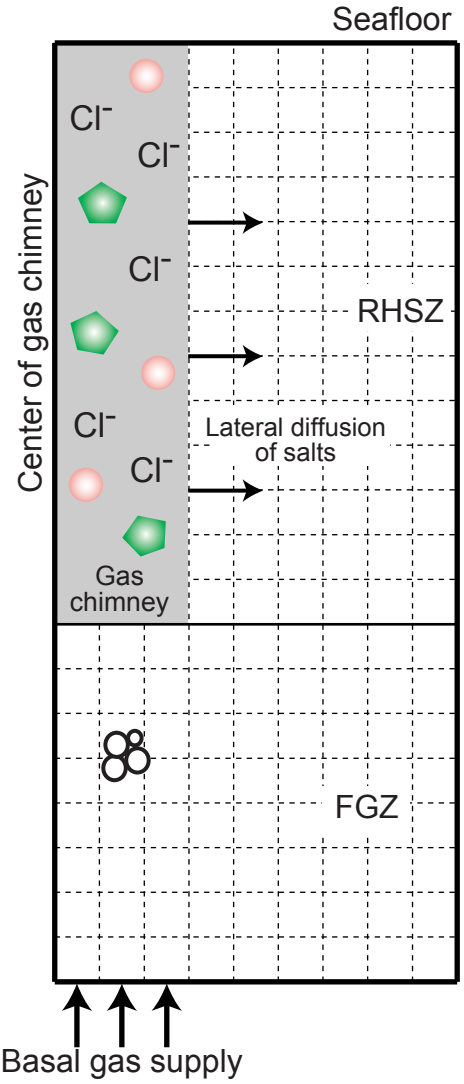

Fig. 3-11: Initial and boundary conditions of two-dimensional gas chimney model. Modeling of fluid flux and hydrate formation is performed assuming symmetry about a vertical gas flux zone. Free gas transports through the RHSZ by elevating pore water salinity. Lateral diffusion of salts from gas chimney affects its propagation toward the seafloor.

chimney is sustained at the value required for three-phase equilibrium (Fig. 3-12A), while the surrounding sediments have seawater salinity. Thus, as the reaction front advances, the sharp lateral changes in salinity across the wall diffuse salts out of the chimney. Meanwhile, hydrate formation at the reaction front initiates the flow of dissolved salts away from hydrate (Fig. 3-12C). As a result, a region of positive salinity anomaly (*i.e.*, salinity halo) occurs in the vicinity of gas chimney (Fig. 3-12A). Loss of salts shifts the established three-phase equilibrium to allow for more hydrate formation. Thus, hydrates need form additionally at the wall of the chimney to replace the salinity lost by lateral diffusion (Fig. 3-12B). By contrast, inside the chimney, further hydrate formation is inhibited by hyper-saline pore water.

The water and gas flow do not occur in the same direction. Water flow is solely controlled by the pressure gradients, while gas flow is controlled by the combined effects of water flow and buoyancy [*England et al.*, 1987]. Water flows both upward and laterally away from the propagating reaction front (Fig. 3-12C), where hydrate formation changes fluid volume. In this case, buoyancy that is always directed upward dominates over water potential gradients, because of the large contrast in density between free gas and water (ρ_w-ρ_g=~930 kg m^{-3}). Thus the resulting gas flow is predominantly vertical (Fig. 3-12D).

The reaction front reaches the seafloor after only ~8 Ka. A hydrate-lined gas chimney extends vertically through the RHSZ in sediment columns where gas is supplied. The salinity within it increases sharply toward the seafloor (Fig. 3-13A). Sustaining three-phase equilibrium within the chimney requires a continuous hydrate formation at its wall to overcome the loss of salts. The salinity halo extends only ~30 m from the

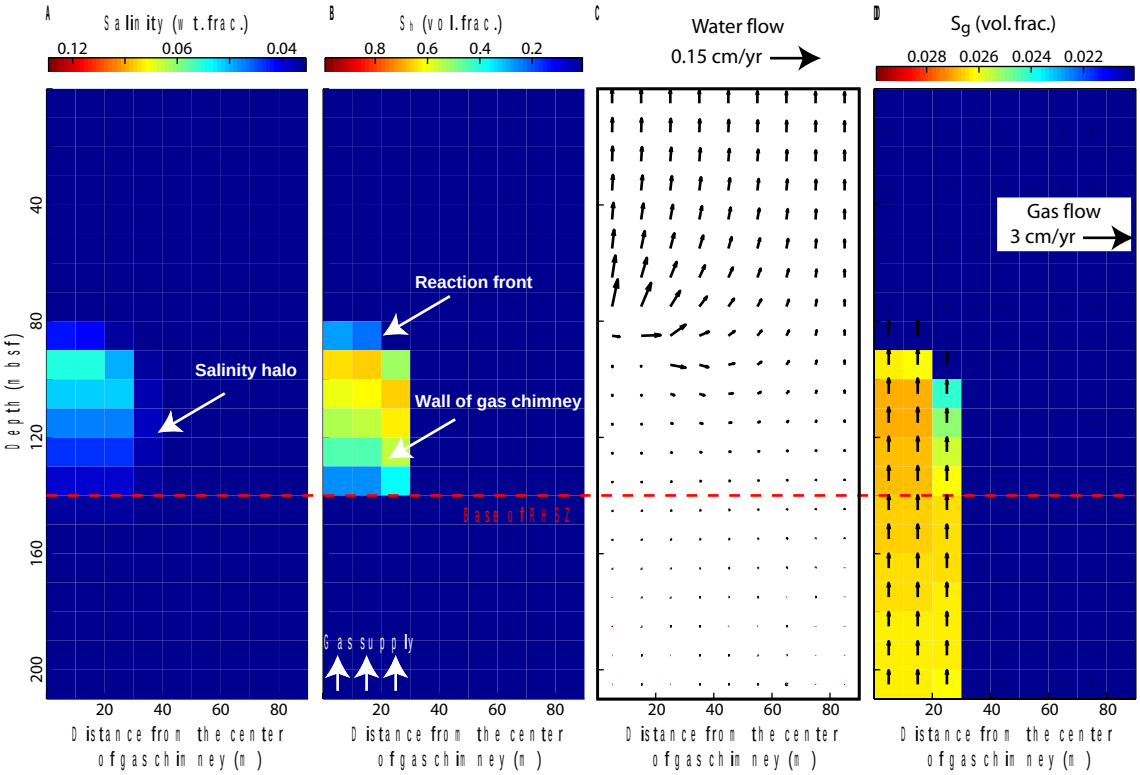

Fig. 3-12: (A) Salinity, (B) hydrate saturation, (C) water flow and (D) gas flow associated with an evolving chimney at 1.0 Ka. Capillary pressure is neglected and water depth is 800 m. A reaction front propagates upward, behind which three phases coexist. Water flows away from the reaction front, while gas flows only vertically. mbsf – meters below sea floor.

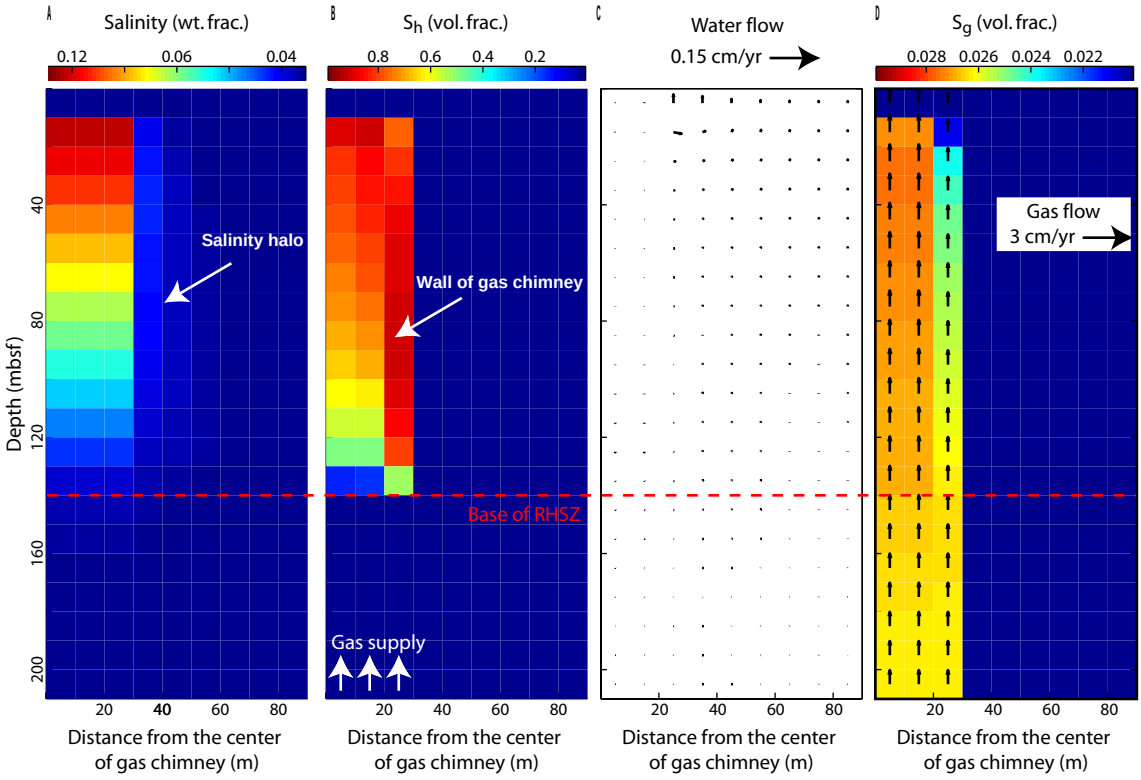

Fig. 3-13: (A) Salinity, (B) hydrate saturation, (C) water flow and (D) gas flow with an evolving chimney at 8.0 Ka. Capillary pressure is neglected and water depth is 800 m. A narrow, near-vertical, hydrate-lined chimney extends completely to the seafloor, forming a conduit for gas migrating upward. Water flow in the system is small. Gas flows vertically through the RHSZ but its rate decreases toward the seafloor.

chimney wall (Fig. 3-13A), where the formed hydrate decreases porosity and increases tortuosity of sediments (equation 3-7), inhibiting the efficient removal of salt from gas chimney.

Hydrate formation is limited to the area of gas flux (Fig. 3-13B), because free gas migrates only vertically in this case. Though the dissolved methane is transported out of chimney by aqueous advection and diffusion, its concentration does not reach the solubility to form hydrate. Thus a vertical, hydrate-lined gas chimney penetrates the RHSZ (Fig. 3-13B). Gas steadily transports through the RHSZ inside the chimney, while due to salt loss, gas flow decreases upward along the wall of the chimney (Fig. 3-13D).

4.2 Gas chimney model with capillary pressure

The changes in capillary pressure with hydrate formation are considered. A gas chimney expands both upwards and laterally with an advancing reaction front (Fig. 3-14B). The salinity for three-phase equilibrium is maintained within the chimney (Fig. 3-14A). The main difference is that the driving force for free gas migration is no longer only vertical. In this case, gas flow is determined by water flow, buoyancy and capillary pressure. Water flows away from the advancing reaction front (Fig. 3-14C). Free gas migration is aided by the buoyancy force but inhibited by the capillary effect. Hydrate formation increases the capillary pressure in gas chimney, reducing vertical flow of gas. The increased capillary pressure in gas chimney forces gas to migrate horizontally to hydrate-free regions. Thus gas flow diverts laterally (Fig. 3-14D), causing the lateral growth of gas chimney and hydrate layer.

Free gas breakthroughs the seafloor in the inner sediment columns after only ~8 Ka (Fig. 3-15D). At this point, free gas is directly vented to the ocean, gas flow diverts

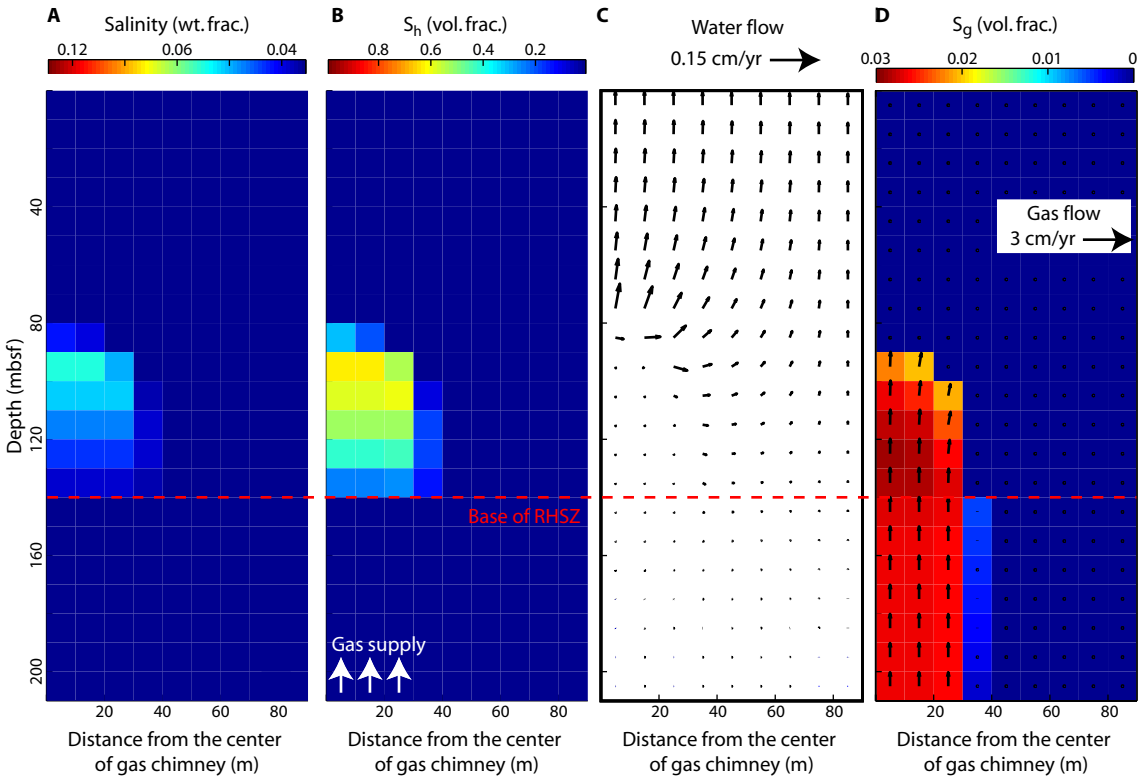

Fig. 3-14: (A) Salinity, (B) hydrate saturation, (C) water flow and (D) gas flow associated with an evolving gas chimney at 1.0 Ka. Capillary pressure is considered and water depth is 800 m. Hydrate formation is not only limited to the areas of gas supply. Water flows away from the front. Gas flow is diverted laterally at the front. mbsf – meters below sea floor.

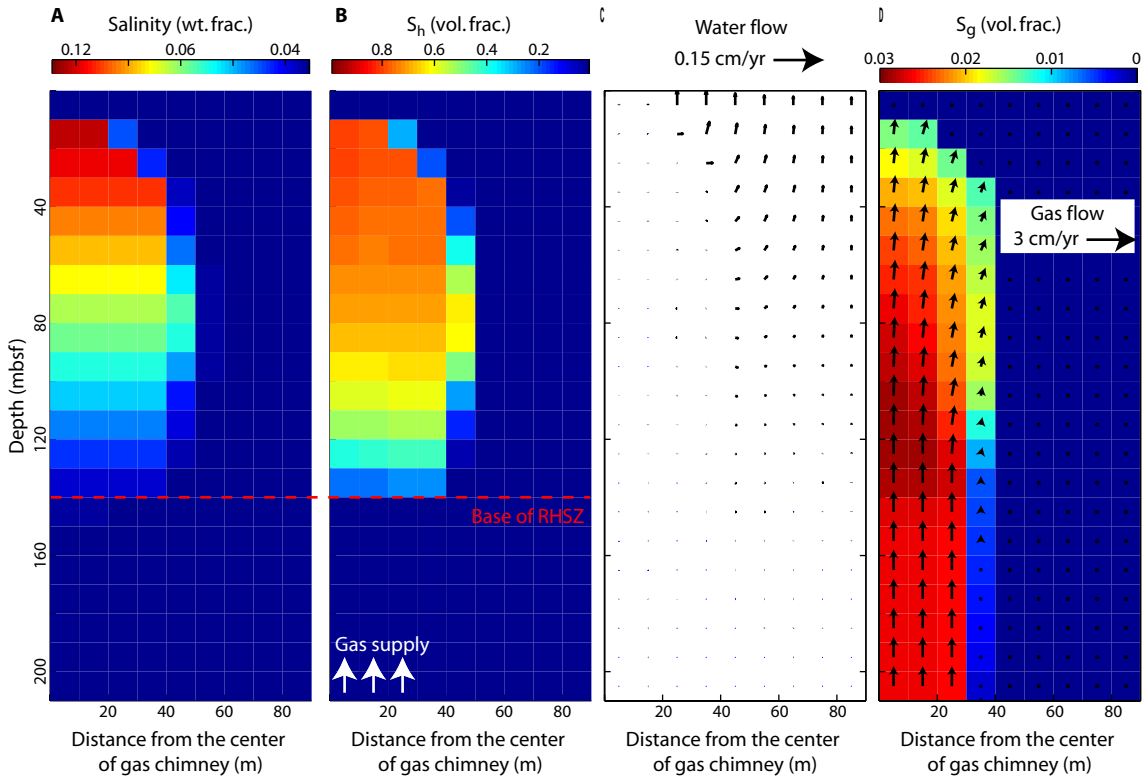

Fig. 3-15: (A) Salinity, (B) hydrate saturation, (C) water flow and (D) gas flow associated with an evolving gas chimney at 8.0 Ka. Capillary pressure is considered and water depth is 800 m. The chimney extends both vertically and laterally. Gas flow diverts laterally and its rate greatly decreases upward. The displacement of gas flow leads to the lateral growth of chimney.

laterally, and gas chimney is wider at the top than at the base (Fig. 3-15B). Gas chimney, hydrate formation and gas flow are not restricted to the area of basal gas supply, because capillary pressure difference between inside and outside the chimney can cause the lateral displacement of gas flow (Fig. 3-15D), enlarging the area of gas chimney.

5. Discussion

5.1 Comparison with other numerical models

Through flow-transport-reaction coupling, we account for transient hydraulic, thermal and chemical signatures that develop in marine hydrates during its formation. The model differs from the previous models in several aspects. First, the model tracks the local changes in pressure, temperature and salinity that accompany hydrate formation, rather than simply assumes the regional geothermal, hydrostatic and fixed salinity conditions. Second, it accounts for the influence of P-T-salinity variations on CH_4 solubility and hydrate stability. Third, free gas is permitted in the RHSZ and hydrate may occur below the RHSZ, depending on the local thermodynamic conditions. Three phases may coexist over a vertical range instead of only at a single depth. Fourth, free methane gas is allowed to move upward rather than remains trapped in sediments. The model focuses the active role of free gas in fluid flow, mass transport and hydrate formation. Last, sediment properties (*e.g.*, porosity, permeability and capillary pressure) are permitted to change with hydrate formation. The resulting permeability reduction and capillary sealing may trap a critical gas column below the hydrate zone.

5.2 A critically pressured gas column below southern Hydrate Ridge

Trehu et al. [2004a] showed that a critical gas column thickness exists below southern Hydrate Ridge, offshore Oregon. This critical gas column exists within a

dipping, permeable layer - Horizon A. Gas saturation estimated from density log and gas column height estimated from seismic data are sufficient to support a critically pressured gas column [*Trehu et al.*, 2004a]. The BSR is disrupted when the BSR crosses the RHSZ. A gas chimney is present above the disrupted BSR. We speculate that at the early stage, gas and water concurrently migrated updip through Horizon A. Hydrate formed once free gas entered the RHSZ. However, the excluded salts were efficiently removed from gas hydrate by the concomitant water flow, preventing the buildup of salt. Thus free gas accumulated in Horizon A below the BSR rather than continued to move updip by generating three-phase equilibrium. As hydrate precipitated in pores and the seal capacity increased, the gas column height continuously increased until the gas pressure at its top reached the overburden stress to open fractures. At this point, the critically pressured gas column forced gas upward through the RHSZ, forming the gas chimney.

ODP (Ocean Drilling Program) Site 1250 at the crest of southern Hydrate Ridge does not show significant salinity anomaly, though it is only ~200 m from the postulated salty gas chimney [*Liu and Flemings*, 2005]. Our two-dimensional model shows that at the specified gas flux of ~0.96 kg m^{-2} yr^{-1}, the gas chimney may rapidly extend toward the seafloor after only ~8 Ka. Since chemical diffusion is small relative to gas flux, the salinity halo is only significant adjacent to gas chimney (~30 m). Thus Site 1250 has no enrichment of salinity that is likely transported laterally from gas chimney. Complete diffusion of excluded salts out of the gas chimney will take significantly long time.

5.3 Influence of hydrate growth habit

The permeability of hydrate-bearing sediments depends crucially on where hydrate forms in pores [*Kleinberg et al.*, 2003]. In the one-dimensional simulations, we

assume that hydrate forms in the centers of pores. This growth habit causes rapid permeability reduction and capillary sealing to free gas. But there is a small effect on fluid flow if hydrate coats the wall of pores [*Kleinberg et al.*, 2003]. If pore-coating model is instead assumed in these simulations, permeability reduction is much less significant (Fig. 3-4). Given that the capillary pressure is inversely proportional to the permeability (equation 3-11), hydrate-bearing sediments at the base of the RHSZ would not form an efficient capillary barrier to upward gas migration. The gas pressure is not allowed to build up below the hydrate layer. As a result, free gas would move through the RHSZ by generating three-phase equilibrium more likely than by opening fractures.

5.4 Implications for the presence of BSR

A strong BSR is present where the base of the hydrate zone coincides with the top of free gas [*Bangs et al.*, 1993; *Holbrook et al.*, 1996]. At high gas flux, a three-phase zone appears in the RHSZ, Three phases coexist over a range of depths, instead of an interface only. Free gas is continuously present across the base of the RHSZ, reducing the contrast in acoustic impedance. Thus a weak or disrupted BSR is formed. However, at low gas flux, hydrate and free gas coexist at the base of hydrate stability zone, producing a strong BSR. The spike in S_h at the base of the stability zone also strengths the BSR. Simulations indicate that strong BSRs are present in low-gas flux regions where the base of gas hydrate coincides with the top of free gas, whereas weak or disrupted BSRs occurs in high-gas flux regions (*e.g.*, southern Hydrate Ridge).

6. Conclusions

(1) In coarse-grained sediments, hydrate formation at the base of the RHSZ cannot increase the capillary entry pressure enough to trap free gas. Thus a large amount

of free gas is supplied into the RHSZ to produce a significant increase in salinity via hydrate formation. High salinity pore water can freely transport free gas through the RHSZ toward the seafloor. In this system, hydrate concentration increases toward the seafloor and all hydrates are located at three-phase equilibrium.

(2) In fine-grained sediment, hydrate formation at the base of the RHSZ leads to rapid permeability reduction and capillary sealing with respect to gas. The capillary seal prevents methane gas from migrating. Thus free gas progressively accumulates beneath the hydrate zone until the critical gas column height is reached. Thereafter the gas pressure at the top of gas column is sufficient to fracture the overlying sediments, thus forcing gas venting through the RHSZ.

(3) In regions of high gas flux, lateral diffusion of salts is slow enough for gas chimney to rapidly extend to the seafloor. Thus the salinity halo is only significant in the immediate vicinity of chimney. Increases in capillary pressure with hydrate formation divert gas flow laterally, leading to the lateral growth of chimney and hydrate.

Nomenclature

κ – component
m – methane component
s – salt component
w – water component
β – phase
h – hydrate phase
l – liquid phase
v – vapor phase
ϕ – porosity (dimensionless)

β_ϕ – pore compressibility (Pa^{-1})

ρ_β – density of phase β (Pa^{-1})

μ_β – viscosity of phase β (Pa·s)

k – absolute permeability (m^2)

$k_{r\beta}$ – relative permeability of phase β (dimensionless)

q^κ – source or sink of component κ ($kg\ m^{-3}\ s^{-1}$)

v_β – Darcy velocity of phase β ($m\ s^{-1}$)

D^κ – chemical diffusivity of component κ ($m^2\ s^{-1}$)

F^κ – mass flux of component κ ($kg\ m^{-2}\ s^{-1}$)

M^κ – mass accumulation of component κ ($kg\ m^{-3}\ s^{-1}$)

P_β – pressure of phase β (Pa)

S_β – saturation of phase β (dimensionless)

T – temperature (°C)

X_β^k – mass fraction of component κ in phase β (dimensionless)

Chapter 4

NUMERICAL MODELING OF HYDRATE DISSOCIATION IN MARINE SEDIMENTS

Abstract

The response of methane hydrate to environmental changes strongly depends on the *in situ* hydrate stability and hydrate formation mechanism. At high gas flux, hydrate is formed as a three-phase (hydrate + liquid + gas) zone extends from the base of hydrate stability to the seafloor. All hydrates within this zone are already at the three-phase boundary, and thus are most vulnerable to methane release. Within the three-phase zone, hydrate dissociation is thermodynamically regulated by the decrease in salinity required for three-phase equilibrium with increasing temperature. The three-phase zone is also critical for transporting the dissociated free gas to the ocean. We estimate that at South Hydrate Ridge, bottom-water warming from 4°C to 8°C can release ~70% of methane stored in hydrates from the three-phase zone, offering a mechanism for rapid methane release during the warming event.

1. Introduction

Hydrate is an ice-like mineral formed when water freezes in the presence of sufficient methane and other low molecular weight gases [*Sloan*, 1998]. Gas hydrate is stable at high pressures and low temperatures, commonly found along continental margins at water depths greater than 300 m [*Kvenvolden*, 1993]. Because temperature increases with depth, gas hydrate is stable only in the upper few hundred meters below seafloor. The shallowness of the hydrate stability zone implies that changes in pressure and temperature at the seafloor would result in the dissociation or formation of sub-seafloor gas hydrates [*MacDonald et al.*, 1990]. Because as much as ~10,000 GT of carbon may be trapped in marine methane hydrate [*Kvenvolden*, 1993], hydrate dissociation and methane escape to the ocean and atmosphere may play a role in global climate [*Dickens et al.*, 1995; *Kennett et al.*, 2000; *Dickens*, 2003]. However, the nature and mechanism of gas escape to the ocean is poorly understood. In particular, the hydrate phase equilibrium (*e.g.*, its proximity to the three-phase boundary) and its role in gas escape and climate change are unclear.

Dickens et al. [1995] suggested the release of methane from the seafloor sediments during the late Paleocene thermal maximum (LPTM). They showed that the observed excursion of $\delta^{13}C$ recorded in carbonate and organic matter deposited during this time is consistent with the addition of $\sim 10^{18}$ g of CH_4 from methane gas hydrate to the oceans over $\sim 10^4$ years.

Harvey and Huang [1995] and *Xu et al.* [2001] investigated the response of oceanic hydrates to seafloor pressure *P* and temperature *T* changes and determined the change in seafloor methane flux as a result of hydrate dissociation. In their models,

hydrates are initially at two-phase equilibrium (hydrate + liquid), dissociated gas is transported to the seafloor by aqueous flow, and the emission rate is limited by the low methane solubility in water. Although the temperature increase may release a large amount of methane from hydrates near the base of the initial hydrate stability zone, much of dissociated gas will migrate back into the stability zone and recrystallize as hydrate at shallower depths. Thus hydrate dissociation cannot cause a large increase in methane emission to the ocean.

In this chapter, we extend the model that we have developed to include hydrate dissociation due to environmental changes. The extended model is used to investigate the response of hydrate reservoirs to an abrupt temperature increase at the seafloor in two scenarios. In one scenario, hydrates are initially at two-phase (hydrate +liquid) equilibrium, while in the other scenario, hydrates are initially at three-phase (hydrate+liquid+gas) equilibrium. In both scenarios, we quantify the changes in the vertical distribution of gas hydrate/free gas and the methane emission across the seafloor, as a result of hydrate dissociation.

Our simulations suggest that the changes in methane emission to the ocean strongly depend on hydrate stability and its formation mechanism. In regions of low gas flux, hydrate is precipitated from water in the two-phase (hydrate + liquid) region. The dissociated gas cannot be released to the ocean until the warming is large enough to completely dissociate the original hydrate layer. However, in regions of high gas flux, hydrate is formed as a three-phase zone progressively expands to the seafloor. The three-phase zone increases the amount of hydrates located at the three-phase (hydrate + liquid + gas) boundary; hence it would easily and rapidly respond to changes in external

conditions. The three-phase zone also provides a mechanism for transporting the dissociated gas to the ocean. We show that a 4°C increase in seafloor temperature can release 70% of methane previously stored in hydrates from the three-phase zone.

2. Governing Equations, Processes and Assumptions

The process of methane release to the ocean involves multi-phase fluid flow within a sediment-gas-water system. We extend the model developed for hydrate formation (Appendix C) to describe hydrate dissociation in oceanic sediments. Similarly, there are three mass balance (methane, water salt) equations (Appendix C.1-C.3) and one energy balance equation (Appendix C.4). These balance equations, combined with the thermodynamic conditions, provide a complete description of hydrate dissociation in porous media.

Hydrate dissociation has negative feedbacks on the dissociation process itself [*Xu et al.*, 2001; *Xu*, 2002]. For example, pressure builds up with hydrate dissociation. This increase in pressure tends to stabilize hydrate and inhibit further dissociation. Hydrate dissociation also releases fresh water and locally decreases pore water salinity. This decrease in salinity can suppress further hydrate dissociation. The model presented here includes these dynamic feedbacks of hydrate dissociation.

We assume the following. (1) Hydrate dissociation follows equilibrium. (2) Latent heat associated with hydrate formation and dissociation is neglected. (3) The effect of *in situ* methane production and sedimentation is neglected. (4) Fluid flow in both liquid and gas phases occur under pressure, capillary and gravitational forces, according to the multiphase Darcy's law that includes the effect of relative permeability. (5) Most of the

dissociated methane is transported upward by free gas migration. (6) Diffusion is only considered in the liquid phase.

3. Simulation Results

We run three different models to show the processes of hydrate dissociation in the present-day marine environment with bottom-water temperature of ~4°C (table 1): (1) dissociation of hydrates at two-phase equilibrium in response to a small (*Case 1*) and a large (*Case 2*) warming event; (2) dissociation of hydrates at three-phase equilibrium in response to a small warming event (*Case 3*). All scenarios are run in sand.

3.1 Dissociation of hydrates at two-phase equilibrium

The model is initialized by running it for 300 Ka with the methane, water and salt fluxes of 0.004, 2.50 and 0.75 kg m^{-2} yr^{-1}. Initially, hydrates occupy only ~5% pore volume in the center of the hydrate stability zone (Fig. 4-1C, t_1), where the methane concentration exceeds the solubility (Fig. 4-1B, t_1). There is no significant salinity buildup (Fig. 4-1D, t_1) and no free gas (Fig. 4-1C, t_1). This hydrate system is at two-phase equilibrium, where the liquid phase (with dissolved gas) coexists in equilibrium with hydrate. The temperature of hydrate is lower than the three-phase boundary (Fig. 4-1A, t_1). We evaluate the response of this hydrate system to a sudden warming.

3.1.1 Case 1: A bottom-water warming of 4°C

A sudden temperature increase from 4°C to 8°C is imposed at the seafloor. A thermal front propagates downward (Fig. 4-1A, t_2). The intersection of geotherm with the three-phase (*L+G+H*) boundary defines the base of the hydrate stability zone, which correspondingly shifts upward. Dissociation begins at the bottom of the hydrate zone, while hydrates above remain stable. Then dissociation progresses upward. Dissociation of

Table 3 Initial conditions and amounts of methane release for three hydrate dissociation scenarios

	Dissociation Case 1	**Dissociation Case 2**	**Dissociation Case 3**
q^m (methane flux)	0.004 kg m^{-2} yr^{-1}	0.004 kg m^{-2} yr^{-1}	0.96 kg m^{-2} yr^{-1}
q^w (water flux)	2.50 kg m^{-2} yr^{-1}	2.50 kg m^{-2} yr^{-1}	0
q^s (salt flux)	0.75 kg m^{-2} yr^{-1}	0.75 kg m^{-2} yr^{-1}	0
q^e (heat flux)	55 mW m^{-2}	55 mW m^{-2}	55 mW m^{-2}
In situ hydrate stability	Two-phase equilibrium	Two-phase equilibrium	Three-phase equilibrium
Initial bottom-water temperature	4 °C	4 °C	4 °C
Initial amount of CH_4 in hydrate per m^2 seafloor	366 kg	366 kg	5950 kg
Initial amount of CH_4 in free gas per m^2 seafloor	0 kg	0 kg	530 kg
Initial amount of CH_4 in liquid per m^2 seafloor	444 kg	444 kg	312 kg
Total initial amount of CH_4 per m^2 seafloor	810 kg	810 kg	6792 kg
Bottom-water warming	4 °C	8 °C	4 °C
Amount of CH_4 in hydrate per m^2 seafloor after warming	191 kg	0 kg	2046 kg
Amount of CH_4 in free gas per m^2 seafloor after warming	172 kg	158 kg	548 kg
Amount of CH_4 in liquid per m^2 seafloor after warming	454 kg	469 kg	360 kg
Total amount of CH_4 per m^2 seafloor after warming	817 kg	627 kg	2954 kg

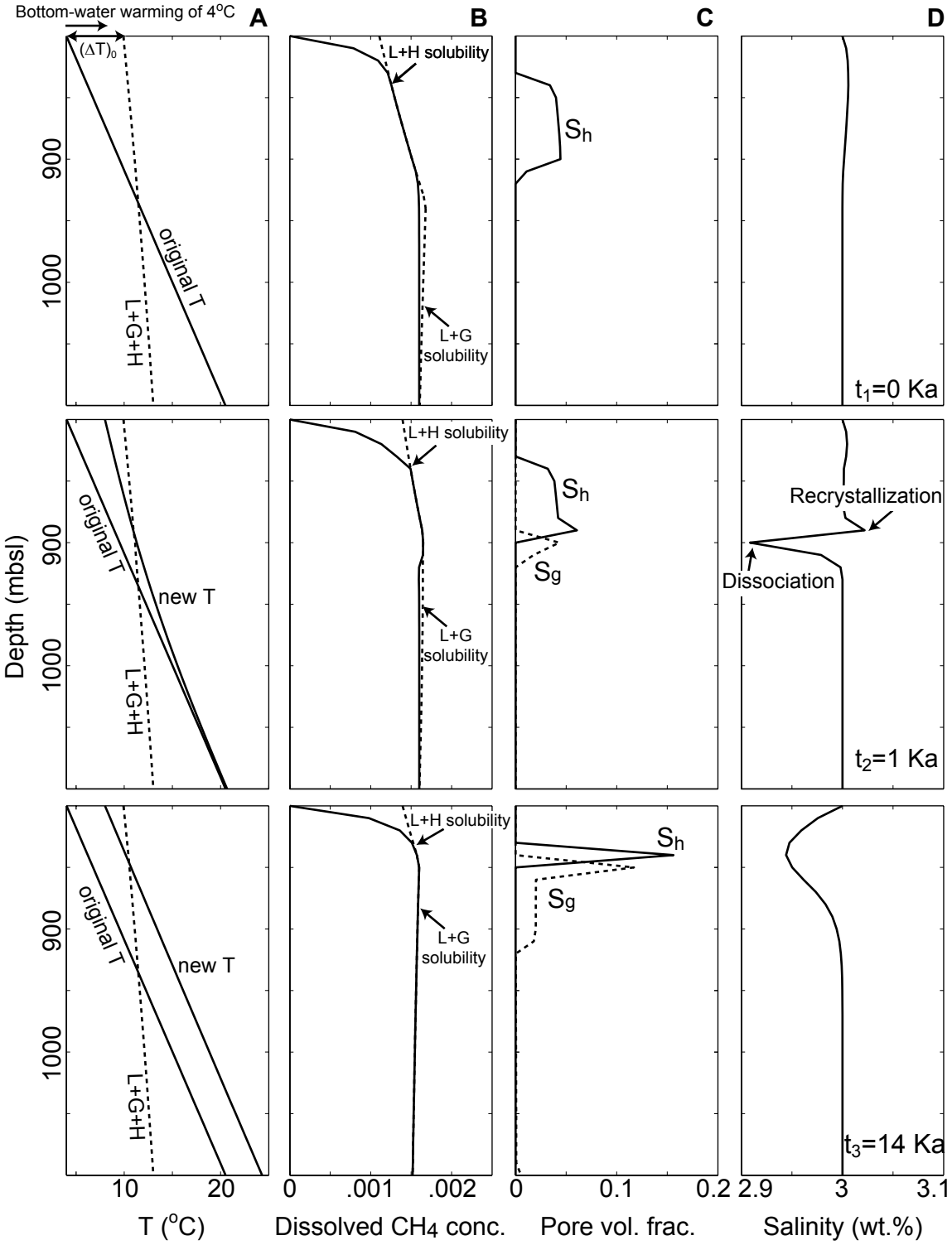

Fig. 4-1: Evolution of (A) temperature, (B) dissolved methane concentration, (C) water and gas fractions of pore volume, and (D) salinity at three times (0, 1 and 14 Ka) during hydrate dissociation. The temperature at the seafloor increases from 4°C to 8°C. Hydrates are initially at two-phase equilibrium. $(\Delta T)_0$ is the minimum bottom-water warming required for hydrates to be completely dissociated.

hydrate produces free gas below the shoaling base of the hydrate zone (Fig. 4-1C, t_2). Due to the large contrast in density between water and gas, dissociated gas migrates upwards under buoyancy once the residual gas saturation (S_{rg}=2%) is exceeded. However, upward-migrating gas recrystallizes as hydrate at shallower depth, producing a spike in S_h (Fig. 4-1C, t_2). Hydrate dissociation releases fresh water and decreases salinity, whereas recrystallization depletes fresh water and increases salinity (Fig. 4-1D, t_2).

The temperature re-equilibrates after ~14 Ka (Fig. 4-1A, t_3). In this case, the 4°C seafloor temperature increase does not completely dissociate the original hydrate zone. The base of hydrate stability zone shoals from 130 to 50 mbsf (meters below seafloor) (Fig. 4-1A, t_3). Hydrate is progressively enriched (~15% pore volume) at the base of the new hydrate stability zone by a process of continuous dissociation, upward transport of gas and recrystallization at shallower depths (Fig. 4-1C, t_3). A small fraction of dissociated gas remains in sediments below the layer of concentrated hydrate (Fig. 4-1C, t_3), where S_g is near the residual value (~2%) and gas becomes immobile.

The methane emission rate at the seafloor increases very little (Fig. 4-2). In this case, only dissolved methane is vented to the ocean and the rate is limited by its low solubility in pore water. Methane concentration is always sustained at its solubility in the hydrate zone, while it is set to zero at the seafloor. Methane solubility in the presence of hydrate (L+H) slightly increases with temperature (Fig. 4-1B), causing a steeper curvature in methane concentration near the seafloor. Thus the methane emission to the ocean increases. But the maximum venting rate increase caused by the seafloor temperature increase is only 20% of its original level (~0.4×10^{-10} kg m^{-2} s^{-1}) (dashed line in Fig. 4-2).

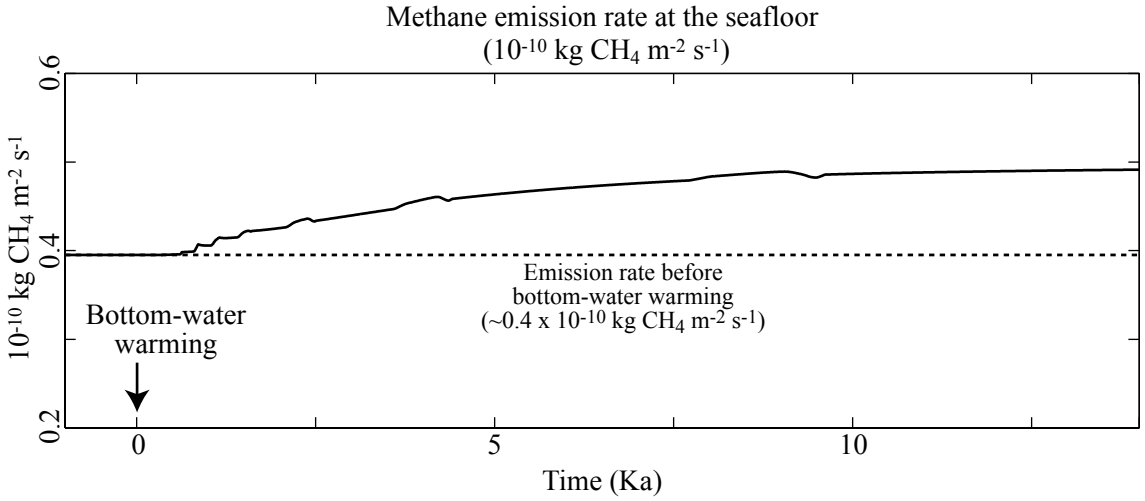

Fig. 4-2: Change in methane flux to the ocean (solid line) as the temperature at the seafloor increases from 4°C to 8°C. The dashed line is the methane flux to the ocean before the seafloor temperature increases.

3.1.2 Case 2: A bottom-water warming of 8°C

Case 2 differs from *Case 1* only in that a sudden temperature increase from 4°C to 12°C is imposed at the seafloor. In this case, dissociation begins instead at the top of the hydrate zone (Fig. 4-3C, t_2), where the temperature reaches the three-phase (L+G+H) boundary curve (Fig. 4-3A, t_2), and then progresses downward; dissociated gas in this region rapidly migrates to the surface under buoyancy without being recrystallized as hydrate at shallower depths. Hydrate dissociation at the top of the hydrate zone releases fresh water and decreases salinity (Fig. 4-3D, t_2).

At t_3, the temperature is everywhere elevated above the three-phase boundary curve (Fig. 4-3A, t_3). The imposed warming exceeds the difference between the *in situ* temperature and the temperature for three-phase equilibrium at the seafloor (Fig. 4-3A, t_1) and the new base of the hydrate stability zone is situated well above the seafloor. Thus warming can eliminate the hydrate stability zone entirely, and most of dissociated gas can freely migrate to the seafloor, which results in a high rate of methane emission. A small faction of dissociated gas (~2% pore volume) remains in the system (Fig. 4-3C, t_3), because gas permeability becomes small when S_g is reduced to the residual level.

The change in methane emission to the ocean occurs rapidly (Fig. 4-4). There is a ~0.4 Ka lag between the increase in gas venting and the surface temperature perturbation, which is the time required for the thermal front to propagate downward and the dissociated gas to migrate upward. When dissociated free gas reaches the seafloor, the gas venting rate greatly increases to ~500 times (~0.2×10^{-7} kg m^{-2} s^{-1}) of its original level (~0.4×10^{-10} kg m^{-2} s^{-1}), but lasts only for a short time (Fig. 4-4). Because warming can

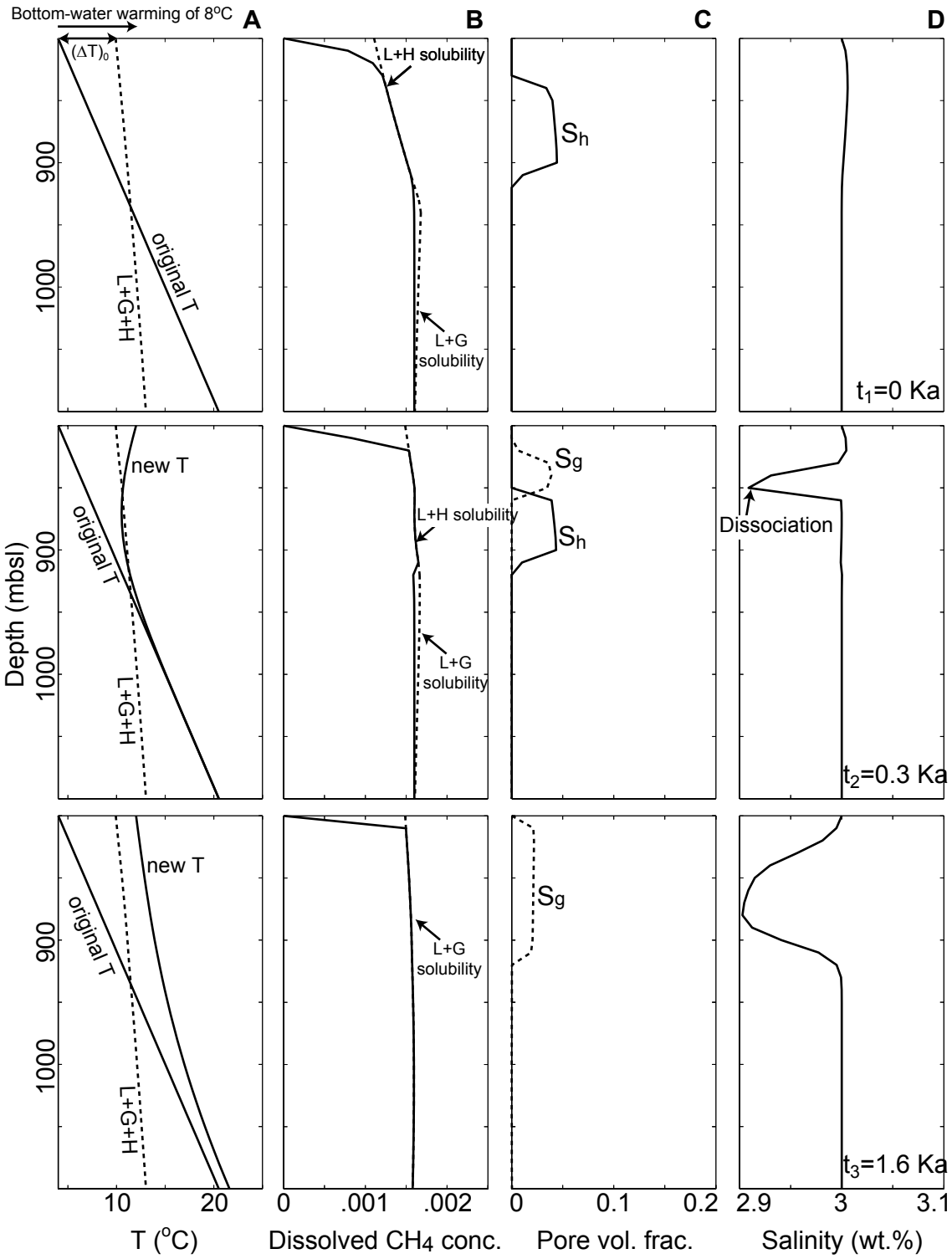

Fig. 4-3: Evolution of (A) temperature, (B) dissolved CH_4 concentration, (C) water and gas fractions of pore volume, and (D) salinity at three times (0, 0.3 and 1.6 Ka) during hydrate dissociation. The temperature at the seafloor increases from 4°C to 12°C. Hydrates are initially at two-phase equilibrium. $(\Delta T)_0$ is the minimum bottom-water warming required for hydrates to be completely dissociated.

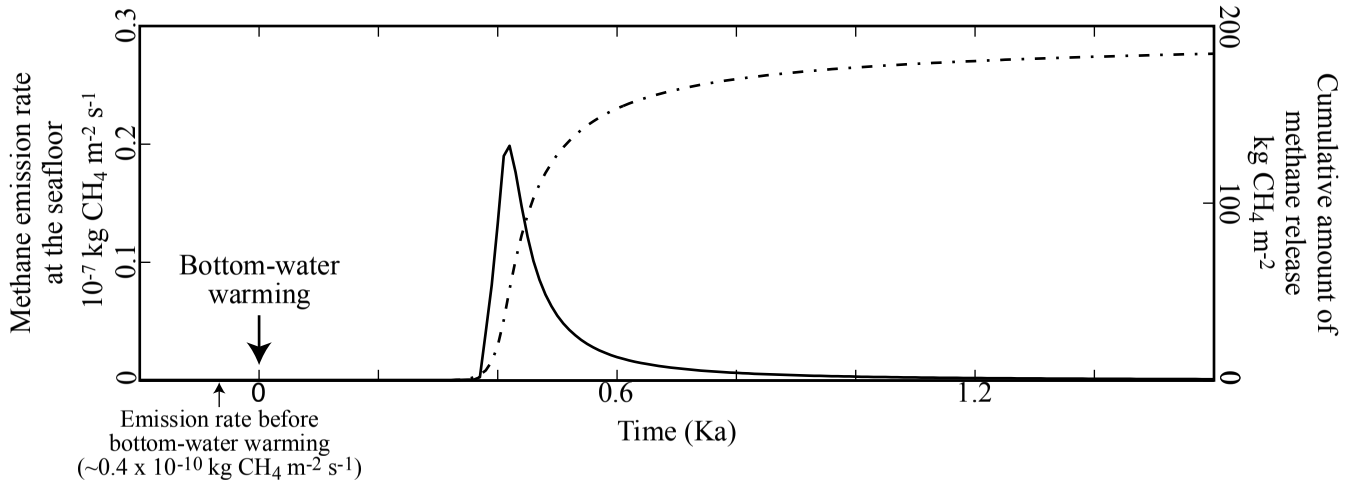

Fig. 4-4: Change in methane flux to the ocean (solid line) as the temperature at the seafloor increases from 4°C to 12°C. The maximum methane flux rate lags behind the increase in seafloor temperature by ~0.4 Ka.

eliminate the hydrate stability zone entirely, the increase in gas venting rate is much larger than that obtained under a seafloor temperature increase of only 4°C.

3.2 Dissociation of hydrates at three-phase equilibrium (*Case 3*: A bottom-water warming of 4°C)

A high gas flux must be present to produce a three-phase system. The model is initialized (dashed lines in Fig. 4-5) by running it for 7 Ka with the basal gas flux of 0.96 kg m^2 yr^{-1}. This gas flux is close to that found at southern Hydrate Ridge [*Torres et al.*, 2004]. Initially, a three-phase zone extends from the base of hydrate stability to the seafloor, in which three phases coexist and hydrate is concentrated toward the seafloor (~80% pore volume). The free gas within the three-phase zone forms an interconnected phase, providing a direct pathway for free gas migration through the hydrate stability zone. A sudden temperature increase from 4°C to 8°C is imposed at the seafloor. The simulation is then carried out for another 20 Ka.

The pore pressure dissipates fast in sand during hydrate dissociation. A pressure surge travels downward as dissociation proceeds (Fig. 4-6). Its magnitude reaches a maximum of only ~0.06 MPa and decreases with time. The pressure surge results from the sudden release of methane from the dissociating hydrates, because the dissociated gas and water occupy a greater volume than the original hydrate (Fig. 4-6 inset) [*Kvenvolden*, 1993]. However, the three-phase zone can efficiently remove the dissociated gas from the hydrate to the seafloor. Thus there is no significant pressure build-up during dissociation to inhibit further dissociation.

A thermal front propagates downward after the surface temperature perturbation is imposed (Fig. 4-5A). Hydrate dissociation occurs first immediately below the seafloor

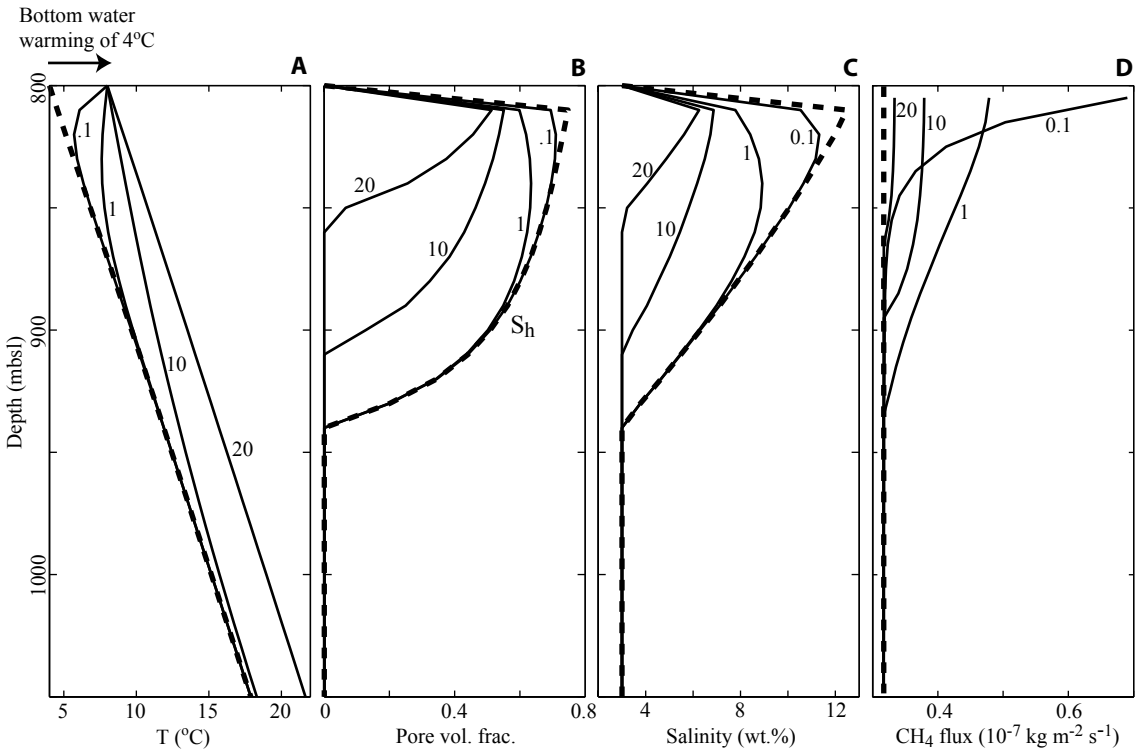

Fig. 4-5: Effect of a temperature increase on the underlying hydrate system. Hydrates are initially at three-phase equilibrium. The dashed lines indicate the initial conditions. The numbers represent the time (in Ka) after bottom-water warming. (A) Subsurface temperature following an increase in bottom water temperature from 4^{o}C to 8^{o}C. The bottom water temperature gradually propagates into the sediments. The hydrate saturation (B) and salinity (C) associated with the temperature changes in (A). The salinity drops to the background seawater value where the hydrate is completely depleted. (D) Changes in gas flux during hydrate dissociation.

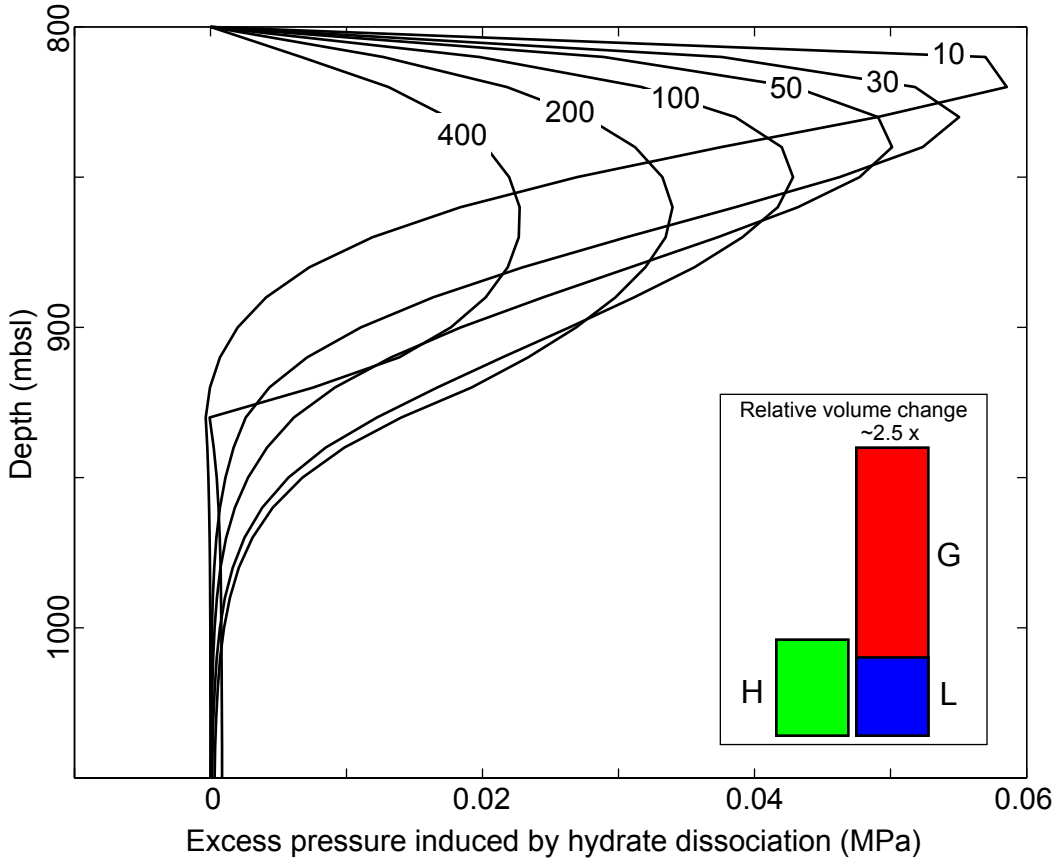

Fig. 4-6: A pressure surge associated with hydrate dissociation. Box showes the relative volume change associated with gas hydrate (H) decomposing into liquid water (L) and free gas (G). The numbers represent the time in years after bottom water warming. The peak excess pressure decreases with time. Pressure build-up generated from hydrate dissociation is not sufficient to thermodynamically inhibit further hydrate dissociation.

(Fig. 4-5B) and progresses downward; and dissociated methane in this region is rapidly released to the ocean. At <1 Ka, the thermal gradient is reversed near the seafloor (Fig. 4-5A) and induces downward heat flow from the ocean. Later, hydrate dissociation also occurs at the base of the hydrate zone, when the warming reaches this depth at ~2 Ka. The temperature eventually re-equilibrates at ~20 Ka.

Hydrate dissociation releases fresh water and decreases salinity (Fig. 4-5C). The dissociation process follows equilibrium and the decreased salinity inhibits further hydrate dissociation. Note that if pressure changes small, the salinity needed for three-phase equilibrium decreases sharply with increasing temperature [*Liu and Flemings*, 2005]. Hydrate dissociation continues until the salinity decreases to the point that venting gas is in equilibrium with undissociated hydrate at the elevated temperature. As a result, in regions where three phases coexist, the evolving P, T and salinity follow the three-phase stability conditions during dissociation until hydrate is completely depleted.

The gas flux increases toward the seafloor as dissociated gas is added to the venting gas at each depth (Fig. 4-5D). As the thermal front propagates downward, the thermal gradient increases with depth (Fig. 4-5A). The continuous variations in thermal gradient allow hydrates to dissociate over a broad zone (Fig. 4-5B), where large amounts of methane gas are released. The dissociated gas then rises buoyantly. However, in this case, the upward-migrating gas does not refreeze at shallower depths, because the three-phase stability conditions are always sustained during hydrate dissociation. Thus most of the dissociated gas can reach the seafloor with the direct pathway provided by the three-phase zone. Due to the high mobility of dissociated gas, the buoyancy effect and the pressure increase caused by volume expansion lead to the immediate release of methane

at the seafloor. Therefore, in this case, the dissociation of sub-seafloor hydrates can directly affect the gas venting rate at the seafloor (Fig. 4-5D).

A new three-phase zone exists closer to the seafloor after the temperature re-equilibrates at ~20 Ka (Fig. 4-5B). The new three-phase zone becomes thinner, fresher and less hydrate-enriched. Small amount of hydrate (~20% pore volume) remains in this zone, where the decreased salinity caused by dissociation stabilizes hydrate and prevents further dissociation (Fig. 4-5C). The undissociated hydrate is now in equilibrium with venting gas at the increased temperature and decreased salinity. The hydrates in the region between the original and new three-phase zone (dashed line and 20 Ka in Fig. 4-5B, respectively) have dissociated. The dissociated free gas escapes to the ocean via the three-phase zone rather than recrystallizes at shallower depths. Fig. 4-5B shows that a 4°C temperature increase at the seafloor can release 70% of methane previously trapped in hydrates through the three-phase zone.

The gas venting rate across the seafloor changes rapidly (Fig. 4-7). The largest increase in venting rate occurs shortly after the step-function temperature increase. Then this response gradually decreases to the basal gas flux through the system (dashed line). The maximum venting rate caused by bottom-water warming more than doubles the basal gas flux, which is already high (~0.32×10^{-7} kg m^{-2} s^{-1}). And the elevated gas venting rate persists for several thousand years.

There is no time lag between the increase in gas venting rate and the increase in seafloor temperature (Fig. 4-7). The reasons are: (1) hydrates are already at the three-phase boundary. Thus hydrates need not be heated to the three-phase boundary before they dissociate; (2) the reversed thermal gradient near the surface induces downward heat

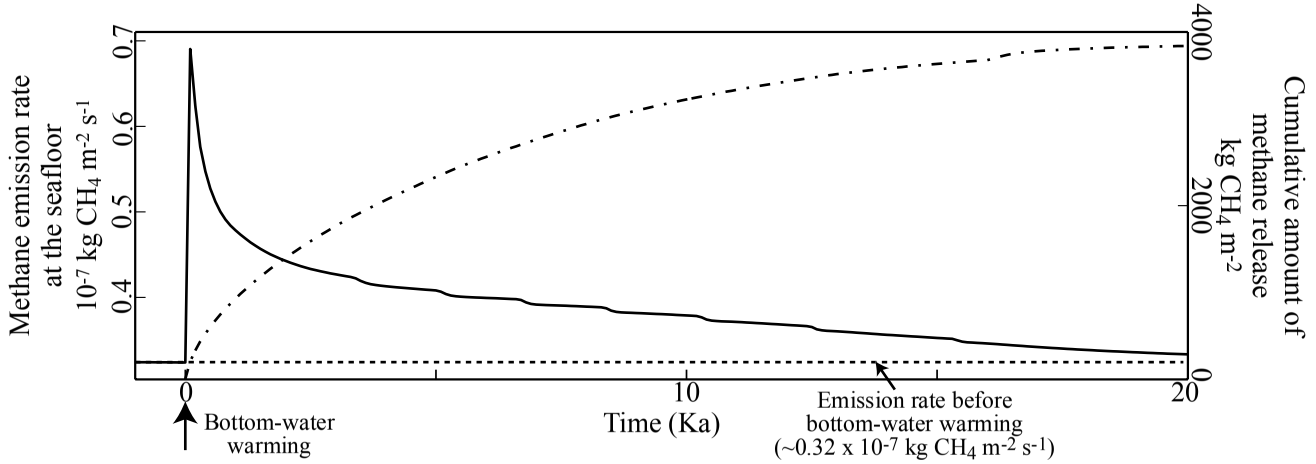

Fig. 4-7: Change in methane flux to the ocean (solid line) as the temperature at the seafloor increases from 4°C to 8°C. There is no time lag between the increase in the rate of gas venting and the bottom-water warming. The dashed line is the methane flux to the ocean before the seafloor temperature increases.

flow, accelerating hydrate dissociation; (3) dissociated gas is removed rapidly enough that pressures do not increase sufficiently to inhibit further dissociation.

4. Discussion

4.1 Hydrate reservoir stability

According to *Case 1* and *Case 2*, if hydrates are initially at two-phase equilibrium, a significant increase in gas venting rates occurs only if the bottom-water warming is large enough to completely eliminate the hydrate stability zone. If water depth is 800 m and bottom-water temperature is 4°C (present-day condition), we calculate that a warming of >6.5°C at the seafloor is required for hydrates initially at two-phase equilibrium to be completely destabilized and released to the ocean.

However, *Case 3* suggests that seafloor temperature increase may release a large amount of methane stored in hydrates to the ocean, if hydrates are initially at three-phase equilibrium. There are two main reasons for this behavior. First, dissociated methane is transported upward as free gas and the emission rate is not limited by the low methane solubility in water. Most of the dissociated gases can directly escape to the ocean via the three-phase zone and do not refreeze at shallower depths. Second, a concentrated hydrate accumulation at three-phase equilibrium is initially available for dissociation. Changes in *P*-*T*-salinity in the hydrate zone follow equilibrium during dissociation. The salinity necessary for three-phase equilibrium decreases rapidly with temperature [*Liu and Flemings*, 2005]. Thus for the three-phase equilibrium to be sustained at the increased temperature, a large amount of hydrate must be dissociated to decrease salinity. The sharp increase in seafloor gas venting indicates that hydrates at three-phase equilibrium may play an important role in the climate changes.

Our model is analogous to that in *Cathles and Chen* [2004]. They presented a kinetic model of hydrate dissociation caused by changes in bottom-water temperature. Gas hydrate and free gas initially coexist throughout the hydrate stability zone. Due to the fractionation effect, gas hydrate is initially enriched in wet gas components (C_3+C_4), while venting gas is depleted in C_3+C_4. As temperature increases, hydrate must be dissociated to release C_3+C_4 to bring the gas into equilibrium with hydrate. In our model, the hydrate zone is buffered at three-phase equilibrium by the presence of salts in pore water. Similarly, hydrate must be dissociated to release fresh water to maintain the three-phase equilibrium at the increased temperature.

There are evidences for very rapid dissociation of hydrate. Measured excursions in venting rate exhibit a positive correlation with increases in bottom-water temperature over time at Bush Hill, Gulf of Mexico [*MacDonald et al.*, 1994; *Cathles and Chen*, 2004]. Gas venting is affected by changes in tidal loading at Hydrate Ridge [*Torres et al.*, 2002]. Gas vents and near-seafloor hydrates occur at both Bush Hill and Hydrate Ridge, where methane may coexist in all three phases. These hydrates at three-phase equilibrium would more easily and rapidly respond to bottom-water warming or sea-level lowering. Only small, short-term transient seafloor *P*-*T* changes can initiate hydrate dissociation. We envision that variations in seafloor gas venting are consistent with the dissociation of hydrates at three-phase equilibrium and the consequent release of methane, caused by changes in external conditions.

The hydrate accumulation at three-phase equilibrium also has important implications for gas production from natural hydrates. High hydrate concentrations initially occur because of the basal high gas flux. This accumulation is more easily

recovered because of its proximity to the dissociation boundary. The minimum amount of pressure drop, thermal energy and inhibitor is required to stimulate recovery.

4.2 Rapid methane release by submarine landslides

Another efficient mechanism for releasing methane to the ocean is the slumping on the continental margins. The volume change associated with hydrate dissociation can elevate pore pressure and reduce the strength of the sediment [*Kayen and Lee*, 1991]. A large pressure buildup due to hydrate dissociation may lead to slope failures where gas hydrate is present, such as the Beaufort Sea Margin [*Kayen and Lee*, 1991], the Cape Fear Slide of the Blake Ridge [*Paull et al.*, 1996], and the Storegga Slide of the Norwegian Margin [*Vogt and Jung*, 2002]. Consequently, these slope failures could also cause rapid release of both the destabilized methane and the free gas previously trapped below the hydrate zone.

The development of excess pressure during hydrate dissociation is largely controlled by pressure dissipation properties (*i.e.*, permeability and compressibility) of the sediment [*Kayen and Lee*, 1991]. In relatively permeable sand, dissociated free gas is readily removed from the hydrate via the three-phase zone, and pressure is then allowed to dissipate by fluid flow. Thus no significant pressure builds up to potentially induce slope failure in this case (Fig. 4-6).

4. Conclusions

(1) Hydrate coexists with liquid water in regions of low gas flux. In this type of hydrate system, although a temperature increase can release a large amount of gas from hydrate, the dissociated gas will move upward and refreeze as hydrate at shallower depths. Thus the dissociation process does not directly affect the methane emission to the

ocean. The dissociated free gas can escape to the ocean only when the surface warming is so high that no hydrate can remain stable at the seafloor.

(2) Massive release of methane from gas hydrate depends on its proximity to the three-phase boundary. Where methane flux is high, there is a three-phase zone from the base of the hydrate stability zone to the seafloor. The three-phase zone increases the amount of hydrates located at the three-phase boundary; thus it can rapidly respond to environmental changes. Hydrate dissociation within the three-phase zone is regulated by changes in salinity required for three-phase equilibrium with temperature. The dissociated free gas can be released to the ocean via the three phase zone, even though hydrates do not completely dissociate during a small warming event. We estimate that a 4°C increase in seafloor temperature can release 70% of methane stored in the hydrate system that is initially at three-phase equilibrium, providing a mechanism for rapid methane release.

BIBLIOGRAPHY

Abegg, F., J. Freitag, G. Bohrmann, W. Brueckmann, A. Eisenhauer, H. Aman, and H.-J. Hohnberg, Free gas bubbles in the hydrate stability zone: evidence from CT investigation under in situ conditions, *Spring 2003 abstract #EAE-A-10342, AGU meeting, Nice, France*, 2003.

Amyx, J.W., D.M., Bass, Jr. and R.L. Whiting, *Petroleum Reservoir Engineering*, 610 pp., McGraw-Hill, New York, 1960.

Bangs, N.L., D. S. Sawyer, and X. Golovchenko, Free gas at the base of the gas hydrate zone in the vicinity of the Chile triple junction, *Geology*, *21*, 905-908, 1993.

Bear, J., *Dynamics of fluids in porous media*, Dover, New York, 1972.

Cathles, L.M., and D. F. Chen, A compositional kinetic model of hydrate crystallization and dissolution, *Journal of Geophysical Research*, *109*, doi:10.1029/2003JB002910, 2004.

Class, H., R. Helmig, and P. Bastian, Numerical simulation of non-isothermal multiphase multicomponent processes in porous media. 1. An efficient solution technique, *Advances in water resources*, *25*, 533-550, 2002.

Clennell, M.B., W. J. Winters, M. Hovland, J. S. Booth, and P. Henry, Formation of natural gas hydrates in marine sediments 1. Conceptual model of gas hydrate growth conditioned by host sediment properties, *Journal of Geophysical Research*, *104*, 22985-23003, 1999.

Collett, T.S., and J. Ladd, Detection of gas hydrate with downhole logs and assessment of gas hydrate concentrations (saturations) and gas volumes on the Blake Ridge with electrical resistivity log data, *Proceedings of the Ocean Drilling Program Scientific Results*, *164*, 179-191, 2000.

Davie, M.K., and B. A. Buffett, A numerical model for the formation of gas hydrate below the seafloor, *Journal of Geophysical Research*, *106*, 497-514, 2001.

Davie, M.K., and B. A. Buffett, A steady state model for marine hydrate formation: Constraints on methane supply from pore water sulfate profile, *Journal of Geophysical Research*, *108*, doi:1029:2002JB002300, 2003.

Dickens, G.R., J. R. O'Neil, D. K. Rea, R. M. Owen, Dissociation of oceanic methane hydrate as a cause of the carbon isotope excursion at the end of the Paleocene, *Paleoceanography*, *10*, 965-971, 1995.

Dickens, G.R., Rethinking the global carbon cycle with a large, dynamic and microbially mediated gas hydrate capacitor, *Earth and Planetary Science Letters*, *213*, 169-183, 2003.

Dickens, G.R., and M. S. Quinby-Hunt, Methane hydrate stability in pore water: a simple theoretical approach for geophysical applications, *Journal of geophysical research*, *102*, 773-783, 1997.

Duan, Z.H., N. Moller, J. Greenberg, and J. H. Weare, The prediction of methane solubility in natural waters to high ionic strength from 0 to 250C and from 0 to 1600 bar, *Geochimica et Cosmochimica Acta*, *56*, 1451-1460, 1992.

Dugan, B., Measuring Pore Pressure in Marine Sediments with Penetrometers: Comparison of the Piezoprobe and DVTP-P Tools in ODP Leg 204, *Research Papers of the Link Foundation Fellows*, *3*, 179-199, 2003.

England, W.A., A. S. Mackenzie, D. M. Mann, and T. M. Quigley, The movement and entrapment of petroelum fluids in the subsurface, *Journal of the Geological Society, London*, *144*, 327-347, 1987.

Falta, R.W., K. Pruess, I. Javandel, P. A. Witherpoon, Numerical modeling of steam injection for the removal of nonaqueous phase liquids from the subsurface, *Water Resource Research*, *28*, 433-449, 1992.

Farnstrom, K.L., and T. Ertekin, A versatile, fully implicit, black oil simulator with variable bubble-point option, *SPE*, 16342, 1987.

Fetter, C.W., *Applied hydrogeology*, 598 pp., Prentice Hall, New Jersey, 1994.

Ginsburg, G.D., and V. A. Soloviev, Methane migration within submarine gas-hydrate stability zone under deep-water conditions, *Marine Geology*, *137*, 49-57, 1997.

Haeckel, M., E. Suess, K. Wallmann, and D. Rickert, Rising methane gas bubbles form massive hydrate layers at the seafloor, *Geochimica et Cosmochimica Acta*, *68*, 4335-4345, 2004.

Handa, Y.P., Effect of hydrostatic pressure and salinity on the stability of gas hydrates, *Journal of Physical Chemistry*, *94*, 2652-2657, 1990.

Harvey, L.D., and Z. Huang, Evaluation of the potential impact of methane clathrate destabilization ob future global warming, *Journal of Geophysical Research*, *100*, 2905-2926, 1995.

Heeschen, K.U., A. M. Trehu, R. W. Collier, E. Suess, and G. Rehder, Distribution and height of methane bubble plumes on the Cascadia Margin characterized by acoustic imaging, *Geophysical Research Letters*, *30*, 1-4, 2002.

Henry, P., M. Thomas, and M. B. Clennell, Formation of natural gas hydrates in marine sediments 2. Thermodynamic calculations of stability conditions in porous sediments, *Journal of Geophysical Research*, *104*, 23005-23022, 1999.

Hesse, R., and W. Harrison, Gas hydrate (clathrate) causing pore water freshening and oxygen isotope fractionation in deep-water sedimentary sections of terrigenous continental margins, *Earth and Planetary Science Letters*, *55*, 55453-55462, 1981.

Holbrook, W.S., D. Lizarralde, H. Hoskins, W. T. Wood, and R. A. Stephen, Methane hydrate and free gas on the Blake Ridge from vertical seismic profiling, *Science*, *273*, 1840-1843, 1996.

Hyndman, R.D., and E. E. Davis, A mechanism for the formation of methane hydrate and seafloor bottom-simulating reflectors by vertical fluid expulsion, *Journal of Geophysical Research*, *97*, 7025-7041, 1992.

Hyndman, R.D., T. Yuan, and K. Moran, The concentration of deep sea gas hydrates from downhole electrical resistivity logs and laboratory data, *Earth and Planetary Science Letters*, *172*, 167-177, 1999.

Kayen, R.E., and H. J. Lee, Pleistocene slope instability of gas hydrate-laden sediment on the Beaufort Sea margin, *Marine Geotechnology*, *10*, 125-141, 1991.

Kennett, J. P., K. G. Cannariato, I. L. Hendy, R. J. Behl, Carbon isotopic evidence for methane hydrate stability during Quaternary Interstadials, *Science*, *288*, 128-133, 2000.

Kleinberg, R.L., C. Flaum, D. D. Griffin, P. G. Brewer, G. E. Malby, E. T. Peltzer, and J.P. Yesinowski, Deep sea NMR: Methane hydrate growth habit in porous media and its relationship to hydraulic permeability, deposit accumulation, and submarine slope stability, *Journal of geophysical research*, *108*, 2508, 2003.

Kvenvolden, K.A., Gas hydrates: Geological perspective and global change, *Review of Geophysics*, *31*, 173-187, 1993.

Liu, X., and P. B. Flemings, Stress-limited gas column height in the gas hydrate system of Blake Ridge, in *Proceedings of the 4th International Conference on Gas Hydrates*, Yokohama, Japan, 807-812, 2002.

Liu, X., and P. B. Flemings, Passing gas through the hydrate stability zone at southern Hydrate Ridge, offshore Oregon, *Earth and Planetary Science Letters*, in press, 2005.

MacDonald, I.R., L. Lee, K. T. Scott, N. L. Guinasso, R. Sassen, and J. M. Brooks, Gas hydrate that breaches the sea floor on the continental slope of the Gulf of Mexico, *Geology*, *22*, 699-702, 1994.

Milkov, A.V., and R. Sassen, Economic geology of offshore gas hydrate accumulations and provinces, *Marine and Petroleum Geology*, *19*, 1-11, 2002.

Milkov, A.V., Y.-J. Lee, W. S. Borowski, M. E. Torres, W. Xu, H. Tomaru, A. M. Trehu, P. Schultheiss, G. R. Dickens, and G. E. Claypool, Co-existence of gas hydrate, free gas, and brine within the regional gas hydrate stability zone at Hydrate Ridge (Oregon margin): Evidence from prolonged degassing of a pressurized core, *Earth and Planetary Science Letters*, *222*, 829-843, 2004.

Moridis, G.J., M. B. Kowalsky, and K. Pruess, Depressurization-induced gas production from Class 1 hydrate deposits, *SPE*, 97266, 2005.

Munck, J., S. Skjoid-Jorgensen, and P. Rasmussen, Computations of the Formation of Gas Hydrates, *Chemical Engineering Science*, *43*, 2661-2672, 1988.

Nisbet, E.G., The end of the ice age, *Canadian Journal of Earth Science*, *27*, 148-157, 1990.

Paull, C.K., W. Ussler, W. S. Borowski, and F. N. Spiess, Methane-rich plumes on the Carolina continental rise: Associations with gas hydrates, *Geology*, *23*, 83-84, 1995.

Paull, C.K., W. J. Buelow, W. Ussler III, and W. S. Borowski, Increased continental-margin slumping frequency during sea-level lowstands above gas hydrate-bearing sediments, *Geology*, *24*, 143-146, 1996

Phillips, O.M., *Flow and reactions in permeable rocks*, 285 pp., Cambridge, New York, 1991.

Rehder, G., P. W. Brewer, E. T. Peltzer, and G. Friederich, Enhanced lifetime of methane bubble streams within the deep ocean, *Geophysical Research Letters*, *29* (21), 1-4, 2002.

Rempel, A.W., and B. A. Buffett, Formation and accumulation of gas hydrate in porous media, *Journal of Geophysical Research*, *102*, 10151-10164, 1997.

Schlumberger, *Log Interpretation Principles/Applications*, 227 pp., Schlumberger, Houston, 1989.

Schowalter, T.T., Mechanics of secondary hydrocarbon migration trapping, *American Association of Petroleum Geologist Bulletin*, *63*, 723-760, 1979.

Sloan, E.D., *Clathrate hydrates of natural gases*, 705 pp., Marcel Dekker, New York, 1998.

Spangenberg, E., Modeling of the influence of gas hydrate content on the electrical properties of porous sediments, *Journal of Geophysical Research*, *106*, 6535-6548, 2001.

Suess, E., R. W. Collier, J. Greinert, P. Linke, G. Rehder, A. Trehu, K. Wallmann, G. Winckler, E. Zuleger, M. E. Torres, and G Bohrmann, Gas hydrate destabilization: Enhanced dewatering, benthic material turnover and large methane plumes at the Cascadia convergent margin, *Earth and Planetary Science Letters*, *170*, 1-15, 1999.

Tan, B., J. T. Germaine, and P. B. Flemings, Consolidation and strength characteristics of sediments from ODP Site 1244, Hydrate Ridge, Cascadia Continental Margin, *Proceedings of the Ocean Drilling Program Scientific Results*, *204*, submitted.

Taylor, M.H., W. P. Dillon, and I. A. Pecher, Trapping and migration of methane associated with the gas hydrate stability zone at the Blake Ridge Diapir, *Marine Geology*, *164*, 79-89, 2000.

Teichert, B.M.A., B. Bock, P. Linke, A. Eisenhauer, G. Bohrmann, and A. Haase-Schramm, U/Th systematics and ages of authigenic carbonates from Hydrate Ridge, Cascadia Margin: Recorders of fluid flow variations, *Geochimica et Cosmochimica Acta*, *67*, 3845-3857, 2003.

Thomeer, J.H.M., Introduction of a pore geometrical factor defined by the capillary pressure curve, *SPE*, 1324, 1960.

Tohidi, B., R. Anderson, M. B. Clennell, R. W. Burgass and A. B. Biderkab, Visual observation of gas-hydrate formation and dissociation in synthetic porous media by means of glass micromodels, *Geology*, *29*, 867-870, 2001.

Torres, M.E., M. A. de Angelis, K. U. Heeschen, S. L. Colbert, M. D. Tryon, K. M. Brown, E. Suess, J. McManus, and D. E. Hammond, Fluid and chemical fluxes in and out of sediments hosting methane hydrate deposits on Hydrate Ridge, OR, I: Hydrological provinces, *Earth and Planetary Science Letters*, *201*, 525-540, 2002.

Torres, M.E., K. Wallmann, A. M. Trehu, G. Bohrmann, W. S. Borowski, and H. Tomaru, Gas hydrate growth, methane transport, and chloride enrichment at the southern summit of Hydrate Ridge, Cascadia margin off Oregon, *Earth and Planetary Science Letters*, *226*, 225-241, 2004.

Trehu, A.M., G. Bohrmann, M. E. Torres, G. F. Moore, and E. Suess, Temporal and spatial evolution of a gas hydrate-bearing accretionary ridge on the Oregon continental margin, *Geology*, *27*, 939-942, 1999.

Trehu, A.M., G. Bohrmann, F. R. Rack, M. E. Torres, et al., *Proceedings of the Ocean Drilling Program Initial Reports*, *204*, 2003.

Trehu, A.M., P. B. Flemings, N. L. Bangs, J. Chevallier, E. Gracia, J. E. Johnson, C.-S. Liu, X. Liu, M. Riedel, and M. E. Torres, Feeding methane vents and gas hydrate deposits at south Hydrate Ridge, *Geophysical Research Letters*, *31*, doi:10.1029/2004GL021286, 2004a.

Trehu, A.M., P. E. Long, M. E. Torres, G. Bohrmann, F. R. Rack, et al., Three-dimentional distribution of gas hydrate beneath southern Hydrate Ridge: constraints from ODP Leg 204, *Earth and Planetary Science Letters*, *222*, 845-862, 2004b.

Turcotte, D.L., and G. Schubert, *Geodynamics*, 456 pp., Cambridge University Press, Cambridge, 2002.

Vogt, P.R., and W.-Y. Jung, Holocene mass wasting on upper non-Polar continental slopes-due to post-Glacial ocean warming and hydrate dissociation? *Geophysical Research Letter*, *29*, doi:10.1029/2001/GK013488, 2002.

Wood, W.T., R. D. Hyndman, J. F. Gettrust, N. R. Chapman, and G. D. Spence, Decreased stability of methane hydrates in marine sediments owing to phase-boundary roughness, *Nature*, *420*, 656-660, 2002.

Xu, W., and C. Ruppel, Predicting the occurrence, distribution, and evolution of methane gas hydrate in porous marine sediments, *Journal of Geophysical Research*, *104*, 5081-5095, 1999.

Xu, W., R. P. Lowell, and E. T. Peltzer, Effect of seafloor temperature and pressure variations on methane flux from a gas hydrate layer: Conditions between current and late Paleocene climate conditions, *Journal of Geophysical Research*, *106*, 26,413-26,423, 2001.

Xu, W., Phase balance and dynamic equilibrium during formation and dissociation of methane gas hydrate, in *Proceedings of the 4th International Conference on Gas Hydrates*, Yokohama, Japan, 195-200, 2002.

Xu, W., Modeling dynamic marine gas hydrate systems, *American Mineralogist*, *89*, 1271-1279, 2004.

Yousif, M.H., H. H. Abass, and E. D. Sloan, Experimental and theoretical investigation of methane-gas-hydrate dissociation in porous media, *SPE Reservoir Engineering*, *6*, 69-76, 1991.

Zatsepina, O.Y., and B. A. Buffett, Nucleation of gas hydrate in marine environments, *Geophysical Research Letters*, *30*, doi:10.1029/2002GL016802, 2003.

Appendix A

THERMODYNAMIC CALCULATIONS OF GAS HYDRATE STABILITY

(1) The L+G phase equilibrium

Liquid-gas phase equilibrium exists, when the chemical potential of methane in the liquid phase equals that of methane in the gas phase:

$$\ln m_{CH_4} = \ln x_{CH_4} P + \ln \phi_{CH_4} - \frac{\mu^0_{CH_4}}{RT} + 2\sum_c \lambda_{CH_4-c} m_c + 2\sum_a \lambda_{CH_4-a} m_a + \sum_c \sum_a \zeta_{CH_4-a-c} m_c m_a ,$$

(A.1)

where m_{CH4} is the methane solubility, x_{CH4} is the mole fraction of methane in the gas phase, ϕ_{CH4} is the fugacity coefficient of methane in the gas phase, μ_{CH4} is the chemical potential of methane, λ and ζ are the ions interaction parameters, a is the anion and c is the cation. We assume that negligible water exist in gaseous CH_4. The virial equation of state in *Duan et al.* [1992] is used to describe the properties of methane gas phase (e.g., ϕ_{CH_4}). The parameters of $\mu^0_{CH_4}$, λ_{CH_4-a}, λ_{CH_4-c}, ζ_{CH_4-a-c} in (A.1) is given by *Duan et al.* [1992].

(2) The L+H phase equilibrium

The equilibrium conditions between hydrate and liquid water are established by *Henry et al.* [1999]. The chemical potential of water in the hydrate phase (μ^w_h) is assumed to equal that of water in the liquid phase (μ^w_l) (i.e., $\mu^w_l = \mu^w_h$). μ^w_h is given by

$$\mu^w_h = \mu^w_\beta + \sum_i \nu_i \ln(1 - \eta_i) , \quad (A.2)$$

where μ_β^w is the chemical potential of water in the hydrate lattice with all cages empty (i.e., the empty lattice), η_i (i=1,2) is the degree of occupancy of the small and large cages, ν_i is the number of cage of type i per molecular of water. The empty hydrate lattice serves as a hypothetical reference state. The cage occupancy (η_i) is estimated by

$$\eta_i = \frac{C_i f}{1 + C_i f} \quad , (A.3)$$

where C_i is the Langmuir constant for cage type i and f is the fugacity of methane. Parameters from *Munck and Rasmussen* [1988] are used for the computation of the Langmuir constants.

We calculate the chemical potential difference of water between the empty lattice and the pure state according to

$$\frac{\mu_\beta^w - \mu_l^w}{RT}(P,T) = \frac{\mu_\beta^w - \mu_l^w}{RT}(P_0,T_0) - \int_{T_0}^{T} \frac{(H_\beta - H_l)}{RT^2} dT + \int_{P_0}^{P} \frac{V_\beta - V_l}{RT} dP - \ln a_w \quad (A.4)$$

where P and T are the pressure and temperature at which hydrate forms, P_0 and T_0 are the pressure and temperature of the standard reference state (T_0=273.15 K and P_0=1 bar). The first term on the right side of (A.4) defines the chemical potential difference for the reference state. The second and third terms account for the enthalpy (H) and volume (V) differences between the empty hydrate lattice and the liquid water. a_w is the activity of water, which represents a measure of the effective concentration of water in the solution. The activity of water for mixed electrolyte solutions is calculated according to *Dickens and Quinby-Hunt* [1997].

The L-H phase equilibrium is computed by equating the water chemical potentials in the hydrate and liquid phases ($\mu_h^w = \mu_l^w$). Combining (A.2), (A.3) and (A.4), we obtain

$$\mu_h^w - \mu_l^w = \sum_i \nu_i \ln(1-\eta_i) + \frac{\mu_\beta^w - \mu_l^w}{RT}(P_0, T_0) - \int_{T_0}^{T} \frac{H_\beta - H_l}{RT^2} dT + \int_{P_0}^{P} \frac{V_\beta - V_l}{RT} dP - \ln a_w = 0$$

(A.5)

The equilibrium methane fugacity is first calculated from (A.5) and from the Langmuir constants. The equilibrium methane solubility is then computed from the methane solubility model of *Duan et al.* [1992].

Appendix B

HALF-SPACE SALT DIFFUSION WITH GAS SUPPLY FROM DEPTH

Consider a vertical zone of elevated salinity through which gas is being transported within the RHSZ. At depth z, the gas chimney is kept at three-phase equilibrium salinity $C_{eq}(z)$ and initially the bounding pore water has normal salinity C_{sw}. The total amount of salt lost from the chimney to the bounding pore water is given by (*mass per unit area*) [*Turcotte and Schubert*, 2002]

$$2\phi\rho_w\left[C_{eq}(z)-C_{sw}\right]\sqrt{\frac{Dt}{\pi}}\,, \quad (B.1)$$

where D is the chemical diffusivity for Cl^-. Equilibrium requires further growth of the hydrate to compensate the loss of salt by lateral diffusion. The chimney is maintained at three-phase equilibrium by further hydrate formation. If S_h increases by ΔS_h over a time interval t, S_w decreases by ΔS_h accordingly. Note that S_w and S_h refer to the volume fractions of water and hydrate in the original space and that free gas expands the volume when it becomes stable. Thus, the amount of salt in the chimney decreases by (*mass per unit area*)

$$\phi\rho_w bC_{eq}(z)\Delta S_h(z,t)\,, \quad (B.2)$$

where b is the half-width of the chimney. This provides a minimum estimate of the change in S_w. Following mass conservation for salt, the decrease in the amount of salt in the chimney equals that lost to the bounding pore water. By equating (B.1) and (B.2), we obtain

$$\phi\rho_w bC_{eq}(z)\Delta S_h(z,t) = 2\phi\rho_w\left[C_{eq}(z) - C_{sw}\right]\sqrt{\frac{Dt}{\pi}}. \quad (B.3)$$

Over this time interval, the S_h increase needed to maintain the equilibrium is

$$\Delta S_h(z,t) = \frac{2}{b}\left(1 - \frac{C_{sw}}{C_{eq}(z)}\right)\sqrt{\frac{Dt}{\pi}}. \quad (B.4)$$

The rate of CH_4 depletion *(mass per unit volume per unit time)* as a result of loss of salt is given by

$$q_{sink}(z,t) = \frac{M_{CH_4}}{M_h}\rho_h\frac{\partial\Delta S_h(z,t)}{\partial t}, \quad (B.5)$$

where M_{CH_4} and M_h are the molecular weight of methane and hydrate respectively. Substituting (B.4) into (B.5) yields

$$q_{sink}(z,t) = \frac{M_{CH_4}}{M_h}\frac{\rho_h}{b}\left(1 - \frac{C_{sw}}{C_{eq}(z)}\right)\sqrt{\frac{D}{\pi t}}. \quad (B.6)$$

Integrating q_{sink} along the chimney with height Z, we obtain the total rate of CH_4 depletion (*mass per unit area per unit time)* due to loss of salt

$$Q_{sink}(t) = \int_0^Z q_{sink}(z,t)dz. \quad (B.7)$$

The gas supply rate from depth is denoted by Q_{source} *(mass per unit area per unit time)*. If $Q_{source} > Q_{sink}$, free gas is rapidly supplied into the chimney relative to the rate at which the excluded salt laterally diffuses. Gas supply is sufficient to maintain the chimney at three-phase equilibrium. If $Q_{source} < Q_{sink}$, diffusion of salt is significant compared with gas supply and three-phase equilibrium cannot be maintained.

At southern Hydrate Ridge, we assume the gas chimney has a porosity of 0.6, a height of 120 m and a half-width of 150 m (Fig. 2-10). Based on dating of the vent

carbonates [*Teichert et al.*, 2003], the gas chimney extended to the ridge crest at ~7 Ka BP. Given the chemical diffusivity $D=10^{-9}$ m^2 s^{-1} [*Rempel and Buffett*, 1997], gas supply ($\sim 10^2$ mol CH_4 m^{-2} $year^{-1}$) is more rapid than gas depletion (<10 mol CH_4 m^{-2} $year^{-1}$) caused by loss of salt. Thus, it is reasonable to assume no large-scale diffusion.

Appendix C

GOVERNING EQUATIONS FOR HYDRATE FORMATION AND DISSOCIATION

The mass balance equation for methane (superscript *m*):

$$\phi\frac{\partial\left(\sum_{\beta=l,v,h}\rho_\beta S_\beta X\beta_\beta^m\right)}{\partial t}-\sum_{\beta=l,v}\mathrm{div}\left\{\frac{kk_{r\beta}}{\mu_\beta}\rho_\beta X_\beta^m\left(\nabla P_\beta-\rho_\beta g\right)\right\}-\mathrm{div}\left\{\phi D_l^m\rho_l\nabla X_l^m\right\}-q^m=0\,.\ (C.1)$$

The mass balance equation for water (superscript *w*):

$$\phi\frac{\partial\left(\sum_{\beta=l,h}\rho_\beta S_\beta X\beta_\beta^w\right)}{\partial t}-\sum_{\beta=l}\mathrm{div}\left\{\frac{kk_{r\beta}}{\mu_\beta}\rho_\beta X_\beta^w\left(\nabla P_\beta-\rho_\beta g\right)\right\}-\mathrm{div}\left\{\phi D_l^w\rho_l\nabla X_l^w\right\}-q^w=0\,.\ (C.2)$$

The mass balance equation for salt (superscript *s*):

$$\phi\frac{\partial\left(\sum_{\beta=l}\rho_\beta S_\beta X\beta_\beta^s\right)}{\partial t}-\sum_{\beta=l}\mathrm{div}\left\{\frac{kk_{r\beta}}{\mu_\beta}\rho_\beta X_\beta^s\left(\nabla P_\beta-\rho_\beta g\right)\right\}-\mathrm{div}\left\{\phi D_l^s\rho_l\nabla X_l^s\right\}-q^s=0\,.\ (C.3)$$

Appendix D

FINITE DIFFERENCE APPROXIMATION OF GOVERNING EQUATIONS

(1) Discretized equations

The mass and energy balance equations given by (3-1) are discretized in space and time using the finite difference method [*Falta et al.*, 1992]. For element *l* with a volume of V_l, the accumulation terms in (3-1) are:

$$\frac{d}{dt}\int_{V_l} M^\kappa dV_l = \frac{d}{dt} V_l M_l^\kappa , \qquad (D.1)$$

where M_l^κ is the average value of M^κ over the volume V_l. Similarly, the sink/source terms in equation (3-1) become:

$$\int_{V_l} q^\kappa dV_l = V_l q_l^\kappa . \qquad (D.2)$$

And the flux terms in equation (3-1) become:

$$\int_{\Gamma_l} F^\kappa \cdot n d\Gamma_l = \sum_m A_{lm} F_{lm}^\kappa , \qquad (D.3)$$

where A_{lm} is the area of the interface between elements *l* and *m*, and F_{lm}^κ is the flux of component κ between elements *l* and *m*. Substituting equations (D.1-D.3) into the governing equation (3-1) yields:

$$\frac{dM_l^\kappa}{dt} = \frac{1}{V_l}\sum_m A_{lm} F_{lm}^\kappa + q_l^\kappa . \qquad (D.4)$$

The accumulation terms are discretized in time using a first-order finite difference approximation. The flux and sink/source terms are evaluated at the new time level $t^{n+1} = t^n + \Delta t$ to avoid numerical instability in multiphase flow simulation**.** The mass

and energy balance equations are written in a discretized form in terms of the residual of each component in each element [*Falta et al.*, 1992]:

$$R_l^{\kappa,n+1} = M_l^{\kappa,n+1} - M_l^{\kappa,n} - \frac{\Delta t}{V_l}\left\{\sum_m A_{lm} F_{lm}^{\kappa,n+1} + V_l q_l^{\kappa,n+1}\right\} = 0\,, \qquad \text{(D.5)}$$

where κ is methane, water, salt and heat. For a flow domain discretized into N blocks, (D.8) yields a system of $4N$ coupled nonlinear equations.

The gas phase mass flux term is approximated using a first-order finite difference in space as:

$$F_{g,lm}^{\kappa} = -k_{lm}\left(\frac{k_{rg}\rho_g}{\mu_g}\right)_{lm}\left(\frac{P_{g,l} - P_{g,m}}{d_{lm}} - \rho_{g,lm} g\right), \quad \text{(D.6)}$$

where d_{lm} is the distance between the centers of elements l and m. The subscript lm indicates that the parameter is evaluated at the interface between elements l and m. Different physical parameters require different interface weighting algorithm. For example, we use upstream weighting to calculate the phase mobility and harmonic weighting to calculate the intrinsic permeability. The component mass fluxes in the liquid phase are:

$$F_{w,lm}^{\kappa} = -k_{lm}\left(\frac{k_{rw}\rho_w}{\mu_w}\right)_{lm}\left(\frac{P_{w,l} - P_{w,m}}{d_{lm}} - \rho_{w,lm} g\right) + J_{w,lm}^{\kappa}\,. \text{(D.7)}$$

The diffusive mass fluxes for methane and salt are:

$$J_{w,lm}^{\kappa} = -\left(\phi S_w D_w^{\kappa} \rho_w\right)_{lm} \frac{X_{w,l}^{\kappa} - X_{w,m}^{\kappa}}{d_{lm}}\,. \quad \text{(D.8)}$$

(2) Newton-Raphson Method

A residual-based Newton-Raphson method is used to iteratively solve the nonlinear balance equations given by (D.5). Newton-Raphson method may be expressed as [*Farnstrom and Ertekin*, 1987; *Falta et al.*, 1992]:

$$R\left(x^{p+1}\right) = R\left(x^{p}\right) + \left(\frac{\partial R(x)}{\partial x}\right)^{p}\left(x^{p+1} - x^{p}\right), \qquad (D.9)$$

where x is the vector of primary variables in each element, p is the iteration index, and the term $\frac{\partial R}{\partial x}$ represents the derivatives of the residual with respect to the vector of primary variables. These derivatives are arranged into the Jacobian matrix. An exact solution to the system of equations is obtained, when each residual equals zero at the iteration index p+1, *i.e.*, $R\left(x^{p+1}\right) = 0$. Thus (D.9) becomes into:

$$\left(\frac{\partial R(x)}{\partial x}\right)^{p}\left(x^{p+1} - x^{p}\right) = -R(x^{p}). \qquad (D.10)$$

These equations may be rewritten as a matrix form. For example, for an element l in which three phases (hydrate, water and gas) coexist, the primary variables are P, T, S_w and S_h. The matrix form is:

$$\begin{bmatrix} \frac{\partial R_l^{m,p}}{\partial P} & \frac{\partial R_l^{m,p}}{\partial T} & \frac{\partial R_l^{m,p}}{\partial S_w} & \frac{\partial R_l^{m,p}}{\partial S_h} \\ \frac{\partial R_l^{w,p}}{\partial P} & \frac{\partial R_l^{w,p}}{\partial T} & \frac{\partial R_l^{w,p}}{\partial S_w} & \frac{\partial R_l^{w,p}}{\partial S_h} \\ \frac{\partial R_l^{s,p}}{\partial P} & \frac{\partial R_l^{s,p}}{\partial T} & \frac{\partial R_l^{s,p}}{\partial S_w} & \frac{\partial R_l^{s,p}}{\partial S_h} \\ \frac{\partial R_l^{e,p}}{\partial P} & \frac{\partial R_l^{e,p}}{\partial T} & \frac{\partial R_l^{e,p}}{\partial S_w} & \frac{\partial R_l^{e,p}}{\partial S_h} \end{bmatrix} \times \begin{bmatrix} \Delta P \\ \Delta T \\ \Delta S_w \\ \Delta S_h \end{bmatrix} = \begin{bmatrix} -R_l^{m,p} \\ -R_l^{w,p} \\ -R_l^{s,p} \\ -R_l^{e,p} \end{bmatrix}, \qquad (D.11)$$

where the first matrix is the Jacobian matrix, the second is the vector of unknown changes in the primary variables in each element from the previous iteration, and the third is the vector of residual of each component in each element.

Iteration process is continued until the residuals $R_l^{\kappa,n+1}$ are reduced below a convergence tolerance. Convergence is usually reached in less than 5 iterations. If convergence cannot be reached within a certain number of iteration, the time step size Δt is reduced and a new iteration is initiated.

(3) Comparison with analytical solution

We use the developed model to solve a one-dimensional steady state fluid flow problem with pressure-dependent fracture permeability and make comparison with the analytical solution [*Liu and Flemings*, 2002].

We model the fractured sediments as stiff, impermeable matrix block interconnected by evenly spaced, compliant matrix (Fig. D-1). Bulk permeability through a network of two orthogonal sets of vertical fracture can be expressed as:

$$k = \frac{w^3}{6S}, \qquad (D.12)$$

where k is the bulk permeability, w is the fracture aperture and S is the fracture spacing. We assume that water flow through the sediments via the fractures at a constant rate. Variations in fracture aperture are only due to changes in effective stress. In the model, fracture aperture is related to horizontal effective stress (σ_h=S_{hmin}-P_w) as

$$w = w_0 e^{-C\sigma_h} = w_0 e^{-C(S_{h\min} - P_w)},$$

where w_0 is the initial fracture aperture and C is the fracture compressibility. In this case, an isotropic stress state is assumed, i.e., the minimum horizontal stress equals the

overburden stress. We use S=0.3 mm, C=0.43 MPa^{-1}, and w_0=0.16 μm [*Liu and Flemings*, 2002].

We evaluate the effects of changing water flux on water pressure using numerical simulations (Fig. D-2). The analytical solution predicts that at high flux, the water pressure follows the lithostatic gradient at depths below the seafloor. Our numerical simulations also show that water pressure parallels the overburden stress. As water flux increases, water pressure will converge on the overburden stress. This comparison can testify the accuracy of our numerical results.

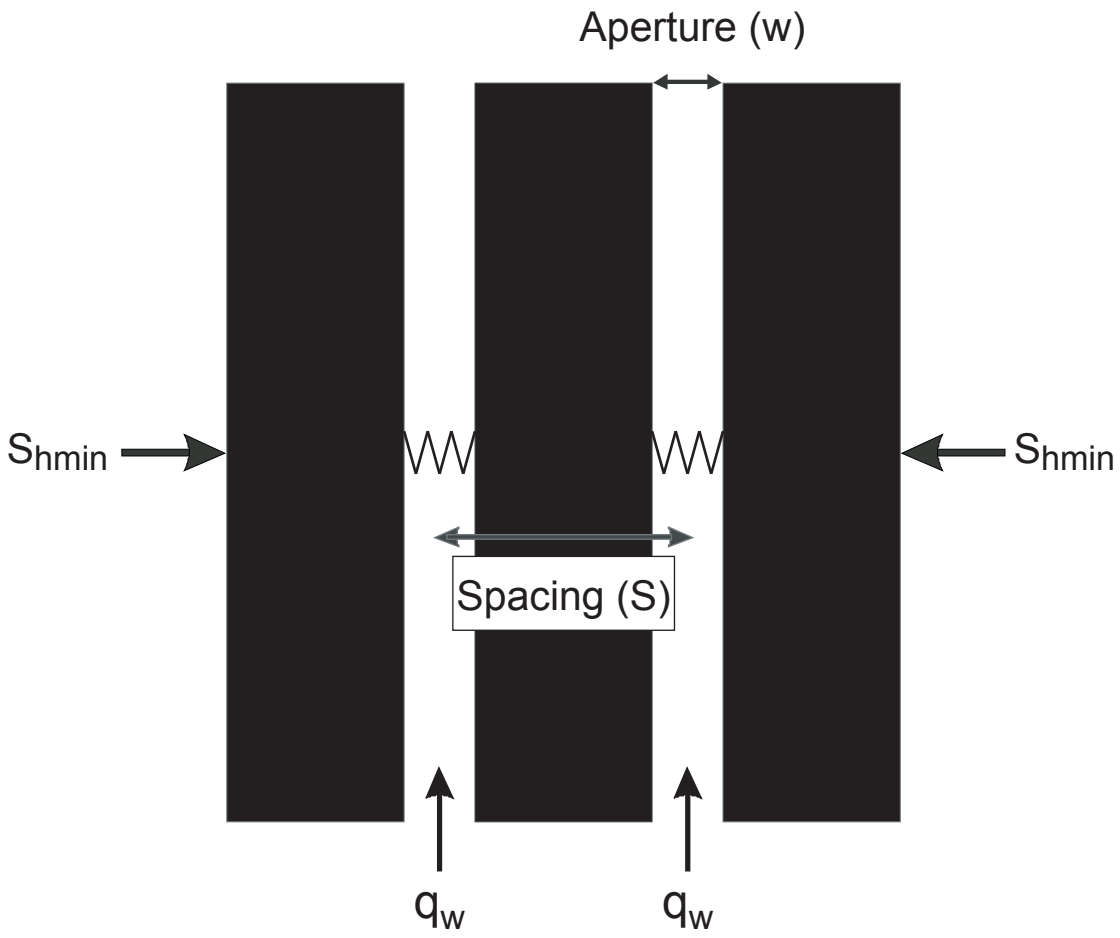

Fig. D-1: Sketch of hydro-mechanical model. Water enters and leaves the model domain at a constant flux rate. Matrix blocks (black area) are impermeable, and all flow occurs through fractures (white area) with aperture (w) and spacing (S).

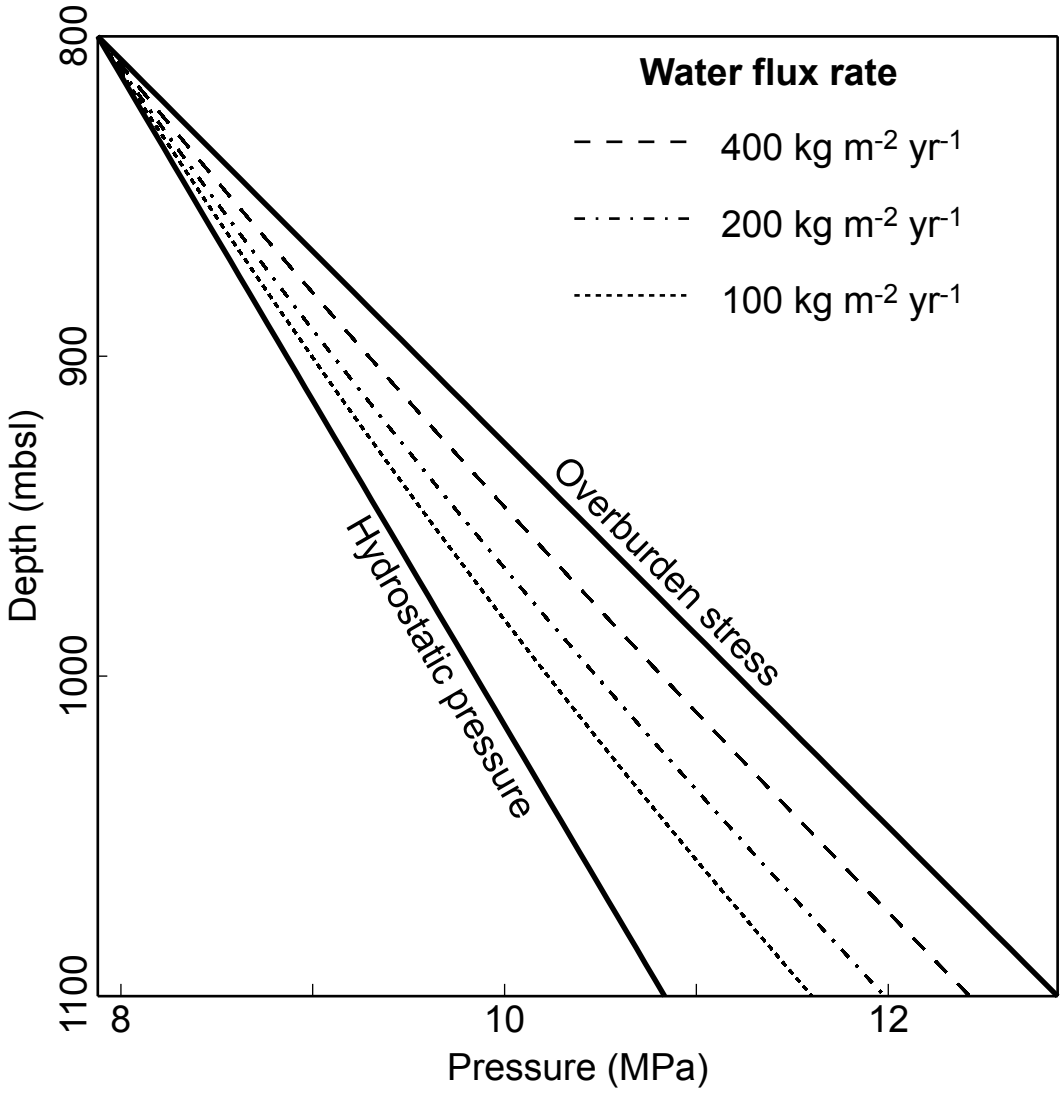

Fig. D-2: Simulated pressures in the fractured sediment at different water flux rates. The water pressure follows the lithostatic gradient at depths below the seafloor.

Appendix E

A SIMPLIFIED ANALYSIS OF DEWATERING IN BLAKE RIDGE

We interpret that the Blake Ridge migrates to the southwest, deposition on its southern flank and erosion on its northern flank. We assume that the Blake Ridge evolves in a self-similar pattern. The ridge is stationary relative to the leading edge and has both sediment solid and saturated pore space moving through it. Here we derive an expression for dewatering in the Blake Ridge with a self-similar geometry.

We solve this problem in a "fully compacted" coordinate system where the length scale is the distance from the surface to an individual sediment grain when no porosity is present. The main advantages of this approach are: (1) a constant nodal distance that fixes an otherwise moving and deforming mesh; (2) each element contains the same amount of sediment grains. In this new domain, the sediment velocity has no vertical component. Sediment particle is assumed to migrate horizontally through the wedge at a constant rate.

The fluid flow in a compacting porous media is described as:

$$\frac{\partial[\rho_s(1-\phi)]}{\partial t} + \nabla \cdot [\rho_s(1-\phi)v_s] = 0, \qquad \text{(E.1)}$$

$$\frac{\partial(\rho_w \phi)}{\partial t} + \nabla \cdot (\rho_w \phi v_w) = 0, \qquad \text{(E.2)}$$

For steady state, the above equations collapse into:

$$\nabla \cdot [\rho_s(1-\phi)v_s] = 0, \qquad \text{(E.3)}$$

$$\nabla \cdot (\rho_w \phi v_w) = 0, \quad \text{(E.4)}$$

Where ρ_s and ρ_w are the densities of sediment grain and water, ϕ is the porosity, and v_s and v_w are the velocities of sediment grain and water. If the sediment grain and water are assumed to be incompressible, (E.3) and (E.4) become into:

$$\nabla \cdot \left[(1-\phi)v_s\right] = 0, \quad \text{(E.5)}$$

$$\nabla \cdot (\phi v_w) = 0. \quad \text{(E.6)}$$

Combining (E.5) and (E.6), we get:

$$\nabla \cdot v_s + \nabla \cdot \left[\phi(v_w - v_s)\right] = 0. \quad \text{(E.7)}$$

Darcy's velocity is defined as:

$$q_w = \phi(v_w - v_s). \quad \text{(E.8)}$$

Combining (E.7) and (E.8), we obtain:

$$\nabla \cdot v_s + \nabla \cdot q_w = 0. \quad \text{(E.9)}$$

We rearrange (E.5) by expanding the productive derivative:

$$\nabla \cdot v_s = \frac{v_s}{1-\phi}\nabla\phi. \quad \text{(E.10)}$$

The porosity-effective stress relationship is described by:

$$\phi = \phi_0 e^{-\beta\sigma} = \phi_0 e^{-\beta(S_v - P_w)}, \quad \text{(E.11)}$$

where ϕ_0 is the reference porosity, β is the bulk compressibility, S_v is the overburden stress, and P_w is the water pressure.

Substituting (E.9) and (E.11) into (E.10) yields:

$$-\nabla \cdot q_w = \frac{\beta\phi}{1-\phi} v_s \left(\nabla S_v - \nabla P_w\right). \quad \text{(E.12)}$$

Darcy's law is defined as:

$$q_w = -\frac{k}{\mu}(\nabla P_w - \rho_w g), \qquad \text{(E.13)}$$

where k is the intrinsic permeability, μ is the viscosity, and g is the acceleration due to gravity. Substituting (E.13) into (E.12), we finally get:

$$\nabla \cdot \left\{ \frac{k}{\mu}\left(\nabla P_w - \rho_w g\right) \right\} = \frac{\beta\phi}{1-\phi} v_s \left(\nabla S_v - \nabla P_w\right). \quad \text{(E.14)}$$

Vitae
Xiaoli Liu

Basin Research Group
Department of Geosciences
The Pennsylvania State University
University Park, PA 16802

xliu@geosc.psu.edu
Phone: (814) 863-9663
Fax: (814) 863-8724

EDUCATION

Ph.D. Candidate, Hydrogeology, The Pennsylvania State University, 2000-present

Courses: Computational Geomechanics, Fluid Mechanics, Geochemical Thermodynamics, Numerical Reservoir Simulation, Numerical Solutions of PDEs

Thesis: "Shallow marine gas hydrates: Dynamics of a sensitive methane reservoir"

M.E., Petroleum Engineering, Research Institute of Petroleum E&D, Beijing, China, 1997-2000

Courses: Theoretical Soil Mechanics, Numerical Simulation of EOR, Advanced Flow in Porous Media, Reservoir Engineering

Thesis: "Simulating hydraulic fracture propagation in layered formations"

B.Sc., Geophysics, Tongji University, Shanghai, China, 1993-1997

Courses: Geodynamics, Structural Geology, Stratigraphy, Well-logging, Seismic Processing and Interpretation, Digital Signal Processing

Thesis: "Numerical modeling of uplift and evolution of Himalayan orogenic belts"

PUBLICATIONS

- Liu, X. and Flemings, P.B. (2005). Numerical modeling of dynamic marine gas hydrates systems, *Journal of Geophysical Research* (in preparation).
- Liu, X. and Flemings, P.B. (2005). Passing gas through the hydrate stability zone at southern Hydrate Ridge, offshore Oregon, *Earth and Planetary Science Letters* (in press).
- Trehu, A., Flemings, P.B., Bangs, N. L., Chevallier, J., Gracia, E., Johnson, J. E., Liu, C.-S., Liu, X., Riedel, M., Torres, M.E. (2004). Feeding methane vents and gas hydrate deposits at south Hydrate Ridge, *Geophysical Research Letters 31*, doi:10.1029/2004GL021286.
- Flemings, P.B., Liu, X., and Winters, W. (2003). Critical overpressure and multiphase flow in Blake Ridge hydrates, *Geology 31*, p.1057-1060.
- Liu, X. and Flemings, P.B. (2002). Stress-limited gas column heights in the gas hydrate system of Blake Ridge, *Proceedings of the 4th International Conference on Gas Hydrates*, p. 807-812.
- Flemings, P.B., Comisky, J., Liu, X., and Lupa, J.A. (2001). Stress-controlled porosity in overpressured sands at Bullwinkle (GC65), deepwater Gulf of Mexico, *Offshore Technology Conference 2001*, 13103.